

UNDERSTANDING THE GROWTH OF GRAPHENE ENCAPSULATED NOBLE METAL  
NANOPARTICLES: MORPHOLOGICAL AND STRUCTURAL EVOLUTION STUDIES,  
GROWTH MECHANISMS, AND CHARACTERIZATION

by

JUNCHI WU

NITIN CHOPRA, COMMITTEE CHAIR  
RAMANA G. REDDY  
MARTIN G. BAKKER

A THESIS

Submitted in partial fulfillment of the requirements  
for the degree of Master of Science  
in the Department of Metallurgical and Materials Engineering  
in the Graduate School of  
The University of Alabama

TUSCALOOSA, ALABAMA

2011

Copyright Junchi Wu 2011

ALL RIGHTS RESERVED

## ABSTRACT

The major goal of this work was to study the morphological evolution of noble metal nanoparticles such as gold, palladium, and platinum nanoparticles as a function of single-parameter variation in simple synthesis approach. As a next step, these nanoparticles were plasma oxidized to result in surface oxidized noble metal nanoparticles. These noble metal nanoparticles were further utilized for the growth of graphene shells in a chemical vapor deposition method resulting in graphene encapsulated noble metal nanoparticles. In regard to morphological evolution of noble metal nanoparticles, systematic studies were performed, where single growth parameter (temperature, metal salt concentration, surfactant type or concentration, seed amount, or growth duration) was varied while other parameters were kept constant. Gold nanoparticles were synthesized by both single-step method and seed-growth method while palladium and platinum nanoparticles were synthesized at high temperature by alcohol reduction. The size, shape, crystallinity, and sample heterogeneity for the nanoparticles were characterized by high-resolution transmission electron microscopy. Single parameter systematic studies allowed for fundamentally understanding the growth and evolution of noble metal nanoparticles. As temperature increased, nanoparticles size increased due to the decrease of absolute value of volume Gibbs free energy. With the existence of surfactant (e.g. hexadecyltrimethylammonium bromide), stabilizer molecules bind to nanoparticles surface with affinity to different facets. When synthesis temperature higher than boiling point of water, the annealing process resulted in rupture of surfactant from weak binding facets, and boosted anisotropic growth of nanoparticles.

Subsequently, oxidation behavior of gold, palladium, and platinum were studied by X-ray photoelectron spectroscopy. Gold oxide, palladium oxide, and platinum oxide were found after plasma oxidation. Noble metal nanoparticles were plasma oxidized for 30 min, and then further utilized for chemical vapor deposition (CVD) of graphene shells. These graphene encapsulated noble metal nanoparticles were thoroughly characterized by scanning electron microscopy, transmission electron microscopy, X-ray photoelectron spectroscopy, and Raman spectroscopy. Aggregation of noble metal nanoparticles was observed after graphene growth. Raman spectra showed D-, G-band for graphene encapsulated gold, palladium and platinum nanoparticles after CVD growth. Raman chemical mapping indicates large area growth of graphene encapsulated nanoparticles.

## DEDICATION

This thesis is dedicated to my family.

## LIST OF ABBREVIATIONS AND SYMBOLS

<i>AA</i>	L-ascorbic acid
<i>AAO</i>	Amorphous alumina
<i>AgCl</i>	Silver chloride
<i>AgNO<sub>3</sub></i>	Silver nitrate
<i>Ar</i>	Argon
<i>Au</i>	Gold
<i>C</i>	Concentration
<i>C<sub>0</sub></i>	Equilibrium concentration
<i>c<sub>0</sub>'</i>	Initial concentration
<i>CCD</i>	Charge-coupled device
<i>cm<sup>-1</sup></i>	Reciprocal centimeter (wavenumber)
<i>CNT</i>	Carbon nanotube
<i>CTAB</i>	Hexadecyltrimethylammonium bromide
<i>CVD</i>	Chemical vapor deposition
<i>D</i>	Diffusion constant
<i>DI</i>	Deionized
<i>DDT</i>	1-dodecanethiol
<i>DMF</i>	Dimethylformamide
<i>EG</i>	Ethylene glycol
<i>g</i>	gram

<i>GICs</i>	Graphite intercalation compounds
<i>h</i>	Hour
$H_2$	Hydrogen
$H_2SO_4$	Sulfuric acid
$H_2O$	Water
$H_2O_2$	Hydrogen peroxide
$HAuCl_4$	Chlauric acid
$HAuCl_4 \cdot 3H_2O$	Gold chloride trihydrate
$H_2PtCl_6 \cdot 6H_2O$	Dihydrogen hexachloropatinate hexahydrate
<i>k</i>	Boltzmann constant
$KBr$	Potassium bromide
$KCl$	Potassium chloride
<i>M</i>	Mole per liter
<i>MB</i>	Methylene Blue
<i>mg</i>	Milligram
<i>min</i>	Minute
<i>mL</i>	Milliliter
<i>mol</i>	Mole
<i>MPTMS</i>	3-Mercaptopropyltrimethoxysilane
$N_2$	Nitrogen
$Na_2PdCl_4 \cdot xH_2O$	Sodium tetrachloropalladate hydrate
$NaBH_4$	Sodium borohydride
<i>n</i>	The number of growth species per unit volume

$\text{NPs}$	Nanoparticles
$O_2$	Oxygen
$^{\circ}\text{C}$	degree Celsius
$P$	Nucleation probability
$Pd$	Palladium
$PdCl_2$	Palladium chloride
$pKa$	Acid dissociation constant
$Pt$	Platinum
$PVP$	Polyvinylpyrrolidone
$rmp$	Revolutions per minute
$R_N$	Rate of nucleation per unit volume
$r^*$	Critical size for nucleus
$SEM$	Scanning Electron Microscopy
$SERS$	Surface enhanced Raman spectroscopy
$Si$	Silicon
$SiC$	Silicon carbide
$SLM$	Standard liter per minute
$T$	Temperature in Kelvin (K)
$TEM$	Transmission Electron Microscopy
$TOAB$	Tetraoctylammonium bromide
$W$	Watt
$XPS$	X-ray Photoelectron Spectroscopy
$\gamma$	Surface energy

$\Delta_r G$	Reaction Gibbs free energy
$\Delta G^*$	Critical Gibbs free energy for nucleation
$\Delta G_v$	Change of Gibbs energy per unit volume of solid phase for nucleation
$\Omega$	Atomic volume
$\sigma$	Supersaturation
$\Gamma$	Successful jump frequency
$\lambda$	Diameter of growth species
$\eta$	Viscosity of the solution

## ACKNOWLEDGMENTS

I would like to greatly thank my advisor, Dr. Nitin Chopra for his support and guidance. I would also like to thank Dr Reddy and Dr Bakker for serving on my committee. I would like to thank all of my group members who helped me at every step of my graduate research, with special thanks to Mr. Wenwu Shi (Graduate Student), Mr. Lyndon Smith Jr. Ms. Brandi Freeman (NSF-REU student), Mr. Larry Summerville (NSF-REU student), Ms. Laura Elena Philips (NSF-REU student), Mr. Robert Miller Wright (NSF-REU student), Mr. Paaras Agrawal (NSF-REH), and Mr. Andrew Lattner (NSF-REH).

Thanks to the Central Analytical Facility (CAF) staff including Mr. Rich Martens, Mr. Johnny Goodwin and Mr. Rob Holler for providing training and assistance. I also thank staff from Metallurgical and Materials Engineering (MTE) department and Center for Materials for Information Technology (MINT), Ms. Jan Creitz, Mr. Bob Fanning, Ms. Lyndall Wilson, Ms. Kim Walker, Ms. Casey Mcdow, Ms. Jamie Crawford, Dr. Mankey, Dr. LeClair, Mr. John Hawkins, and Mr. Jason Foster.

I am grateful to Materials Science and Engineering (MSE) program staff including Dr. Garry W. Warren, Dr. Mark L. Weaver for their consistent support through the program. I would like to thank financial support from CAF, MINT, and MSE at the University of Alabama, University of Alabama's Office of Sponsored Programs, Research Grant Committee Award, and NSF award (0925445) for my tuition, stipend, instrument time, supplies and infrastructure/resources. Finally, I would like to thank my family and friends with all encouragements and supports.

## CONTENTS

ABSTRACT .....	ii
DEDICATION .....	iv
LIST OF ABBREVIATIONS AND SYMBOLS .....	v
ACKNOWLEDGMENTS .....	ix
CONTENTS .....	x
LIST OF TABLES .....	xiii
LIST OF FIGURES .....	xv
1. INTRODUCTION .....	1
1.1. Noble metal nanoparticles .....	1
1.1.1 Types of nonspherical noble metal nanoparticles .....	2
1.1.2 Synthesis of nonspherical noble metal nanoparticles .....	5
1.1.3 Gold nanoparticles .....	6
1.1.4 Palladium nanoparticles .....	10
1.1.5 Platinum nanoparticles .....	11
1.2 Multi-component nanomaterials .....	13
1.3 Oxidation of noble metal nanoparticles .....	17
1.4 Noble metal nanoparticles/graphene heterostructure .....	19
1.4.1 Graphene synthesis .....	19
1.4.2 Chemistry of graphite .....	22

1.4.3	Methods for synthesizing graphene encapsulated gold nanoparticles .....	23
1.5	Raman Spectroscopy .....	27
1.6	Challenges, Motivations, and goals .....	29
2.	EXPERIMENTAL PROCEDURES .....	31
2.1	Materials and Methods .....	31
2.2	Synthesis of gold nanoparticles.....	33
2.3	Plasma oxidation of gold nanoparticles .....	38
2.4	Growth of graphene on gold nanoparticles .....	40
2.5	Synthesis of palladium nanoparticles .....	42
2.6	Synthesis of platinum nanoparticles.....	44
2.7	Dispersion and plasma oxidation of palladium, platinum nanoparticles .....	46
2.8	Growth of graphene on palladium and platinum nanoparticles .....	48
2.9	Characterization .....	49
2.10	Raman mapping for noble metal nanoparticles after graphene growth .....	51
2.11	Disperse noble metal nanoparticles on silicon wafer .....	52
2.12	Raman analysis of methylene blue on noble metal nanoparticles.....	53
3.	RESULT AND DISCUSSION .....	54
3.1	Synthesis and characterization of gold nanoparticles .....	54
3.1.1	Synthesis gold nanoparticles in single-step .....	55
3.1.2	Synthesis gold nanoparticles in seed-growth method.....	74
3.2	Synthesis and characterization of palladium nanoparticles.....	85
3.3	Synthesis and characterization of platinum nanoparticles .....	94
3.4	Plasma oxidation of noble metal nanoparticles.....	103

3.4.1	Plasma oxidation duration study of gold nanoparticles .....	103
3.4.2	Plasma oxidation of palladium nanoparticles .....	112
3.4.3	Plasma oxidation duration study of platinum nanoparticles .....	119
3.5	Fabrication of graphene encapsulated noble metal nanoparticles .....	128
3.6	Raman mapping for nanoparticles after graphene growth .....	136
3.7	Dispersion of noble metal nanoparticles .....	140
3.8	Raman spectroscopy of methylene blue on noble metal nanoparticles.....	142
4.	CONCLUSIONS AND FUTURE WORK .....	145
	REFERENCES .....	148

## LIST OF TABLES

Table 2.1 Systematic study for single-step synthesis of AuNPs. The nanoparticles were synthesized by varying one growth parameter at a time while other parameters remained fixed. The shaded region in the table denotes the changing parameter and baseline parameters (sample 2) are indicated by bold and italicized fonts.....	35
Table 2.2 Quenching conditions for AuNPs that were synthesized at 130 °C (Table 2.1, sample 7) .....	36
Table 2.3 Seed synthesis condition in seed-growth method.....	37
Table 2.4 Systematic study for growth condition of seed-growth synthesis of AuNPs. The nanoparticles were synthesized by varying one growth parameter at a time while other parameters remained fixed. The shaded region in the table denotes the changing parameter and baseline parameters (sample 2) are indicated by bold and italicized fonts.....	37
Table 2.5 Systematic study for synthesis of PdNPs. The nanoparticles were synthesized by varying one growth parameter at a time while other parameters remained fixed. The shaded region in the table denotes the varying parameter and baseline parameters (sample 3) are indicated by bold and italicized fonts.....	43
Table 2.6 Systematic study for synthesis of PtNPs. The nanoparticles were synthesized by varying one growth parameter at a time while other parameters remained fixed. The shaded region in the table denotes the changing parameter and baseline parameters (sample 2) are indicated by bold and italicized fonts. ....	45
Table 3.1 Result summary for systematic study indicating size, shape distribution, lattice spacing, and the corresponding planes for the as-prepared AuNPs according to the table 2.1.....	57
Table 3.2 Results summarizing the effect of quenching (table 2.2, sample 21-23) on AuNPs prepared at higher temperature (130 °C), indicating size, shape distribution, lattice spacing and the corresponding plane for after-quenched AuNPs.....	71
Table 3.3 Result summary for systematic study indicating size, shape distribution, lattice spacing, and the corresponding planes for the as-prepared AuNPs according to the table 2.4.....	76
Table 3.4 Result summary for systematic study indicating average size, shape distribution, lattice spacing, and the corresponding planes for the as-prepared PdNPs according to the table 2.5.....	86

Table 3.5 Result summary for systematic study indicating average size, shape distribution, lattice spacing, and the corresponding planes for the as-prepared PtNPs according to the table 2.6.....	95
Table 3.6 Binding energy (eV) derived from XPS study for AuNPs (table 2.1, sample 10 with different plasma oxidation duration) corresponding to the spectra as shown in figure 3.29 .....	106
Table 3.7 The ratio of AuO <sub>x</sub> calculated as peak area of AuO <sub>x</sub> over the sum of Au and AuO <sub>x</sub> peaks area as shown as figure 3.29 .....	108
Table 3.8 Binding energy (eV) derived from XPS study for shape controlled PdNPs with different plasma oxidation duration corresponding to the spectra as shown in figure 3.33. ....	115
Table 3.9 The ratio of PdO <sub>x</sub> calculated as peak area of PdO <sub>x</sub> over the sum of Pd and PdO <sub>x</sub> peaks area as shown as figure 3.33. ....	117
Table 3.10 Binding energy (eV) derived from XPS study for shape controlled PtNPs with different plasma oxidation duration corresponding to the spectra as shown in figure 3.36. ....	122
Table 3.11 The ratio of PtO <sub>x</sub> calculated as peak area of PtO <sub>x</sub> over the sum of Pt and PtO <sub>x</sub> peaks area as shown as figure 3.36. ....	124
Table 3.12 Binding energy (eV) chart derived from XPS study for AuNPs (table 2.1, sample 10 before, after plasma oxidation, and after graphene growth) corresponding to the spectra as shown in figure 3.42. ....	135
Table 3.13 Assignment for Raman peaks of methylene blue .....	144

## LIST OF FIGURES

- Figure 1.1 A few examples of different shapes 1D, 2D, 3D noble metal nanoparticles synthesized through solution-based approach. The first row shows the TEM (a - d) or SEM (e) images of 1D structure nanoparticles: (a) nanorods, (b) nanodumbbells, (c) nanobipyramids of Au/Ag, (d) silver nanowires, and (e) gold nanotube. The middle row shows some 2D structure nanoparticles: TEM images of (f) triangular gold nanoplates, (g) silver nanodisks, and (h) gold ribbons; SEM image of (i) gold belts. The last row shows some typical 3D structures: TEM images of (j) nanocubes, (k) nanotepropods, and (l - m) star-shaped gold nanoparticles, (n) silver nanohexapods, SEM image of an (o) Au-Ag nanocage. Reprinted with permission from <sup>14</sup> Copyright 2010, Wiley-VCH..... 4
- Figure 1.2 Digital images of aqueous solutions of gold nanospheres (upper panels) and gold nanorods (lower panels). Corresponding TEM images of the nanoparticles are shown; all scale bars corresponding to 100 nm. Reprinted with permission from <sup>46</sup> (Murphy, C. J.; Gole, A. M.; Stone, J. W.; Sisco, P. N.; Alkilany, A. M.; Goldsmith, E. C.; Baxter, S. C., Gold Nanoparticles in Biology: Beyond Toxicity to Cellular Imaging. *Accounts of Chemical Research* **2008**, *41* (12), 1721-1730). Copyright 2008, American Chemical Society ..... 7
- Figure 1.3 Examples of multi-component nanomaterials: (a - d) core/shell structure spheres, (e) film coated with nanoparticles, (f, g) heterodimer, (h) crystal with attached nanosphere, (i) cross section through alloyed metal particle showing disordered nature of atomic occupancies, (j) cross section through nanoparticle composed of an intermetallic compound showing ordered atomic occupancy, (k) core/shell structure rod, (l, m) dimer with incoherent and coherent crystalline interface between the parts, respectively, (n) nanorods with overgrowth of another metal at the rod ends, (o) nanoparticles on nanorods, (p) multi-segment nanowires, (q) “nanotadpole”. Reprinted with permission from <sup>68</sup> (Cortie, M. B; McDonagh, A. M. , Synthesis and optical properties of hybrid and alloy plasmonic nanoparticles. *Chemical reviews*, **2011**, *111*, 3713-3735). Copyright 2011, American Chemical Society. .... 14
- Figure 1.4 The schematic shows different graphitic forms. Graphene is a 2D building material for carbon materials of all other dimensionalities. It can wrap up into 0D buckyballs, roll into 1D nanotubes or stack into 3D graphite. Reprinted by permission from Macmillan Publishers Ltd: (The rise of graphene) *Nature* <sup>87</sup> Copyright 2007. .... 20
- Figure 1.5 Sequence of transmission electron microscopy images characteristic of the interaction of Au/C core-shell nanoparticles in the temperature range between 400 and 800 °C. Reprinted with permission from <sup>99</sup> (Sutter, E.; Sutter, P.; Zhu, Y. M., Assembly and interaction of Au/C core-shell nanostructures: In situ observation in the transmission

electron microscope. Nano Letters 2005, 5 (10), 2092-2096). Copyright 2005 American Chemical Society .....	26
Figure 1.6 Schematic of different cases of scattering (Rayleigh scattering, Stokes scattering, and Anti-Stokes scattering) .....	28
Figure 2.1 Digital image showing the set-up for synthesis gold nanoparticles at (a) room temperature, and (b) high temperature. Schematic showing the parameter study of (c) single-step method and (d) seed-growth method.....	34
Figure 2.2 (a) Digital image showing Jupiter III reactive ion etcher, (b) schematic indicating gold nanoparticles are oxidized by O <sub>2</sub> plasma.....	39
Figure 2.3 Schematic representing of chemical vapor deposition process for graphene encapsulating noble metal nanoparticles .....	41
Figure 2.4 Digital images of Model 1021 plasma cleaner and the schematic shows sample stage. ....	47
Figure 2.5 Digital images of (a) FE-SEM JEOL-7000 for SEM, (b) Tecnai F-20 for TEM, (c) Kratos Axis for XPS, and (d) Bruker Senterra for Raman. ....	50
Figure 3.1 TEM images of AuNPs (table 2.1, sample 1-7) synthesized at different temperatures: (a, b) 4 °C, (c) 25 °C, (d) 50 °C, (e, f) 70 °C, (g, h) 90 °C, (i, j) 110 °C, (k, l) 130 °C, and (m) histogram showing AuNPs size distributions. ....	58
Figure 3.2 Reaction Gibbs free energy ( $\Delta rG$ ) of reduction reaction of HAuCl <sub>4</sub> with NaBH <sub>4</sub> at different temperature. ....	60
Figure 3.3 TEM images of AuNPs (table 2.1, sample 8-10) synthesized using different metal salt (HAuCl <sub>4</sub> .3H <sub>2</sub> O) concentration: (a, b) $5 \times 10^{-6}$ M, (c, d) $5 \times 10^{-4}$ M, (e, f, g, h) $5 \times 10^{-3}$ M, and (i) histogram showing AuNPs size distributions.....	62
Figure 3.4 TEM images of AuNPs (table 2.1, sample 11-14) synthesized from different surfactants: (a, b) PVP, (c, d, e) KBr, (f, g) MPTMS, (h, i) PVA, and (j) histogram showing AuNPs size distributions.....	64
Figure 3.5 TEM images of AuNPs (table 2.1, sample 15-17) synthesized using different CTAB concentration: (a, b) 0 M, (c, d) 0.0074 M, (e, f) 0.8 M, and (g) histogram showing AuNPs size distributions.....	65
Figure 3.6 TEM images of AuNPs (table 2.1, 18-20) synthesized for different growth duration: (a) 0.25 h, (b) 0.5 h, (c) 24 h, and (d) histogram showing AuNPs size distributions.	68

Figure 3.7 The change of gold nanoparticle size with different parameters: (a) temperature, (b) metal salt concentration, (c) surfactant type, (d) CTAB concentration, and (e) synthesis duration.....	70
Figure 3.8 TEM images of AuNPs (table 2.2, sample 21-23) synthesized at 130 °C and then quenched at (a, b, c) 10 °C, (d, e) 0 °C, (f, g, h, i) -20 °C, and (j) histogram showing AuNPs size distributions.....	72
Figure 3.9 (a) A schematic showing the color change of a typical seed-growth process. (b - e) TEM images of Au seeds (table 2.3) and (f) a histogram showing AuNPs size distributions.....	75
Figure 3.10 TEM images of AuNPs (table 2.4, sample 1-3) synthesized using different CTAB concentrations: (a, b, c) 0 M, (d, e) 0.075 M, (f, g) 0.5 M, and (h) histogram showing AuNPs size distributions.....	77
Figure 3.11 TEM images of AuNPs (table 2.4, sample 4-6) synthesized by adding different amount of seed solution: (a, b) 0.0005 mL, (c, d) 0.0625 mL, (e, f) 0.125 mL, and (g) histogram showing AuNPs size distributions.....	79
Figure 3.12 TEM images of AuNPs (table 2.4, sample 7-8) synthesized at different temperatures: (a, b) 90 °C, (c, d) 130 °C and (e) histogram showing AuNPs size distributions.....	82
Figure 3.13 TEM images of AuNPs (table 2.4, sample 9-11) synthesized for different growth duration: (a, b) 1h, sample 9; (c, d) 9 h, sample 10; (e, f) 24 h, sample 11, and (i) histogram showing AuNPs size distributions.....	83
Figure 3.14 The change of AuNPs size with different parameters: (a) CTAB concentration, (b) seed amount, (c) temperature, (d) growth duration.....	84
Figure 3.15 TEM images of PdNPs (table 2.5, sample 1-4) synthesized using different PVP concentrations: (a, b) 0.261 mM, (c, d) 0.522 mM, (e, f) 1.044 mM, (g, h) 2 mM, and (i) histogram showing PdNPs size distributions.....	87
Figure 3.16 TEM images of PdNPs (table 2.5, sample 5-7) synthesized using different metal salt (PdCl <sub>2</sub> ) concentration: (a, b) 0.05 mM, (c, d) 0.25 mM, (e, f) 0.5 mM, and (g) histogram showing PdNPs size distributions.....	88
Figure 3.17 TEM images of PdNPs (table 2.5, sample 8-9) synthesized at different temperatures: (a, b) 125 °C, (c, d) 150 °C, and (e) histogram showing PdNPs size distributions....	89
Figure 3.18 TEM images of PdNPs (table 2.5, sample 10-12) synthesized for different growth duration: (a, b) 1 h, (c, d) 6 h, (e, f) 10 h, and (g) histogram showing PdNPs size distributions.....	90

Figure 3.19 The change of PdNPs size with different parameters: (a) PVP concentration, (b) metal salt concentration, (c) temperature, (d) synthesis duration.....	91
Figure 3.20 (a - d) TEM images of shape controlled PdNPs (table 2.5, sample 13), and (e) histogram showing PdNPs size distribution.....	93
Figure 3.21 TEM images of PtNPs (table 2.6, sample 1-3) synthesized using different metal salt ( $H_2PtCl_6$ ) concentration: (a, b) $1.93 \times 10^{-5}$ M, (c, d) $6.0 \times 10^{-4}$ M, (e, f) $1.93 \times 10^{-3}$ M, and (g) histogram showing PtNPs size distributions.....	96
Figure 3.22 TEM images of PtNPs (table 2.6, sample 5-7) synthesized using different PVP amount: (a, b) 0 g, (c, d) 1.2 g, (e, f) 2 g, and (g) histogram showing PtNPs size distributions.....	97
Figure 3.23 (a, b) TEM images of PtNPs (table 2.6, sample 8) synthesized at $150^{\circ}C$ , and (c) histogram showing PtNPs size distributions.....	98
Figure 3.24 (a, b)TEM images of PtNPs (table 2.6, sample 9) synthesized using $NaBH_4$ as reducing agent, and (c) histogram showing PtNPs size distributions.....	99
Figure 3.25 TEM images of PtNPs (table 2.6, sample 10-12) synthesized for different growth duration: (a, b) 1 h, (c, d) 10 h, (e, f) 24 h, and (g) histogram showing PtNPs size distributions.....	100
Figure 3.26 The change of PtNPs size with different parameters: (a) metal salt concentration, (b) PVP concentration, (c) temperature, (d) synthesis duration.....	101
Figure 3.27 (a - c) TEM images of shape controlled PtNPs (table 2.6, sample 13), and (d) histogram showing PtNPs size distributions.....	102
Figure 3.28 XPS spectra corresponding to AuNPs (a) before plasma oxidation and after (b) 15 min, (c) 30 min, (d) 45 min, (e) 60 min, (f) 75 min of plasma oxidation duration. <i>Note: AuNPs (table 2.1, sample 10) were dispersed on Si wafer by drop casting method.</i>	104
Figure 3.29 Deconvoluted XPS spectra (from figure 3.28), subtracted by linear background, and fitted with Au 4f peaks corresponding to AuNPs (a) before plasma oxidation and after (b) 15 min, (c) 30 min, (d) 45 min, (e) 60 min, (f) 75 min of plasma oxidation duration. <i>Note: AuNPs (table2.1, sample 10) were dispersed on unmodified Si wafer by drop casting method.</i>	105
Figure 3.30 Oxidation behaviors of AuNPs (table 2.1, sample 10) as a function of plasma duration, percentages of (a) $HAuCl_4$ , (b) $AuO_x$ , (c) Au corresponding to the calculation in table 3.7 .....	109

Figure 3.31 SEM images of AuNPs (table 2.1, sample 10) (a) before plasma oxidation and after plasma oxidation for b) 15 min, c) 30 min, d) 45 min, e) 60 min, and f) 75 min. And (g) histogram shows size distributions of gold nanoparticles. Note: AuNPs were dispersed on unmodified Si wafer by drop casting method. All scale bar stands for 100 nm ..... 111

Figure 3.32 XPS spectra corresponding to PdNPs (a) before plasma oxidation and after (b) 5 min, (c) 15 min, (d) 30 min, (e) 45 min of plasma oxidation duration. Note: Shape controlled PdNPs (table 2.5, sample 13) were dispersed on Si wafer by drop casting method ..... 113

Figure 3.33 Deconvoluted XPS spectra (from figure 3.32), subtracted by Shirley background, and fitted with Pd 3d peaks corresponding to PdNPs (a) before plasma oxidation and after (b) 5 min, (c) 15 min, (d) 30 min, (e) 45 min of plasma oxidation duration. Note: Shape controlled PdNPs (table 2.5, sample 13) were dispersed on Si wafer by drop casting method ..... 114

Figure 3.34 Oxidation behavior of shape controlled PdNPs as a function of plasma duration, percentages of (a) PdO, (b) Pd, and (c) PdO<sub>2</sub> corresponding to the calculation in table 3.9 ..... 118

Figure 3.35 XPS spectra corresponding to PtNPs (a) before plasma oxidation and after (b) 5 min, (c) 15 min, (d) 30 min, (e) 45 min of plasma oxidation duration. Note: Shape controlled PtNPs (table 2.6, sample 13) were dispersed on Si wafer by drop casting method ..... 120

Figure 3.36 Deconvoluted XPS spectra (from figure 3.35), subtracted by Shirley background, and fitted with Pt 4f peaks corresponding to PtNPs (a) before plasma oxidation and after (b) 5 min, (c) 15 min, (d) 30 min, (e) 45 min of plasma oxidation duration. Note: Shape controlled PtNPs (table 2.6, sample 13) were dispersed on unmodified Si wafer by drop casting method ..... 121

Figure 3.37 Oxidation behavior of shape controlled PtNPs (table 2.6, sample 13) as a function of plasma duration, percentages of (a) Pt, (b) PtO<sub>2</sub>, and (c) PtO corresponding to the calculation in table 3.11 ..... 125

Figure 3.38 (a) Schematic for the gold nanoparticles been oxidized, and thickness of oxide shell vs. plasma oxidation time for (b) AuNPs, (c) PdNPs, and (d) PtNPs ..... 127

Figure 3.39 (a, b) SEM images and (c - i) TEM images of graphene encapsulated AuNPs on Si wafer. Note: AuNPs (table 2.1, sample 10) were dispersed on unmodified Si wafer by drop-casting method and utilized to grow graphene shells ..... 129

Figure 3.40 TEM images of graphene encapsulated PdNPs on Si wafer. Note: PdNPs (table 2.5, sample 13) were dispersed on unmodified Si wafer by drop-casting method and utilized to grow graphene shells ..... 130

Figure 3.41 TEM images of graphene encapsulated PtNPs on Si wafer. Note: PtNPs (table 2.6, sample 13) were dispersed on unmodified Si wafer by drop-casting method and utilized to grow graphene shells. .... 131

Figure 3.42 A) XPS spectra corresponding to AuNPs (a) before plasma oxidation, (b) after 30 min of plasma oxidation, and (c) after 1 h of graphene growth. B) Deconvoluted XPS spectra subtracted by linear background and fitted with Au 4f peaks corresponding to AuNPs (a) before plasma oxidation, (b) after 30 min of plasma oxidation, and (c) after 1 h of graphene growth. (d) Deconvoluted XPS of C 1s after graphene growth. Note: AuNPs (table 2.1, sample 10) were dispersed on unmodified Si wafer by drop casting method. .... 134

Figure 3.43 Raman 3D mapping for AuNPs after graphene growth. (a) Raman spectroscopy of graphene encapsulated AuNPs, (b) 3D map for graphene structure on sample surface, (c) sample surface has been scanned, and (d) vertical view of the 3D map. Note: AuNPs (table 2.1, sample 10) were dispersed on piranha cleaned Si wafer by drop casting method. .... 137

Figure 3.44 Raman 3D mapping for PdNPs after graphene growth. (a) Raman spectroscopy of graphene encapsulated PdNPs, (b) 3D map for graphene structure on sample surface, (c) sample surface has been scanned, and (d) vertical view of the 3D map. Note: PdNPs (table 2.5, sample 13) were dispersed on piranha cleaned Si wafer by drop casting method. .... 138

Figure 3.45 Raman 3D mapping for PtNPs after graphene growth. (a) Raman spectroscopy of graphene encapsulated PtNPs, (b) 3D map for graphene structure on sample surface, (c) sample surface has been scanned, and (d) vertical view of the 3D map. Note: PtNPs (table 2.6, sample 13) were dispersed on piranha cleaned Si wafer by drop casting method. .... 139

Figure 3.46 SEM images of (a, b) Commercial AuNPs dispersed on MPTMS (12.4 mM) functionalized silicon wafer, (c, d) Commercial AuNPs dispersed on MPTMS (2 mM) functionalized silicon wafer, (e, f) synthesized AuNPs (table 2.1, sample 7) dispersed on MPTMS (2 mM) functionalized silicon wafer, (g) synthesized PdNPs (table 2.5, sample 8) dispersed on MPTMS, (h) synthesized PtNPs (table 2.6, sample 8) dispersed on MPTMS. .... 141

Figure 3.47 Raman spectroscopy for (a) Methylene-Blue (MB) dried on piranha cleaned silicon wafer by drop-casting, MB dried on silicon wafer decorated with (b) AuNPs, (c) PdNPs, (d) PtNPs. .... 143

# CHAPTER 1

## INTRODUCTION

### *1.1. Noble metal nanoparticles*

Nanomaterials are defined as materials with size smaller than 100 nm in at least one dimension.<sup>1</sup> Over the past two decades, metal nanoparticles have received significant attention due to different electronic, physical, and chemical properties from their bulk counterparts.<sup>2 3 4</sup> For metal, the mean free path of an electron at room temperature is 10 nm to 100 nm.<sup>5</sup> So, unusual effects would be observed when the size of metallic materials shrinks to nanoscale. For instance, noble metals such as gold, palladium, and platinum which are stable in bulk scale become active to the environment in nanostructure form.<sup>6 7 8</sup> Metal nanoparticles are widely used in chemical catalysis, optical, electronic, magnetic devices, and biological systems.<sup>9 10 11 12 13</sup>

In addition to the materials composition, the characteristics of nanoparticles are also size- and shape-dependent, including their optical, electronic, and catalytic properties.<sup>10</sup> Nanomaterials are consisted of a few hundreds to thousands of atoms or molecules (1 nm is about 6 times the atom size of Au and about 4.5 times the atomic spacing in noble metals) as a single entity, the shapes of the nanoparticle are governed by the surface-energy factor.<sup>14</sup>

Significant amount of work has been devoted to the synthesis of metal nanospheres, and the particle size distributions can be achieved within the 10% of the mean diameter.<sup>15 16</sup> Basically, there are two approaches to synthesize nanoparticle which are classified as “top-down” and “bottom-up”. Top-down approach starts from bulk materials, using physical and lithographic principles of micro- and nanotechnology to achieve nanostructures.<sup>17</sup> While bottom-

up approach is governed primarily by chemical synthesis principles to assemble ionic, atomic, or molecular units through various processes in the nanometer range.<sup>18, 19</sup> Top-down approach usually requires state-of-the-art instruments, the drawback is that it is time consuming and still cannot efficiently manipulate particle morphology at nanoscale. On the other hand, bottom-up approach is more popular because it allows, in principle, the design and formation of nanoparticles of any size and morphology. Meanwhile, it is inexpensive, versatile, and technologically easy to implement for fabricating a wide variety of nanoparticles.

Colloid-chemical approach, often referred to solution phase synthesis routes, is an important method in bottom-up approach, to which much work has been devoted. However, there is still a significant challenge in understanding and precisely predicting nanoparticle morphology from a given set of synthesis conditions. That is because synthesis parameters such as metal salt concentration, surfactant type and amount, addition of additives, impurities, and temperature always interact with each other and contribute to the morphology of final products.<sup>20</sup>

### 1.1.1 Types of nonspherical noble metal nanoparticles

Nanomaterials can be classified according to their composition and morphology. Nonspherical nanomaterials can be divided into 1D, 2D, and 3D structures depend to their major growth direction: For 1D nanoparticles, the major growth occurred in one-dimension and confined in two dimensions, resulting in nanoscale rods,<sup>21</sup> tubes,<sup>22</sup> and wires;<sup>23</sup> one dimension is confined for 2D nanoparticles, generates different shapes such as plates,<sup>24</sup> discs,<sup>25</sup> ribbons,<sup>26</sup> and belts.<sup>27</sup> In case of 3D structure nanoparticles, major growth occurred in all three dimensions, produces tetrahedral, octahedral, decahedra, icosahedra,<sup>28</sup> cubes,<sup>29</sup> cages,<sup>30</sup> or branched

nanoparticles such as bi-, tri-, tetra-pod, bumpy, or star shapes.<sup>20</sup> Figure 1.1 shows some examples of different shapes nanoparticles.<sup>14</sup>

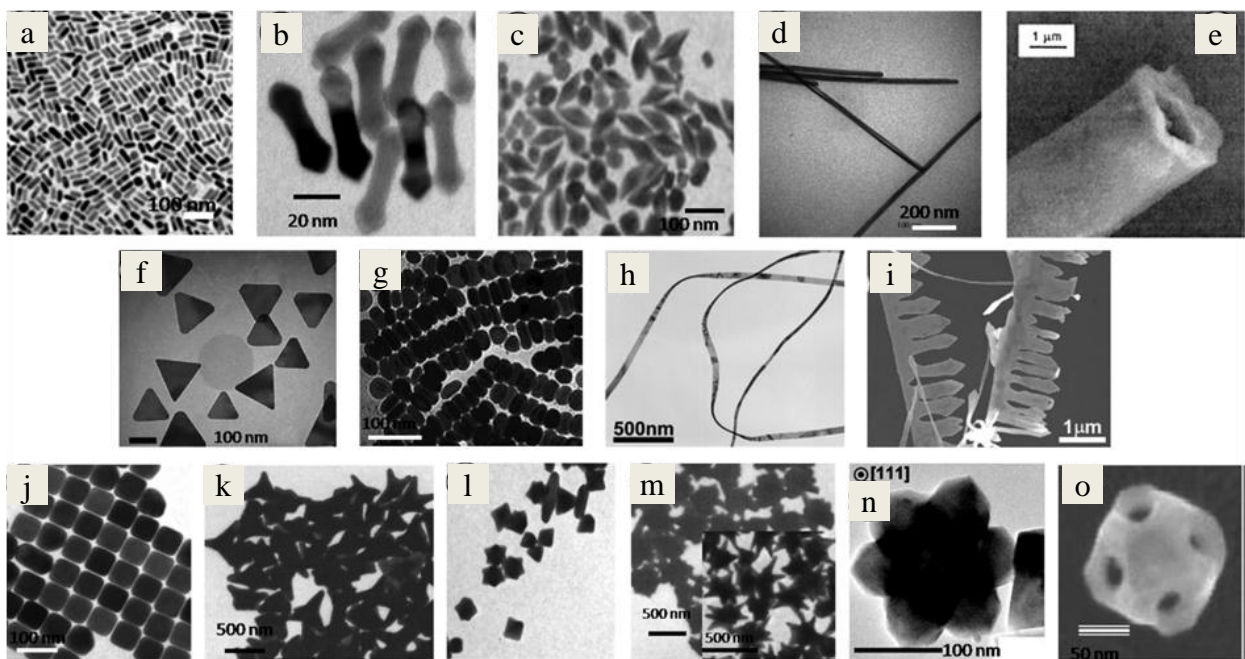


Figure 1.1 A few examples of different shapes 1D, 2D, 3D noble metal nanoparticles synthesized through solution-based approach. The first row shows the TEM (a - d) or SEM (e) images of 1D structure nanoparticles: (a) nanorods, (b) nanodumbbells, (c) nanobipyramids of Au/Ag, (d) silver nanowires, and (e) gold nanotube. The middle row shows some 2D structure nanoparticles: TEM images of (f) triangular gold nanoplates, (g) silver nanodisks, and (h) gold ribbons; SEM image of (i) gold belts. The last row shows some typical 3D structures: TEM images of (j) nanocubes, (k) nanotepropods, and (l - m) star-shaped gold nanoparticles, (n) silver nanohexapods, SEM image of an (o) Au-Ag nanocage. Reprinted with permission from <sup>14</sup> Copyright 2010, Wiley-VCH.

### 1.1.2 Synthesis of nonspherical noble metal nanoparticles

Design and synthesis of materials with tailored size and shape is a fundamental goal of materials science because it is well recognized that properties of nanoparticles are significantly depend on their composition, size, shape, structure, and crystallinity.<sup>31</sup> The solution based approaches (colloid-chemical methods) of nonspherical noble metal nanoparticles principally involves the reduction of metal salts or decomposition of metallic compounds in aqueous or organic solvents in the presence of stabilizer and shape-control additives such as surfactant, ligand, polymer, and foreign ion.<sup>32, 33, 34, 35</sup>

Nanoparticles with a wide variety of morphologies can evolve under a certain condition; meanwhile, particles with a certain kind of morphology can also be obtained through different methods.<sup>20-36</sup> Popular ways of developing nonspherical nanoparticles include seed-growth approach,<sup>37</sup> high-temperature synthesis,<sup>38</sup> template-based (electro-) chemical synthesis,<sup>39</sup> photochemical techniques.<sup>40</sup> In seed-growth approach, fine metal nanoparticles (size < 10 nm) are first synthesized by strong reducing agent (e.g. NaBH<sub>4</sub>). Subsequently, these fine metal nanoparticles are used as seeds that added into solution containing the same or different metal ions. And particles with certain morphology can be obtained by heterogeneous nucleation of metal ions at the surface of seeds. Chemicals with weak reducing properties such as citric acid, alcohol, polymers with hydroxyl group (e.g. PVP, PVA), and dimethylformamide (DMF)<sup>41</sup> are capable to reduce metal ions at elevated temperature. At high temperature, those chemicals will act as both solvent/stabilizers and reducing agent. Template-based (electro-) chemical synthesis is a popular method for nanoparticles shape control. Soft templates include self-assembled chemicals and liquid-crystalline media. For instance, Cetyltrimethylammonium bromide (CTAB), which contains hydrophobic carbon chain and hydrophilic head, can form micelles in

aqueous solution, containing long water channels as template for the formation of nanowires.<sup>42</sup> Carbon nanotubes and porous membrane (e.g. amorphous alumina) are examples of hard template.<sup>43 44</sup> In this case, precursor solution wets the inner wall of template channels, followed by the deposition of metal on the template. The reduction can be classified as electro-less and electrochemical reduction. The former involves the use of chemical reducing agent to provide electrons, whereas electrochemical reduction applies potential as reaction force to deposit metal from solution onto a desired surface of template. Another template is nanoparticles with particular shapes. In this case, template particles usually sacrifice themselves to reduce object metals on their surface.<sup>45</sup> So, template materials do not exist in final product or at least not exist on the surface of product, and this is the difference between using nanoparticles as template and using nanoparticles as seeds.

### 1.1.3 Gold nanoparticles

As noble metal, gold has been an object of luxury for its ornamental value. As a matter of fact, the history of synthesis of gold nanoparticles have been over 2000 years in medias including glasses, salt matrices, polymers, the gas phase and in water.<sup>36</sup> Gold is not always golden but varies with conditions. With different size, shape, aggregation degree and local environment, the color of gold nanoparticles can varies from red to purple, blue, and green. Some examples of gold colloid solutions with different colors influenced by different morphology of containing gold nanoparticles are shown in figure 1.2.<sup>46</sup>

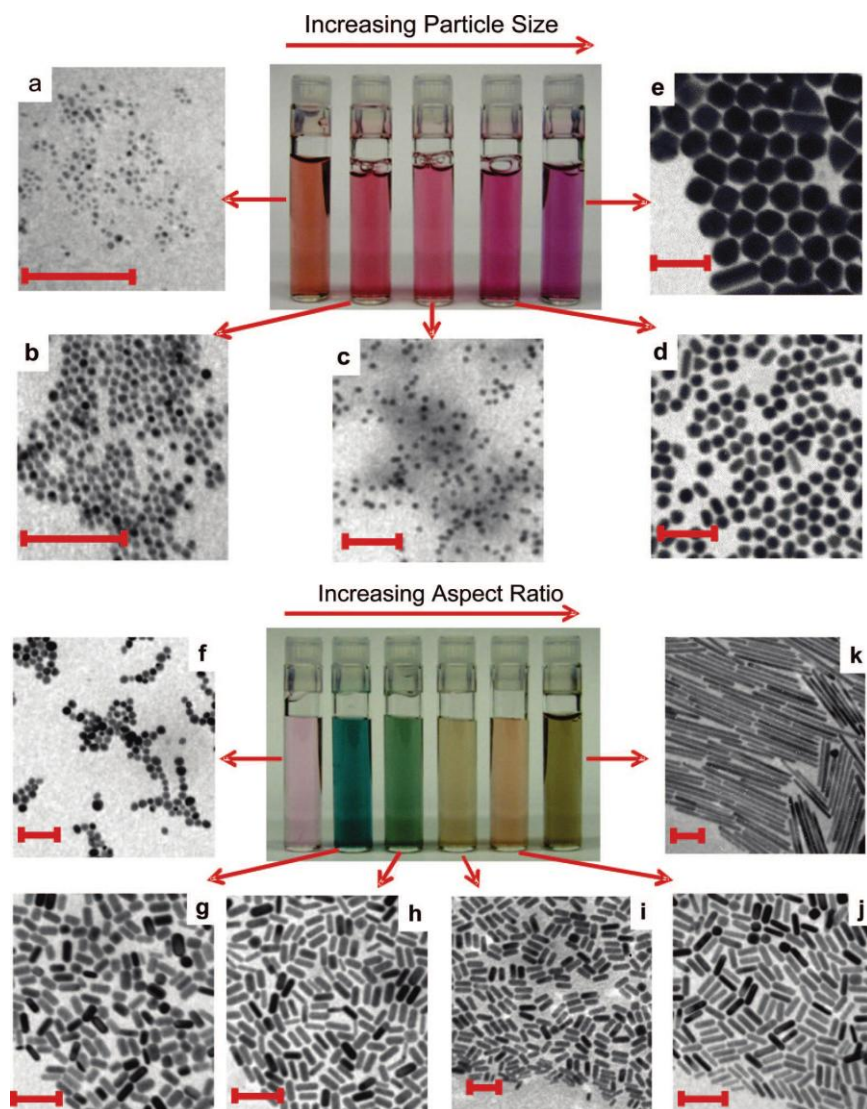


Figure 1.2 Digital images of aqueous solutions of gold nanospheres (upper panels) and gold nanorods (lower panels). Corresponding TEM images of the nanoparticles are shown; all scale bars corresponding to 100 nm. Reprinted with permission from <sup>46</sup> (Murphy, C. J.; Gole, A. M.; Stone, J. W.; Sisco, P. N.; Alkilany, A. M.; Goldsmith, E. C.; Baxter, S. C., Gold Nanoparticles in Biology: Beyond Toxicity to Cellular Imaging. *Accounts of Chemical Research* **2008**, *41* (12), 1721-1730). Copyright 2008, American Chemical Society.

The phenomenon that gold nanoparticles can appear in different color is attributed to size effect. If size is smaller than the wavelength of visible light (about 400 ~750 nm), a collective oscillation of electrons known as “plasma oscillations” can be generated on the surface of metal nanoparticles when particles are irradiated with light at certain frequencies. Such collective oscillations govern the optical properties of small metal nanoparticles.<sup>46</sup> For metal nanoparticles, these plasma frequencies are sensitive to the dielectric nature.<sup>47</sup> The frequency of this oscillation for gold lies in the range of visible light wavelength. By changing size, shape, degree of aggregation, and local environment, the plasmon frequency changes with the variation of dielectric constant,<sup>48</sup> so gold nanoparticles will appear different color.

Some approaches of synthesis of gold nanoparticles include Turkevich method, Brust method, Martin method, and seed-growth method. Turkevich method was pioneered by Turkevich and his coworkers in year 1951 and refined by Frens in year 1973.<sup>49, 50</sup> It simply adds chlorauric acid into boiled water, and then adds small amount of sodium citrate solution to reduce gold ion to produce monodispersed spherical gold with size around 15 nm.

Brust method was discovered by Brust et al.<sup>51</sup> in year 1994 for synthesis small gold nanoparticles with size around 2 nm. In this method, toluene is used as solvent, sodium borohydride is reducing agent, and tetraoctylammonium bromide (TOAB) is stabilizer for produced gold nanoparticles. Since the bind between TOAB and gold nanoparticles does not strong enough, the solution will aggregate after a few weeks. To solve this problem, a stronger binding agent, e.g. a thiol, can be added after reaction completed to produce a stable solution.

Martin Method is an efficient method for colloidal gold nanoparticles chemical synthesis and dispersion, discovered by Eah and co-workers<sup>52</sup> in year 2010. The size of colloidal gold nanoparticles is tunable from 3.2 to 5.2 nm diameter. 2D monolayer films of close-packed gold

nanoparticles can be effectively fabricated to any substrate without any limit in size. In this method, HAuCl<sub>4</sub> and NaBH<sub>4</sub> are first stabilized by HCl and NaOH, respectively. Then HAuCl<sub>4</sub> is reduced by NaBH<sub>4</sub> in aqueous solution. Subsequently, acetone, hexane and 1-dodecanethiol (DDT) are added into the mixture solution, and the vial containing solution is shaken vigorously for 30 s. As-prepared gold nanoparticles are coated with monolayer of DDT, and phase-transferred to hexane, while all the reaction byproducts remain in the water-acetone phase. A monolayer of gold film can form by adding prepared hexane-gold solution into a toluene droplet. Negatively charged gold nanoparticles coated with hydrophobic DDT molecules will 2D self-assemble at the air-liquid interface of the droplet, and the monolayer film of close-packed gold nanoparticles can be obtained after toluene droplet dried.

Seed-growth method is widely used for size- and shape- control of gold nanoparticles, which is pioneered by Murphy and the research group.<sup>53</sup> In this method, fine gold nanoparticles were first synthesized and then used as nucleus in the surfactant-directed growth step. By varying the experimental parameters in the growth procedure, they produced gold nanoparticles with different shapes such as rod, rectangle, hexagon, cub, and star. However, on the one hand, the growth conditions need to be precisely controlled, and it requires extensive separation of different shapes nanoparticles. On the other hand, it is also difficult to fabricate small seeds with a narrow size distribution. In order to increase the proportion of objective product for synthesis gold nanorods, they find out that slightly increasing solution pH from 2.8 to 3.5 can help to achieve this goal.<sup>54</sup> They postulated that since the first pKa of ascorbic acid (reducing agent) is 4.1, the increased pH condition favored the ascorbate monoanion over the acid or dianion. The ascorbate monoanion absorbed better to the five-fold {111} end faces of gold, effectively reduced Au<sup>III</sup> and Au<sup>I</sup> intermediates there and resulted in nanorods structure.

#### 1.1.4 Palladium nanoparticles

The unique properties of palladium account for its widespread use. As its bulk material is stable and does not react with oxygen at normal temperatures, palladium can catalyze a large number of reactions when its size is in nanoscale.<sup>7</sup> Notable examples include alkene hydrogenation, alcohol oxidation, low-temperature reduction of automobile pollutants, petroleum cracking, and CO oxidation.<sup>55, 56, 57, 58</sup> Palladium is also used in electronics for making the multilayer ceramic capacitor.<sup>59</sup> Moreover, palladium can absorb up to 900 times to its own volume of hydrogen at room temperature and atmospheric pressure, which gives it potential for hydrogen storage.<sup>60</sup> However, the implement of palladium based hydrogen storage would be difficult to achieve due to the expensive cost of palladium.

The activity and selectivity of a catalyst can be enhanced by the exposure of specific crystal facets that are intrinsically more active to some particular reactions. For instance, {100} facets of cubic palladium nanoparticles have a higher catalytic activity than {111} facets in CO oxidation.<sup>35</sup> The shape of nanoparticles are governed by their exposed facets, therefore ways of controlling the size and shape of palladium nanoparticles have attracted significant attention in order to achieve high performance in various catalytic applications.

Polyol synthesis has been a popular method of preparing metal nanoparticles with well-defined shapes.<sup>18</sup> Polyols, for example ethylene glycol (EG), can dissolve many metal salts, and can react as reducing agent at high temperature. The drawback of this method is that shapes of nanoparticles product are usually restricted to cuboctahedrons or truncated cubes because of the fast reduction and growth rate.<sup>61</sup> Moreover, this approach is also troubled by the irreproducible results due to the presence of even trace amounts of impurities in the system.

Therefore, a water-based system was adopted in the synthesis of palladium nanoparticles. It does not involve toxic organic solvents and high-purity of water is more easily accessible. Instead of EG, low reducing power chemicals such as L-ascorbic acid (AA), citric acid, and alcohol can be used as reducing agents which are favorable to manipulate the reduction kinetics.<sup>34-62</sup> Xia et al. synthesized palladium nanoparticles with well-controlled shapes in aqueous system. By adding haloids ions, they can selectively promote the formation of {111} and {100} facets and obtained shapes include truncated octahedron, icosahedrons, decahedron, hexagonal and triangular plates, and cube.<sup>29</sup>

### 1.1.5 Platinum nanoparticles

As a pure metal, bulk platinum does not oxidize at any temperature and has an excellent resistance to corrosion. This property makes platinum be widely used as noble metal electrode in electrochemistry.<sup>63</sup> The other most important application for platinum is as a catalyst in a number of separate processes, especially in automobiles industry. Platinum powder allows complete combustion of unburned hydrocarbons from the exhaust, and converts them into harmless carbon dioxide and water.<sup>7</sup>

Many efforts have been involved to make various shapes of platinum nanoparticles in order to investigate their influence on catalytic activity. On this point, uniformly dispersed platinum nanoparticles are needed to quantify the catalytic influences. Similar with the morphology control of other noble metal nanoparticles, capping agents such as CTAB, PVP, KBr, KCl, AgNO<sub>3</sub> are usually used to favor the growth of particular facets. Ahmadi and co-workers<sup>64</sup> reported sizes and shapes control of platinum nanoparticles by changing the ratio of capping polymer (sodium polyacrylate) to the concentration of metal salt. Yang et al.<sup>38</sup> also

demonstrated that cuboctahedrons, cubes, and porous platinum nanoparticles can be obtained by adjusting the reduction method, and silver ion plays a significant role in morphology control for platinum nanoparticles synthesis.

## *1.2 Multi-component nanomaterials*

Starting from the preparation of single component nanomaterials, nanotechnology is moving toward manipulating and tailoring more and more sophisticated structures named as multicomponent and heterostructured nanomaterials. In nanoscale, composition, size, and shape all play critical roles in determining nanostructures' physical and chemical properties such as wave functions, plasmon resonances, and catalytic activities.<sup>65 66</sup> By incorporating components of intrinsically different functionality, we may create novel functional materials which not only maintain functions from each component, but also show synergistic properties found in neither of the constituents. For example, by coating a core particle with other materials, colloidal stability may be improved or the core material can be protected from being oxidized.<sup>67</sup>

Multicomponent nanomaterials can be classified according to the way constituents being hybridized, such as alloyed nanoparticles, nanoparticles hybrid with nanowires or nanotubes, and core/shell nanoparticles, multisegment nanowires. Some of which are depicted in Figure 1.3.<sup>68</sup>

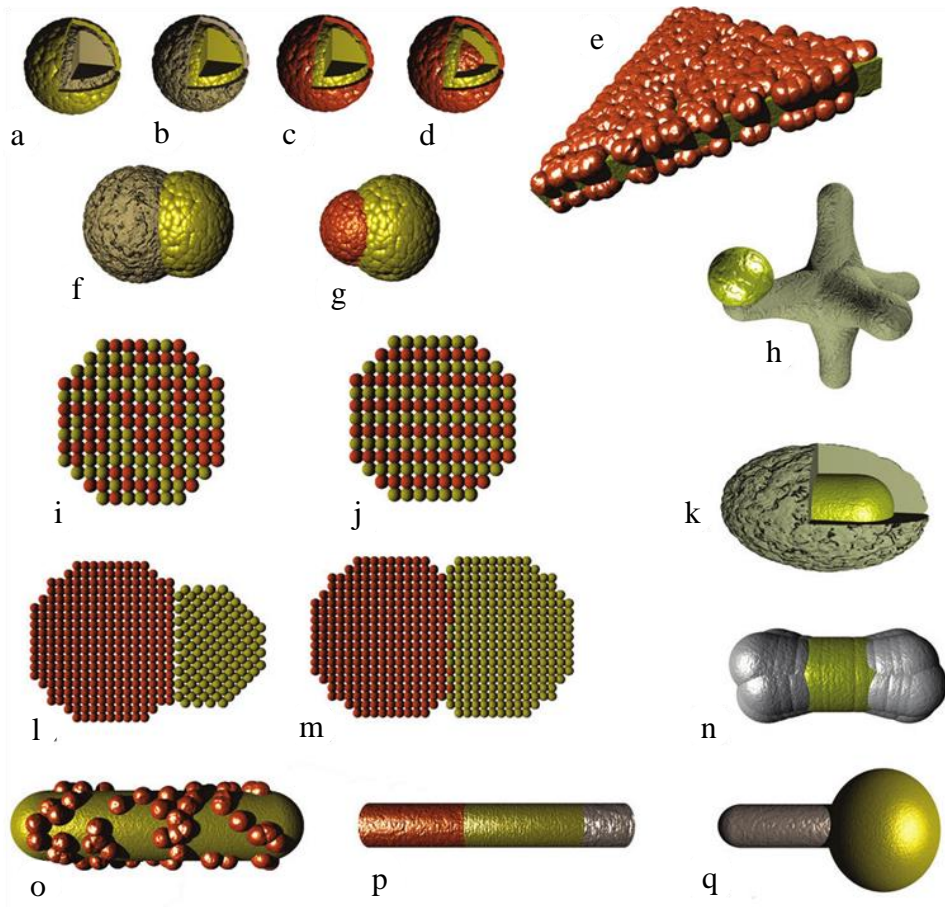


Figure 1.3 Examples of multi-component nanomaterials: (a - d) core/shell structure spheres, (e) film coated with nanoparticles, (f, g) heterodimer, (h) crystal with attached nanosphere, (i) cross section through alloyed metal particle showing disordered nature of atomic occupancies, (j) cross section through nanoparticle composed of an intermetallic compound showing ordered atomic occupancy, (k) core/shell structure rod, (l, m) dimer with incoherent and coherent crystalline interface between the parts, respectively, (n) nanorods with overgrowth of another metal at the rod ends, (o) nanoparticles on nanorods, (p) multi-segment nanowires, (q) “nanotadpole”. Reprinted with permission from <sup>68</sup> (Cortie, M. B; McDonagh, A. M., Synthesis and optical properties of hybrid and alloy plasmonic nanoparticles. *Chemical reviews*, **2011**, *111*, 3713-3735). Copyright 2011, American Chemical Society.

Preparation of multi-component nanomaterials involves several strategies including deposition-precipitation, galvanic replacement, coprecipitation, templated growth.<sup>45, 69</sup> Chen et al.<sup>70</sup> synthesized Fe<sub>3</sub>O<sub>4</sub>/TiO<sub>2</sub> core/shell nanoparticles (with estimated size ~50 nm), and employed these magnetic nanoparticles to selectively concentrate phosphopeptides from mixture solutions for further analyzing. Titanium dioxide nanoparticles have high trapping capacities toward phosphopeptides. The combination of magnetic property from Fe<sub>3</sub>O<sub>4</sub> nanoparticles allows the core/shell nanoparticles that are conjugated with target peptides can be isolated readily from sample solutions. The lowest detectable concentration is much lower than that which can be achieved from other methods.

Tresback and co-workers fabricated Au-NiO-Au multi-segment nanowires using template-based method.<sup>71</sup> They electro-deposited a small segment of Ag in anodic aluminum oxide (AAO) template, and subsequently deposited Au, Ni, Au segment from the corresponding electrolytes. After dissolving Ag nanowire segment and AAO template by HNO<sub>3</sub> and NaOH, respectively, multi-segment nanowires were collected and dispersed on an oxidized silicon substrate, followed by annealing at 600 °C in air to fully oxidize the nickel segment to NiO. The authors claimed that these Au-NiO-Au multisegment nanowires have a potential to be integrated as chemical nanosensors into nanoelectronics devices in the future.

Qu and co-workers decorated carbon nanotube (CNT) with size and shape controlled noble metal nanoparticles in a novel approach.<sup>72</sup> They found that even without adding foreign capping reagents, cubic platinum nanoparticles can be synthesized by galvanic displacement reaction between an aqueous solution of metal salt and copper foil substrate. Actually, it was Cu<sup>2+</sup> ions, which were produced in the galvanic displacement reaction between metal salt and copper foil, acted as an in situ capping agent and regulated the shape of synthesized platinum

nanoparticles. When they exposed copper foil-supported CNTs to a certain concentration of aqueous solution of  $K_2PtCl_4$  with and without the addition of  $CuCl_2$ , cubic and spherical Pt nanoparticles, respectively, can formed on CNTs. These nanoparticles-nanowires hybrid structures may further applied in a wide range including fuel cell, sensing, optoelectronics, and catalytic systems.

Another example of hybrid structure consisting nanoparticles decorated on the surface of films. Lu et al.<sup>73</sup> reported the distribution of silver nanoparticles onto graphene oxide sheets. In this case, Hummers method<sup>74</sup> was used to synthesize graphene oxide sheets. The aerosol silver nanoparticles were synthesized through physical vaporization of an Ag wire, and subsequently decorated onto the surface of graphene oxide sheets by electrostatic force directed assembly technique at room temperature. The interaction between assembled silver nanoparticles and graphene oxide sheets was studied by annealing the hybrid structure in Ar atmosphere at different temperature. The author claimed that Ag nanoparticles were attached on graphene oxide sheets through van der Waals forces. This noncovalent nature of the adhesion is potentially beneficial for electronic and optoelectronic applications of the multi-component nanomaterials.

### *1.3 Oxidation of noble metal nanoparticles*

Noble metals such as gold, palladium, and platinum are widely used in the field of ornament. Bulk gold is oxidation-resistant in air or molecular oxygen even at elevated temperatures. Its chemical inertness can be attributed to the high value of the enthalpy of oxygen chemisorptions to form gold oxide  $\text{Au}_2\text{O}_3$  ( $\Delta H=+19.3 \text{ kJ/mol}$ ).<sup>75</sup> However, the catalytic activity of gold nanoparticles (e.g. their activity for the low-temperature oxidation of CO and  $\text{C}_3\text{H}_6$  epoxidation)<sup>76, 77</sup> has been found experimentally, formation of adsorbed oxygen species on the surface of gold nanoparticles is involved in these reactions. Since the unique behavior of gold catalysts is mainly associated with the nature of adsorbed oxygen, it is critical to study the structure and the nature of the bond between oxygen and the gold surface. It is also reported that PdO is more active than Pd for the catalytic combustion of methane.<sup>78</sup> In this context, the investigation of oxygen species on the surface of noble metals is important in numerous fields such as surface science, corrosion resistance, and catalysis.

Several methods have been suggested to oxidize noble metal materials such as oxygen adsorption at high temperatures and pressures,<sup>79</sup> oxidation by ozone,<sup>80</sup>  $\text{NO}_2$ , and atomic oxygen,<sup>81</sup> electrochemical oxidation,<sup>82</sup> oxygen plasma treatment.<sup>83</sup> In these methods, plasma treatment at low temperatures is an efficient approach, and it has been widely involved in the study of noble metal oxides.<sup>83, 84, 85</sup> In addition, this treatment induced many active oxygen atoms interact with the metal surface, and potentially lead to surface disordering and the formation of defects.

The stability of noble metal oxide also attracted the interest of researchers. Tsai and co-workers<sup>83</sup> reported the instability of gold oxide formed on a gold film by oxygen plasma treatment. In year 2008, Ono et al.<sup>75</sup> indicated that the thermal stability of  $\text{Au}_2\text{O}_3$  on gold

nanoparticles depends on the size of particles, as well as on supporting substrates. They observed that gold oxide is more stable on  $\text{SiO}_2$  than using  $\text{TiO}_2$  as substrates, and nanoparticles with diameter around 1.5 nm would be easier to be reduced than larger clusters. They suggested that there are two different oxygen species present: gold oxide on surface as well as on subsurface. The surface gold oxide decomposes at temperatures below 600 K, whereas the subsurface gold oxide is stable above 600 K.

## *1.4 Noble metal nanoparticles/graphene heterostructure*

Hybrid nanomaterials with multi-components provide significant flexibility in design and manipulation. Among the list of materials, noble metal nanoparticles and graphene exhibit excellent properties, and the combination of these two materials can form building blocks in the frontier technology.

### 1.4.1 Graphene synthesis

Graphene is a two dimensional structure of  $sp^2$  bonded carbon atoms. The covalent  $sp^2$  bonds are hybridized from s,  $p_x$ , and  $p_y$  atomic orbitals, carbon atoms are bonded through  $120^\circ$  C-C-C bond, giving rise to a honeycomb crystal lattice.<sup>86</sup> The discovery of graphene exploded the interests of scientists because two-dimensional crystals were considered thermodynamically unstable in nature. Graphene is the fundamental structure of some carbon allotropes, by wrapping graphene we get zero-dimension (0-D) fullerenes, by rolling graphene we get single or multi-wall one-dimension (1-D) carbon nanotubes, by stacking graphene we obtain three-dimension (3-D) graphite or charcoal. Figure 1.4 shows 0-D, 1-D, and 3-D graphene structures formed by wrapping, rolling, and stacking two-dimension (2D) graphene sheets, respectively. Graphene also be well known due to its excellent in-plane electrical ( $\sim 10^4 \Omega^{-1}cm^{-1}$ ) and thermal ( $\sim 3000 Wm^{-1}K^{-1}$ ) conductivity, as well as its high mechanical stiffness (1060 GPa). Figure 1.4 shows some different graphitic forms.<sup>87</sup>

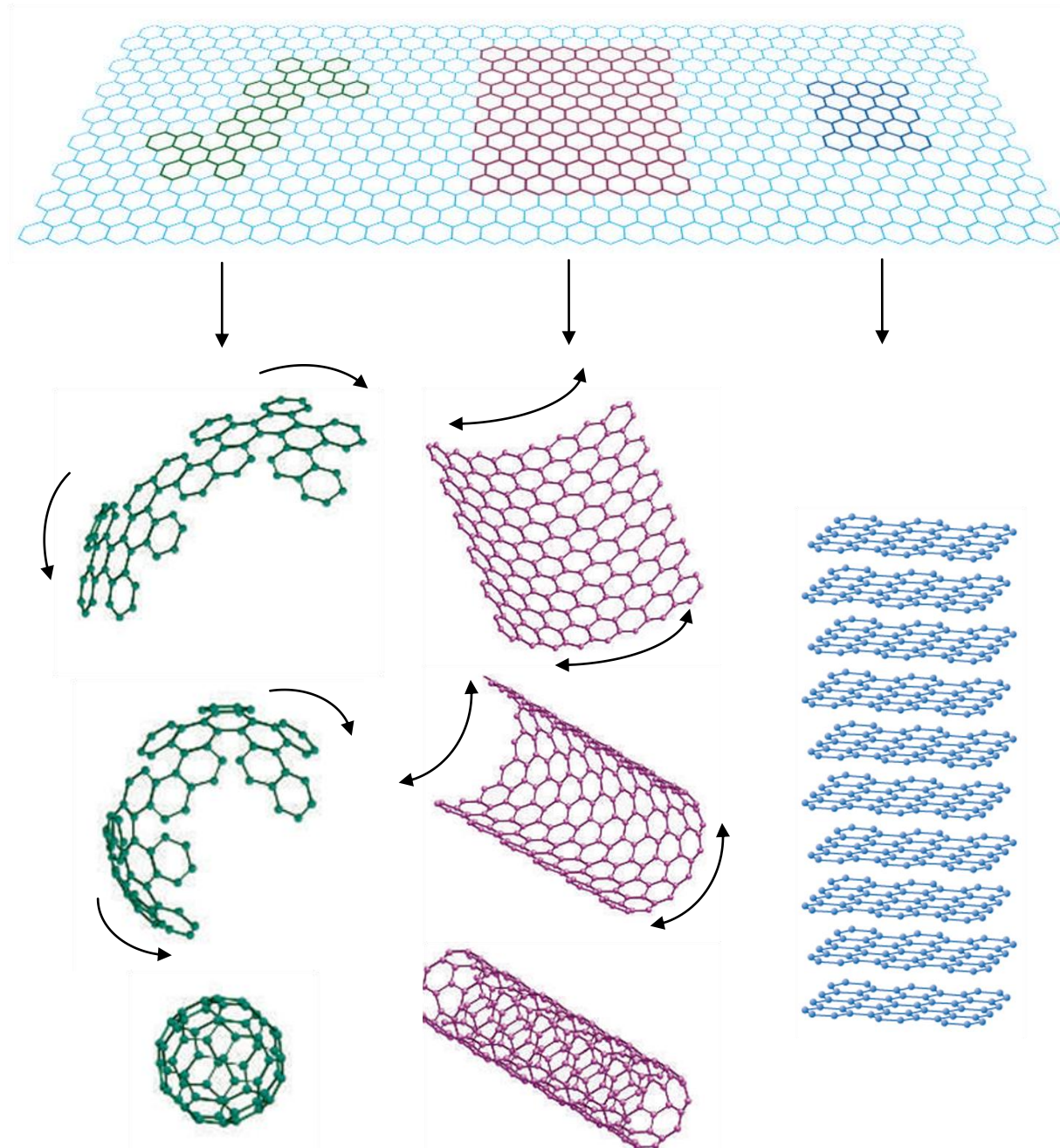


Figure 1.4 The schematic shows different graphitic forms. Graphene is a 2D building material for carbon materials of all other dimensionalities. It can wrap up into 0D buckyballs, roll into 1D nanotubes or stack into 3D graphite. Reprinted by permission from Macmillan Publishers Ltd: (The rise of graphene) Nature<sup>87</sup> Copyright 2007.

Several methods involved in synthesis graphene:

(1) Mechanical method. In 2004, Manchester group developed a technique to split graphite crystals into thinner pieces, resulting single- or few- layer flakes attached on adhesive tape.<sup>86</sup> The substrate (tape) can be etched away by acetone and those graphene flakes can be dispersed on silicon wafer. This approach is often referred to as a scotch tape method or drawing method. Although high quality samples can be obtained through mechanical exfoliation, the method suffered from time consuming and low-yield.

(2) Chemical approaches. Graphene can be synthesized by chemical reducing graphene oxide or cutting open carbon nanotubes. Graphene oxide, which is hydrophilic and could be exfoliated in water under ultrasonic treatment and heating, can serve as a precursor to graphene.<sup>88</sup> It has been documented that hydrazine can reduce graphene oxide films to yield graphene<sup>89</sup>. However, the quality of as-prepared graphene film is not as high as graphene produced from mechanical method due to incomplete removal of functional group on the surface of graphene oxide. Graphene nanoribbons can also be synthesized by unzipping of carbon nanotubes through concentrated sulfuric acid and potassium permanganate.<sup>90</sup>

(3) Graphene growth from organic precursor. Wu et al.<sup>91</sup> reported that disc-like nanosized graphene molecules can self-assemble at the solid-liquid interface. For instance, effective oxidative cyclodehydrogenation of branched oligophenylenes forms different shapes, sized and edge structures graphene molecules. Those graphene molecules have the potential to be converted into 1D carbon nanotubes by template-directed solid-state pyrolysis. The drawback of this synthesis method is the limit of size, because as the increases of molecular weight, side reactions occurred.

(4) Epitaxial growth on substrates. Chemical vapor deposition (CVD) method opens a new route to large-scale production of high quality graphene films. It has been observed that graphene can grow on the surface of semiconducting silicon carbide (SiC) by high-temperature annealing in vacuum<sup>92</sup>. This method was further developed by Emtsev and co-workers.<sup>93</sup> They reported that monolayer graphene films with larger domain sizes can be synthesized on Si-terminated SiC (0001) in an argon atmosphere, compared with vacuum graphitization. Metal substrates can also be used in chemical vapor deposition for the growth of graphene. Recently Bae et al.<sup>94</sup> reported an efficient method for the synthesis, transfer and doping of graphene at a large scale. Firstly, a roll of copper foil with size of 30 inches in the diagonal direction was inserted into a tubular quartz tube, and annealed 30 min at 1000 °C in H<sub>2</sub> atmosphere. The goal of annealing process is to increase copper grain size to yield higher quality graphene films. After annealing, a mixture gas of CH<sub>4</sub> and H<sub>2</sub> is then flowed through the copper foil for 30 min. Then the sample was rapidly cooled down to room temperature. The as-prepared graphene films on copper foil were subsequently transferred to a thermal release tape by applying soft pressure between two rollers. The synthesized graphene films have low sheet resistance and high optical transmittance, and this method, and this method gives the possibility to commercial produce large scale high quality graphene sheets.

#### 1.4.2 Chemistry of graphite

The chemistry of graphite (multi-layer graphene) can be tuned for further applications. Firstly, additional chemical species can be inserted between the basal planes to form graphite intercalation compounds (GICs).<sup>95</sup> The interlayer spacing of some GICs can be increased to more than 1 nm (0.34 nm for native graphite), leads to a significant reduction in van der Waals forces

between adjacent layers. Thus it can open a possible route of graphite exfoliation. Secondly, carbon atoms on graphite can be replaced by other elements, which induce substitutional doping of graphite. Thirdly, graphite surface can be functionalized by other chemical group. For instance, carboxyl group can be formed on the surface of graphene structure by plasma oxidation and serves for the attachment of other biologically relevant species.

#### 1.4.3 Methods for synthesizing graphene encapsulated gold nanoparticles

Efforts have been involved in synthesis graphene structures (either carbon nanotubes or graphite shell) on nanoparticles. Among 70 elements that include all of the transition metals, Fe, Co and Ni are elements favored in the catalytic function of graphite formation. It was suggested that carbon atoms cannot stay on gold long enough to produce graphitic network,<sup>96</sup> however, this contradicts with experimental results. Lee et al.<sup>97</sup> used monodispersed gold nanoparticles with diameter less than 2 nm (1.3 – 1.8 nm) synthesized carbon nanotubes, carbon nanofilaments, and carbon nanoparticles encapsulating gold particles by varying growth condition. Single-walled carbon nanotubes were also synthesized by Takagi and co-workers using different kinds of small metal nanoparticles (noble metals such as Au, Ag, Pt, Pd, and iron family metals such as Fe, Co, Ni. Cu was also chosen as catalyst).<sup>98</sup> Here we list several approaches for synthesizing graphene encapsulated gold nanoparticles:

(1) High temperature with electron irradiation. Sutter and co-workers<sup>99</sup> observed the formation of Au/C core-shell heterostructures from amorphous carbon film supported gold nanoparticles. The formation of graphene took place at temperatures higher than 425 °C and under electron beam irradiation. Graphene fragments and layers formed only in the vicinity of gold nanoparticles, away from which amorphous carbon remains, which suggest that gold

nanoparticles were catalysts for the ordering and crystallization of carbon. They also did in situ TEM showing the interaction of nanoparticles under high temperature and electron irradiation (showed in figure 1.5). They found that carbon shells initially inhibit thermally driven coalescence between gold nanoparticles. However, under intense electron irradiation, carbon shells would act like a pressurized chamber and ultimately stimulate coalescence by breaking core/shell structure. This work demonstrated that gold/graphite core/shell heterostructure can be formed and tailored under appropriate thermal and electronic driving force, but this method cannot be scaled up for efficiently synthesizing large amount of core/shell heterostructure.

(2) Polymer coating on gold. Hore and co-workers<sup>100</sup> found that, without addition of amorphous carbon or graphite, carbon layers on gold can form by simply blending aliphatic polymers (e.g. polyethylene) with gold oxide. Comparing X-ray photoelectron spectroscopy (XPS), they demonstrated that cationic gold, after blended with polyethylene or polyvinylidene fluoride, would convert to anionic gold. In this process, polymers were oxidized other than catalyzed into carbon shell on gold particles. Kim et al.<sup>101</sup> also reported the formation of carbon shell from polymer coated gold. Gold film was embedded between two polyamic acid films. This sandwich-shape sample was first annealed at 400-800 °C resulting in a monolayer of gold nanoparticles in the center, then further annealed at 1000 °C in oxidize atmosphere, and eventually formed gold nanoparticles coated with 2-2.5 nm amorphous carbon layer. Overall, synthesis gold/graphite heterostructure by coating polymer would induce a significant amount of amorphous carbon and make it difficult to eliminate impurities after reaction.

(3) Chemical vapor deposition. CVD process is a promising method to produce graphene encapsulated gold with minimum amount of impurities (e.g. CNT), and it is capable to be applied in a large scale. Chopra et al.<sup>102</sup> reported the formation of gold nanoparticle/graphite

heterostructure from plasma oxidized gold by CVD growth. However, there is still a need for detailed understanding of several questions such as the plasma oxidation of gold nanoparticles, the role of gold oxide in the growth of graphene, and the graphene growth mechanism. These are motivations for our research.

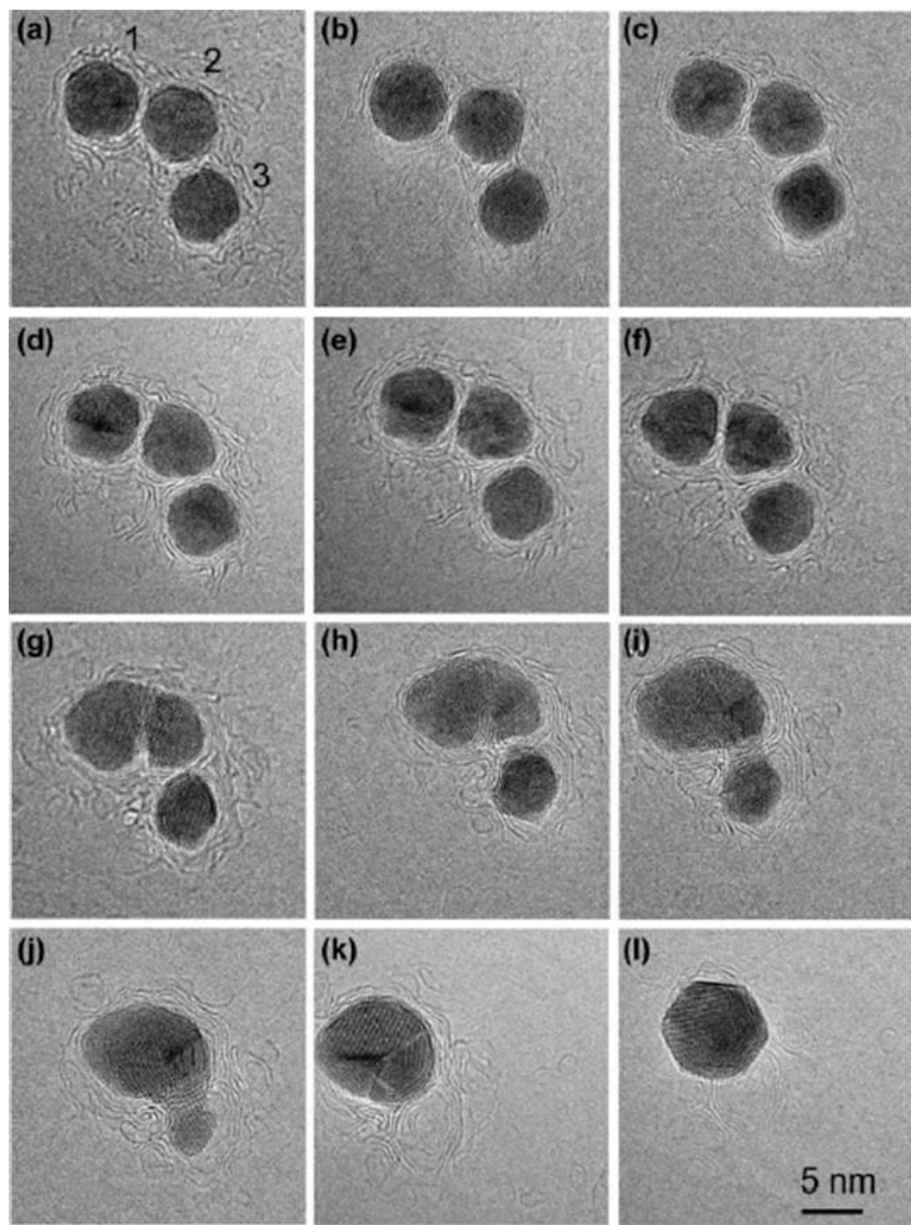


Figure 1.5 Sequence of transmission electron microscopy images characteristic of the interaction of Au/C core-shell nanoparticles in the temperature range between 400 and 800 °C. Reprinted with permission from <sup>99</sup> (Sutter, E.; Sutter, P.; Zhu, Y. M., Assembly and interaction of Au/C core-shell nanostructures: In situ observation in the transmission electron microscope. *Nano Letters* 2005, 5 (10), 2092-2096). Copyright 2005 American Chemical Society.

### *1.5 Raman Spectroscopy*

Raman spectroscopy is an analysis technique which bears the name of India physicist C. V. Raman who was the pioneer in this field. When light interacts with an atom or molecule, different kinds of scattering occur (Rayleigh scattering, Stokes scattering, and Anti-Stokes scattering). If the energy of incident is not high enough to excite the molecules from ground state to the lowest electronic state, the molecule will be excited to a virtual state and immediately go back to the ground state. In case of elastic scattering, molecule will go back to its original energy state, this is called Rayleigh scattering. However, if the light is scattered by an excitation (inelastic scattering), the wavelength of scattered photons will be different from the wavelength of incident phonons, corresponding to energy change. If the emitted energy is lower than the incident energy, it is called Stokes scattering. On the opposite, if the emitted energy is higher, it is called Anti-Stokes scattering. Both kinds of elastic scattering contribute to Raman Effect. Since the energy differences between scattered and incident photons are depend on the differences of the vibrational and rotational energy-levels of the molecule, we can analysis the molecule by comparing the energy shift of photons. Schematic of different cases of scattering is shown in figure 1.6.

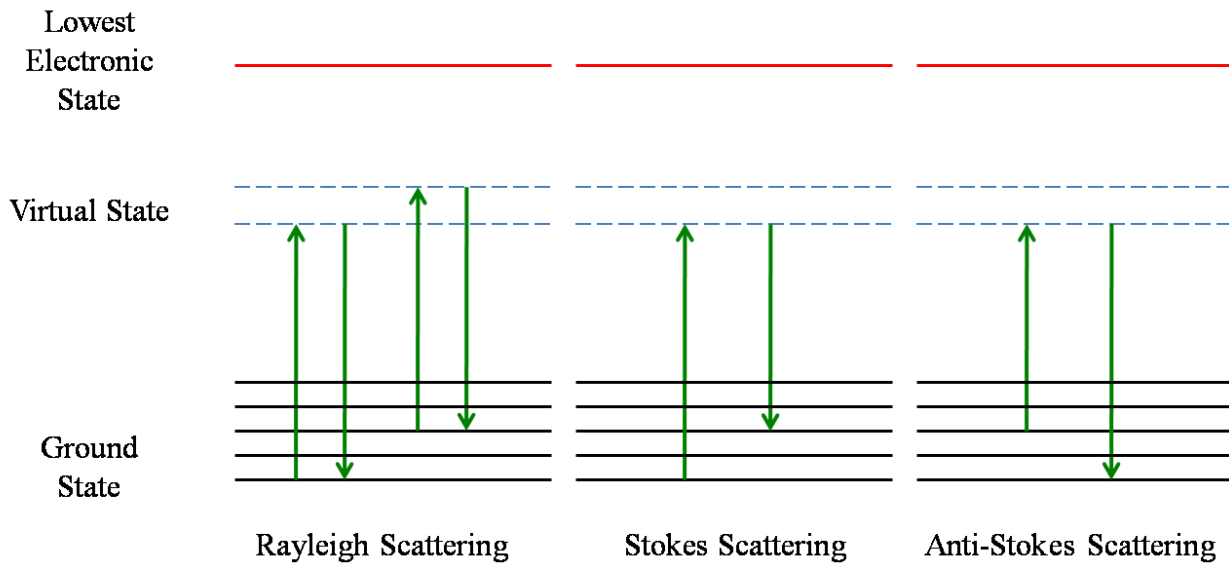


Figure 1.6 Schematic of different cases of scattering (Rayleigh scattering, Stokes scattering, and Anti-Stokes scattering)

### *1.6 Challenges, Motivations, and goals*

Before one can use nanoparticles with desired morphology for further applications, it is necessary to understand how various morphologies develop in nanoparticles and what the major factor is. Even though significant efforts have been made in synthesizing noble metal nanoparticles, it remains unknown that how much variation in their size, shape, and crystallinity exists throughout a specific sample set. Moreover, single component noble metal nanoparticles have several limitations: (1) Aggregation can yield bulk materials or false positive results; (2) Unprotect surface allows the possibility for other chemicals replace the label species on the nanoparticle surface; (3) The properties of noble metal nanoparticles are strongly depend on the type of ligand used to passivate their surfaces. To protect noble metal nanoparticles from unexpected aggregation, we can synthesize graphene encapsulated nanoparticles heterostructure.

The other major challenge is the growth of graphene on noble metal nanoparticles. Usually, Fe, Co, and Ni are used for catalyzing chemical vapor deposition of graphene. For a long time, gold was considered incapable to catalyze the growth of graphene structure. Even though some researchers have successfully synthesized carbon nanotube using gold in CVD furnace,<sup>103, 96, 98</sup> the mechanism is still remains a matter of debate.

Because its plasmon oscillation excitation frequency lies in the range of visible light, gold is a popular material used in SERS. Since graphene has good photo-permeability, gold nanoparticles encapsulated in graphite shell may maintain the property for Raman signal enhancement. Meanwhile, the surface of gold can be protected by carbon shell, on which carboxyl group can be attached, open a new route for the fabrication of multi-functional materials. For other noble metals such as palladium and platinum, they are well known by their catalytic activity. Since nanoparticles' properties are decided by their composition, size, and

shape, it is critical to understand how the morphology factors govern nanoparticles size and shape. At the same time, the synthesis and application of multicomponent nanomaterials is a promising field to explore.

Thus, we believe a systematic study for the morphology control of noble metal nanoparticles synthesis, and the synthesis of graphene encapsulated noble metal nanoparticles can lead us to a new field with multiple application directions for our study.

In this study, our goals include: (1) to understand how different conditions (such as temperature, surfactant type and concentration, reaction duration, foreign ions) affect the morphology development of nanoparticles; (2) to observe the oxidation behavior of gold, palladium, and platinum nanoparticles under oxygen plasma; (3) to synthesis graphene encapsulated noble metal nanoparticles and study the growth mechanism of graphene. These graphene encapsulated noble metal nanoparticles will be a unique surface enhanced Raman substrate, where optical properties of core materials and rich chemistry of graphene shell could result in unique multi-functionality.

## CHAPTER 2

### EXPERIMENTAL PROCEDURES

#### *2.1 Materials and Methods*

Gold (III) chloride trihydrate ( $\text{HAuCl}_4 \cdot 3\text{H}_2\text{O}$ , 99.9%), Palladium (II) chloride ( $\text{PdCl}_2$ , 99.999%), Polyvinylpyrrolidone (PVP,  $(\text{C}_6\text{H}_9\text{NO})_x$ , Mw 40,000) were purchased from Sigma-Aldrich (St. Louis, MO). Sodium tetrachloropalladate (II) hydrate ( $\text{Na}_2\text{PdCl}_4 \cdot x\text{H}_2\text{O}$  ( $x \approx 3$ ), 99.999%), Dihydrogen hexachloropatinate (IV) hexahydrate ( $\text{H}_2\text{PtCl}_6 \cdot 6\text{H}_2\text{O}$ , 99.9%) were bought from Alfa Aesar (Ward Hill, MA). Hexadecyltrimethylammonium bromide (CTAB,  $\text{C}_{19}\text{H}_{42}\text{BrN}$ , 99+ %), sodium borohydride ( $\text{NaBH}_4$ , powder, 98+ %), L-Ascorbic acid (reagent ACS), Silver nitrate ( $\text{AgNO}_3$ , reagent ACS, electrophoresis grade), Ethyl Alcohol ( $\text{C}_2\text{H}_6\text{O}$ , 95%), potassium bromide ( $\text{KBr}$ , 98%) were purchased from Acros Organics (New Jersey, NJ). Acetone ( $(\text{CH}_3)_2\text{CO}$ ), Ethylene Glycol (EG,  $\text{HOCH}_2\text{CH}_2\text{OH}$ ) were bought from VWR International (West Chester, PA), Potassium chloride ( $\text{KCl}$ , 99.7) was purchased from Fisher Scientific (New Jersey, NJ). 3-Mercaptopropyltrimethoxysilane (MPTMS,  $\text{HSCH}_2\text{CH}_2\text{CH}_2\text{Si}(\text{OCH}_3)_3$ , 97+ %) was bought from TCI America (Portland, OR). All chemicals were used without further purification. Silicon wafers (100, n-type) were purchased from IWS (Colfax, CA). DI water (18.1  $\text{M}\Omega\text{-cm}$ ) was obtained using a Barnstead International DI water system (E-pure D4641).

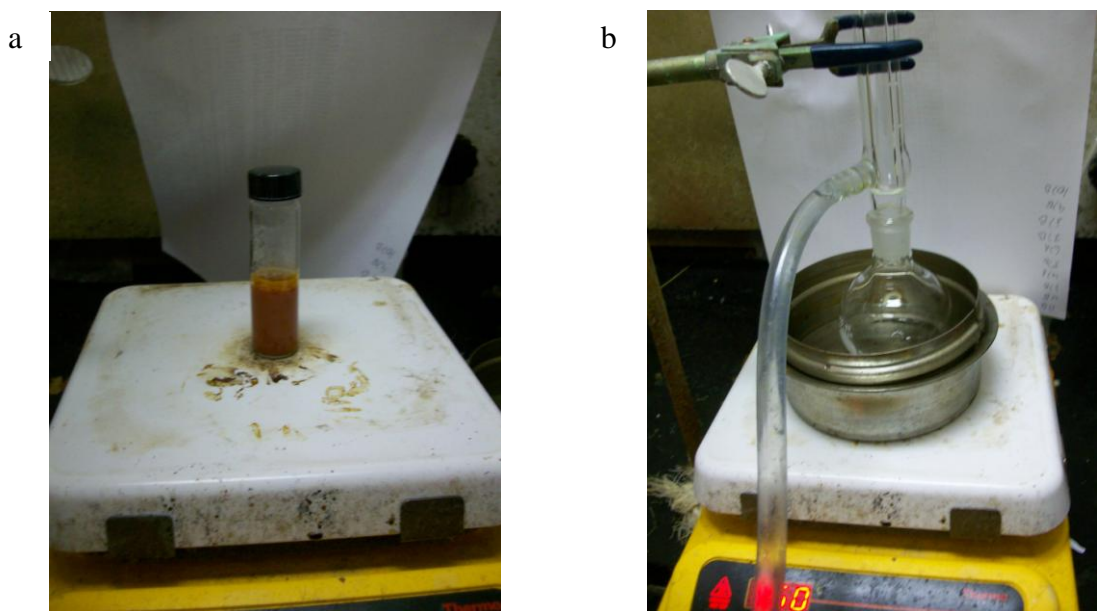
Labnet centrifuge (Edison, NJ) was used to wash and separate nanoparticles. Before characterization, samples were dried and stored in a VWR vacuum oven (West Chester, PA). Oxygen plasma treatment was performed in a Nordson March Jupiter III Reactive Ion Etcher (Concord, CA) and Model 1021 plasma cleaner (E.A. Fischione Instruments, PA). Quenching of solutions was performed in recirculating bath purchased from VWR North American, Model

1162A (West Chester, PA). Graphene growth was conducted inside Lindberg blue 3-zone tube furnace (Watertown, WI). Quartz tubes were purchased from ChemGlass (Vineland, NJ). Syringe injector was obtained from Fisher Scientific (Suwannee, GA). Thermocouples and temperature controllers were bought from Omega Engineering (Stamford, CT). H<sub>2</sub> (UHP grade, 40% balanced with Ar) and Ar (UHP grade) gas cylinders were purchased from Airgas South (Tuscaloosa, AL). Gas flow rates of all chemical vapor deposition processes were controlled by Teledyne Hasting power pod 400 mass flow controllers (Hampton, VA).

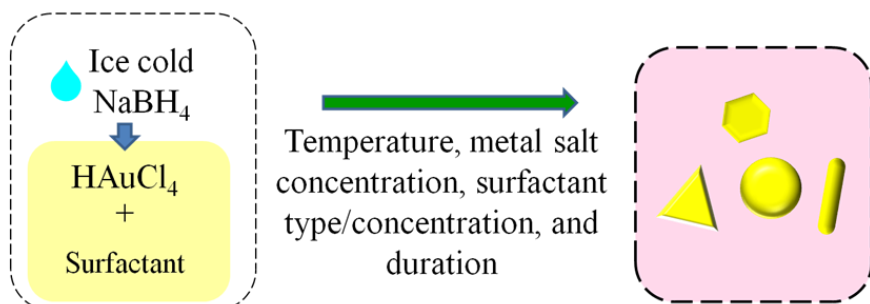
## 2.2 Synthesis of gold nanoparticles

Gold nanoparticles (AuNPs) were synthesized by two methods: single-step method and seed-growth method. For single-step approach baseline sample, 0.1 mL HAuCl<sub>4</sub> ( $5 \times 10^{-3}$  M) was mixed with 9.8 mL CTAB (0.03 M) and 0.1 mL DI water. Subsequently, 10 µL ice-cold NaBH<sub>4</sub> (0.12 M) was added, and solution was magnetically stirred and reacted for 2 h. In seed-growth approach, firstly, seed solution was prepared by mixing 1 mL HAuCl<sub>4</sub> ( $5 \times 10^{-3}$  M) with 50 µL CTAB (0.1 M) and 8.5 mL DI water, then 0.5 mL ice-cold NaBH<sub>4</sub> (0.12 M) was added. The solution was allowed magnetically stirred and reacted for 2 h. After seed synthesis, the baseline sample was synthesized by mixing 0.45 mL HAuCl<sub>4</sub> ( $5 \times 10^{-3}$  M) with 7.5 mL CTAB (0.1 M) and 1.5 mL DI water, then 0.05 mL fresh-made AA (0.1 M) was added while stirring. After that, 0.5 mL as-prepared seed solution was added, and solution was magnetically stirred and reacted for 3 h.

To examine the influence of different growth parameters on the size and morphology of AuNPs, systematic studies (Table 2.1 and 2.4) were performed for both approaches by changing temperature (4 – 130 °C), surfactant type and concentration (0 – 0.8 M), metal salt concentration ( $5 \times 10^{-6}$  –  $5 \times 10^{-3}$  M) or seed amount (0.005 – 0.5 mL), and reaction duration (30 min – 24 h). Only one variable was changed while keeping all the other conditions fixed for each experiment. The effects of quenching (Table 2.2) the AuNP solution immediately after their high temperature synthesis (at 130 °C, Table 2.1, sample 7) were also observed. The AuNP solution was quenched in a recirculating bath for 1 h at 10 °C, 0 °C, and -20 °C, respectively.



c Single-step synthesize of gold nanoparticles



d Seed-growth synthesize of gold nanoparticles

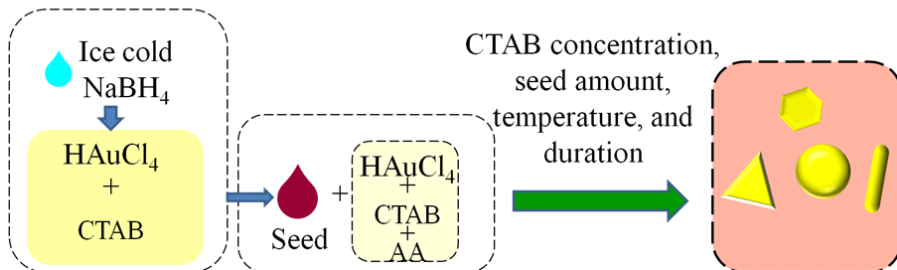


Figure 2.1 Digital image showing the set-up for synthesis gold nanoparticles at (a) room temperature, and (b) high temperature. Schematic showing the parameter study of (c) single-step method and (d) seed-growth method.

Table 2.1 Systematic study for single-step synthesis of AuNPs. The nanoparticles were synthesized by varying one growth parameter at a time while other parameters remained fixed. The shaded region in the table denotes the changing parameter and baseline parameters (sample 2) are indicated by bold and italicized fonts.

Sample number	Surfactant	Surfactant concentration/M	[Au <sup>3+</sup> ]/M	NaBH <sub>4</sub> /M	T/°C	Time/h
1	CTAB	0.0294	5×10 <sup>-5</sup>	1.2×10 <sup>-4</sup>	4	2
2	<b>CTAB</b>	<b>0.0294</b>	<b>5×10<sup>-5</sup></b>	<b>1.2×10<sup>-4</sup></b>	<b>25</b>	<b>2</b>
3	CTAB	0.0294	5×10 <sup>-5</sup>	1.2×10 <sup>-4</sup>	50	2
4	CTAB	0.0294	5×10 <sup>-5</sup>	1.2×10 <sup>-4</sup>	70	2
5	CTAB	0.0294	5×10 <sup>-5</sup>	1.2×10 <sup>-4</sup>	90	2
6	CTAB	0.0294	5×10 <sup>-5</sup>	1.2×10 <sup>-4</sup>	110	2
7	CTAB	0.0294	5×10 <sup>-5</sup>	1.2×10 <sup>-4</sup>	130	2
8	CTAB	0.0294	5×10 <sup>-6</sup>	1.2×10 <sup>-4</sup>	25	2
2	<b>CTAB</b>	<b>0.0294</b>	<b>5×10<sup>-5</sup></b>	<b>1.2×10<sup>-4</sup></b>	<b>25</b>	<b>2</b>
9	CTAB	0.0294	5×10 <sup>-4</sup>	1.2×10 <sup>-4</sup>	25	2
10	CTAB	0.0294	5×10 <sup>-3</sup>	1.2×10 <sup>-4</sup>	25	2
11	PVP	0.0294	5×10 <sup>-5</sup>	1.2×10 <sup>-4</sup>	25	2
2	<b>CTAB</b>	<b>0.0294</b>	<b>5×10<sup>-5</sup></b>	<b>1.2×10<sup>-4</sup></b>	<b>25</b>	<b>2</b>
12	KBr	0.0294	5×10 <sup>-5</sup>	1.2×10 <sup>-4</sup>	25	2
13	MPTMS	0.0294	5×10 <sup>-5</sup>	1.2×10 <sup>-4</sup>	25	2
14	PVA	0.0294	5×10 <sup>-5</sup>	1.2×10 <sup>-4</sup>	25	2
15	CTAB	0	5×10 <sup>-5</sup>	1.2×10 <sup>-4</sup>	25	2
16	CTAB	0.0074	5×10 <sup>-5</sup>	1.2×10 <sup>-4</sup>	25	2
2	<b>CTAB</b>	<b>0.0294</b>	<b>5×10<sup>-5</sup></b>	<b>1.2×10<sup>-4</sup></b>	<b>25</b>	<b>2</b>
17	CTAB	0.8	5×10 <sup>-5</sup>	1.2×10 <sup>-4</sup>	25	2
18	CTAB	0.0294	5×10 <sup>-5</sup>	1.2×10 <sup>-4</sup>	25	0.25
19	CTAB	0.0294	5×10 <sup>-5</sup>	1.2×10 <sup>-4</sup>	25	0.5
2	<b>CTAB</b>	<b>0.0294</b>	<b>5×10<sup>-5</sup></b>	<b>1.2×10<sup>-4</sup></b>	<b>25</b>	<b>2</b>
20	CTAB	0.0294	5×10 <sup>-5</sup>	1.2×10 <sup>-4</sup>	25	24

Table 2.2 Quenching conditions for AuNPs that were synthesized at 130 °C (Table 2.1, sample 7)

Sample number	Surfactant	Surfactant concentration/M	[Au <sup>3+</sup> ]/M	NaBH <sub>4</sub> /M	Synthesis T/°C	Synthesis Time/h	Quench T/°C	Quench time/h
21	CTAB	0.0294	5×10 <sup>-5</sup>	1.2×10 <sup>-4</sup>	130	2	10	1
22	CTAB	0.0294	5×10 <sup>-5</sup>	1.2×10 <sup>-4</sup>	130	2	0	1
23	CTAB	0.0294	5×10 <sup>-5</sup>	1.2×10 <sup>-4</sup>	130	2	-20	1

Table 2.3 Seed synthesis condition in seed-growth method.

Surfactant	Surfactant concentration/M	[Au <sup>3+</sup> ]/M	NaBH <sub>4</sub> /M	T/°C	Time/h
CTAB	0.0005	5×10 <sup>-4</sup>	0.006	25	2

Table 2.4 Systematic study for growth condition of seed-growth synthesis of AuNPs. The nanoparticles were synthesized by varying one growth parameter at a time while other parameters remained fixed. The shaded region in the table denotes the changing parameter and baseline parameters (sample 2) are indicated by bold and italicized fonts.

Sample number	[Au <sup>3+</sup> ]/M	Surfactant	Surfactant concentration/M	Seed amount/mL	T/°C	Time/h
1	2.25×10 <sup>-4</sup>	CTAB	0	0.5	25	3
2	<b>2.25×10<sup>-4</sup></b>	<b>CTAB</b>	<b>0.075</b>	<b>0.5</b>	<b>25</b>	<b>3</b>
3	2.25×10 <sup>-4</sup>	CTAB	0.5	0.5	25	3
4	2.25×10 <sup>-4</sup>	CTAB	0.075	0.0005	25	3
5	2.25×10 <sup>-4</sup>	CTAB	0.075	0.0625	25	3
6	2.25×10 <sup>-4</sup>	CTAB	0.075	0.125	25	3
2	<b>2.25×10<sup>-4</sup></b>	<b>CTAB</b>	<b>0.075</b>	<b>0.5</b>	<b>25</b>	<b>3</b>
2	<b>2.25×10<sup>-4</sup></b>	<b>CTAB</b>	<b>0.075</b>	<b>0.5</b>	<b>25</b>	<b>3</b>
7	2.25×10 <sup>-4</sup>	CTAB	0.075	0.5	90	3
8	2.25×10 <sup>-4</sup>	CTAB	0.075	0.5	130	3
9	2.25×10 <sup>-4</sup>	CTAB	0.075	0.5	25	1
2	<b>2.25×10<sup>-4</sup></b>	<b>CTAB</b>	<b>0.075</b>	<b>0.5</b>	<b>25</b>	<b>3</b>
10	2.25×10 <sup>-4</sup>	CTAB	0.075	0.5	25	9
11	2.25×10 <sup>-4</sup>	CTAB	0.075	0.5	25	24

### *2.3 Plasma oxidation of gold nanoparticles*

As-synthesized AuNPs were oxidized by plasma treatment process. Silicon wafer was first piranha cleaned by soaked in the mixture of H<sub>2</sub>SO<sub>4</sub> and H<sub>2</sub>O<sub>2</sub> (volume ratio is 5:1) at 100 °C for 30 min. Subsequently, the wafer was soaked and rinsed with copious amount of DI water and dried in air. As a next step, as-prepared AuNPs (table 1, sample 10) were dispersed on piranha cleaned silicon substrate by drop casting. After this step, the silicon substrate decorated with AuNPs was dried in desiccator. Subsequently, the substrate was placed in Jupiter III reactive ion etching chamber and oxidized at 160 watt and 300 mTorr of O<sub>2</sub> pressure. To study the effect of plasma oxidation on AuNPs, the process was performed for different durations (15-75 min).

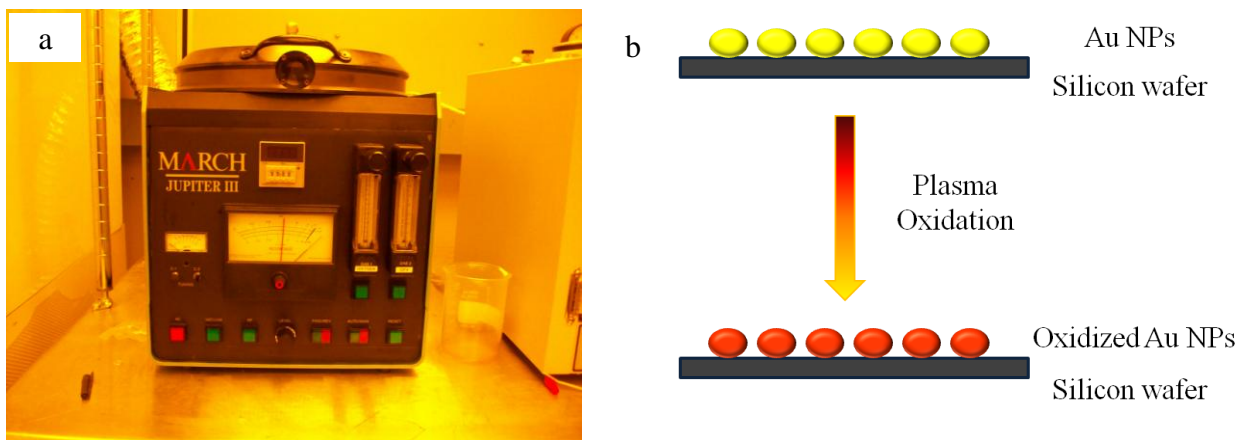


Figure 2.2 (a) Digital image showing Jupiter III reactive ion etcher, (b) schematic indicating gold nanoparticles are oxidized by O<sub>2</sub> plasma.

#### *2.4 Growth of graphene on gold nanoparticles*

Graphene was grown in a CVD process. Silicon wafer decorated with AuNPs that were plasma oxidized for 30 min was placed in the center of quartz tube equipped with precursor and gas lines for Ar/H<sub>2</sub> flow. Xylene precursor was injected through a syringe injector into a pre-heated zone (~ 220 °C) at the rate of 45 mL/h for about 2 min and subsequently transported into the reaction zone (~ 675 °C) inside the quartz tubes furnace. The xylene flow rate was reduced to 1 mL/h when H<sub>2</sub> in Ar (Ar/H<sub>2</sub>=1.8 SLM: 0.2 SLM 10% v/v) carrier gas was introduced in the CVD reactor, where H<sub>2</sub> acted as an oxygen scavenger. The CVD reaction was continued for 1 h after which H<sub>2</sub> and xylene flow was discontinued and furnace was cooled down under Ar flow.

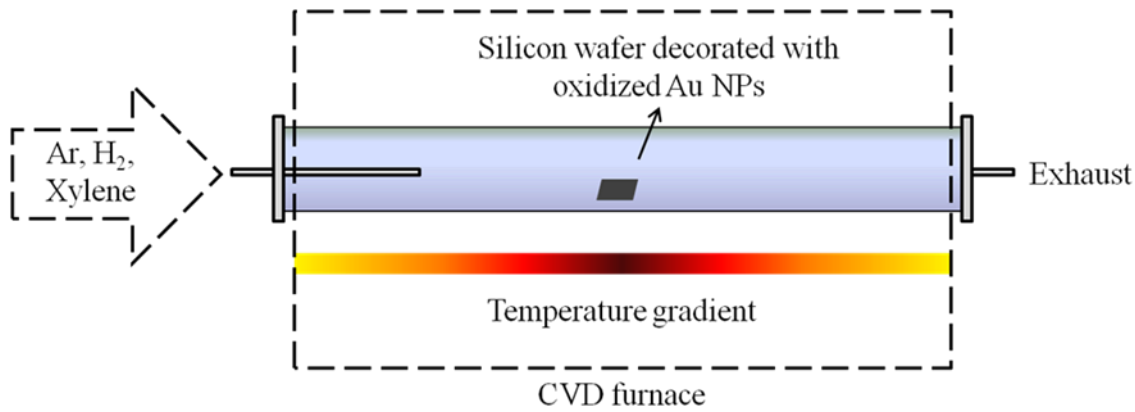


Figure 2.3 Schematic representing of chemical vapor deposition process for graphene encapsulating noble metal nanoparticles

## *2.5 Synthesis of palladium nanoparticles*

Palladium nanoparticles (PdNPs) were synthesized by ethanol reduction for parameter study. In a typical process, 4.8 mg PdCl<sub>2</sub> was dissolved in a mixture of 10 mL ethanol and 10 mL DI water. 0.116 g PVP was added to the solution, and then the solution was allowed to reflux at 100 °C for 3 h in N<sub>2</sub> atmosphere. The dark brown product was washed by DI water and Acetone, and finally dispersed in DI water. To examine the influence of different parameters on the size and morphology of Pd nanoparticles, systematic studies (Table 2.5) were performed by changing surfactant concentration (0.261 – 2 mM), metal salt concentration (0.0271 – 0.5 mM), temperature (100 – 150 °C), and reaction duration (1 – 10 h). Only one variable was changed while keeping all the other experimental conditions fixed for each particular experiment.

To control the shape of PdNPs, KBr and KCl were added as shape-control additives. An aqueous solution (8.0 mL) containing 105 mg PVP, 60 mg AA, 600 mg KBr, and 185 mg KCl were placed in a volumetric flask, refluxed and pre-heated in oil bath under magnetic stirring at 80 °C for 10 min. Then, 3.0 mL of an aqueous solution containing 67.46 mg Na<sub>2</sub>PdCl<sub>4</sub>·xH<sub>2</sub>O (x≈3) was added using a pipette. The solution was stirred and refluxed at 80 °C for 3 h. The dark brown solution was centrifuged, washed 3 times to remove excess PVP, and re-dispersed in 11 mL DI water.

Table 2.5 Systematic study for synthesis of PdNPs. The nanoparticles were synthesized by varying one growth parameter at a time while other parameters remained fixed. The shaded region in the table denotes the varying parameter and baseline parameters (sample 3) are indicated by bold and italicized fonts.

Sample number	Metal salt	Reducing agent	PVP amount/mmol	Metal salt/mmol	T/°C	Time/h	KBr/mmol	KCl/mmol
1	PdCl <sub>2</sub>	Ethanol	0.261	0.0271	100	3	0	0
2	PdCl <sub>2</sub>	Ethanol	0.522	0.0271	100	3	0	0
<b>3</b>	<b>PdCl<sub>2</sub></b>	<b>Ethanol</b>	<b>1.044</b>	<b>0.0271</b>	<b>100</b>	<b>3</b>	<b>0</b>	<b>0</b>
4	PdCl <sub>2</sub>	Ethanol	2	0.0271	100	3	0	0
<b>3</b>	<b>PdCl<sub>2</sub></b>	<b>Ethanol</b>	<b>1.044</b>	<b>0.0271</b>	<b>100</b>	<b>3</b>	<b>0</b>	<b>0</b>
5	PdCl <sub>2</sub>	Ethanol	1.044	0.05	100	3	0	0
6	PdCl <sub>2</sub>	Ethanol	1.044	0.25	100	3	0	0
7	PdCl <sub>2</sub>	Ethanol	1.044	0.5	100	3	0	0
<b>3</b>	<b>PdCl<sub>2</sub></b>	<b>Ethanol</b>	<b>1.044</b>	<b>0.0271</b>	<b>100</b>	<b>3</b>	<b>0</b>	<b>0</b>
8	PdCl <sub>2</sub>	Ethanol	1.044	0.0271	125	3	0	0
9	PdCl <sub>2</sub>	Ethanol	1.044	0.0271	150	3	0	0
10	PdCl <sub>2</sub>	Ethanol	1.044	0.0271	100	1	0	0
<b>3</b>	<b>PdCl<sub>2</sub></b>	<b>Ethanol</b>	<b>1.044</b>	<b>0.0271</b>	<b>100</b>	<b>3</b>	<b>0</b>	<b>0</b>
11	PdCl <sub>2</sub>	Ethanol	1.044	0.0271	100	6	0	0
12	PdCl <sub>2</sub>	Ethanol	1.044	0.0271	100	10	0	0
13	NaPdCl <sub>4</sub>	AA	0.945	0.1937	80	3	5.04	2.48

## *2.6 Synthesis of platinum nanoparticles*

Platinum nanoparticles (PtNPs) were synthesized by alcohol reduction for parameter study. In a typical process, 6.2 mg H<sub>2</sub>PtCl<sub>6</sub>·6H<sub>2</sub>O was dissolved in 2 mL DI water, mixed with 8 mL DI water and 10 mL ethanol, followed with adding 0.04 g PVP. The mixture was refluxed at 95 °C for 3 h under air. To examine the influence of different parameters on the size and morphology of PtNPs, parametric studies (Table 2.6) were performed by changing metal salt concentration ( $1.93 \times 10^{-5}$  -  $1.93 \times 10^{-2}$  M), surfactant amount (0 – 2 g), temperature (95 – 150 °C), reducing agent (ethanol or NaBH<sub>4</sub>), and duration (1 – 24 h). Only one variable was changed while keeping all the other conditions fixed for each experiment.

To control the shape of PtNPs, AgNO<sub>3</sub> was added as shape-control additive. First, 2.5 mL of EG was magnetic stirred and refluxed at 200 °C for 5 min in an oil heating bath. Second, 0.5 mL 0.002 M AgNO<sub>3</sub> in EG was added to above EG. Third, 3 mL 0.375 M PVP and 1.5 mL 0.0625 M H<sub>2</sub>PtCl<sub>6</sub> in EG were mixed together, then 140.7 µL of PVP and H<sub>2</sub>PtCl<sub>6</sub> in EG mixture was added into the volumetric flask every 30 s over a 16 min period (4.5 mL totally). The resultant mixture was heated and refluxed at 200 °C for an additional 5 min. After cooling down, the solution was centrifuged at 5000 rpm for 15 min to remove AgCl. The supernatant was collected and precipitated by adding triple volume (21 mL) of acetone, and centrifuged at 3000 rpm for 5 min. The precipitate was dispersed in 3 mL ethanol by sonication, then added 9 mL of hexane. Repeating the centrifugation step twice, and finally the product was dispersed in 3 mL of ethanol.

Table 2.6 Systematic study for synthesis of PtNPs. The nanoparticles were synthesized by varying one growth parameter at a time while other parameters remained fixed. The shaded region in the table denotes the changing parameter and baseline parameters (sample 2) are indicated by bold and italicized fonts.

Sample number	H <sub>2</sub> PtCl <sub>6</sub> /M	Surfactant (PVP) amount/g	T/°C	Reducing agent	Time/h	Additive
1	1.93×10 <sup>-5</sup>	0.04	95	Ethanol	3	/
<b>2</b>	<b>6.0×10<sup>-4</sup></b>	<b>0.04</b>	<b>95</b>	<b>Ethanol</b>	<b>3</b>	<b>/</b>
3	1.93×10 <sup>-3</sup>	0.04	95	Ethanol	3	/
4	1.93×10 <sup>-2</sup>	0.04	95	Ethanol	3	/
5	6.0×10 <sup>-4</sup>	0	95	Ethanol	3	/
<b>2</b>	<b>6.0×10<sup>-4</sup></b>	<b>0.04</b>	<b>95</b>	<b>Ethanol</b>	<b>3</b>	<b>/</b>
6	6.0×10 <sup>-4</sup>	1.2	95	Ethanol	3	/
7	6.0×10 <sup>-4</sup>	2	95	Ethanol	3	/
<b>2</b>	<b>6.0×10<sup>-4</sup></b>	<b>0.04</b>	<b>95</b>	<b>Ethanol</b>	<b>3</b>	<b>/</b>
8	6.0×10 <sup>-4</sup>	0.04	150	Ethanol	3	/
<b>2</b>	<b>6.0×10<sup>-4</sup></b>	<b>0.04</b>	<b>95</b>	<b>Ethanol</b>	<b>3</b>	<b>/</b>
9	6.0×10 <sup>-4</sup>	0.04	95	NaBH <sub>4</sub>	3	/
10	6.0×10 <sup>-4</sup>	0.04	95	Ethanol	1	/
<b>2</b>	<b>6.0×10<sup>-4</sup></b>	<b>0.04</b>	<b>95</b>	<b>Ethanol</b>	<b>3</b>	<b>/</b>
11	6.0×10 <sup>-4</sup>	0.04	95	Ethanol	10	/
12	6.0×10 <sup>-4</sup>	0.04	95	Ethanol	24	/
13	1.25×10 <sup>-2</sup>	0.125	200	Ethylene glycol	0.35	AgNO <sub>3</sub>

## *2.7 Dispersion and plasma oxidation of palladium, platinum nanoparticles*

As-synthesized shape controlled PdNPs and PtNPs were oxidized by plasma treatment process. PdNPs and PtNPs were dispersed on piranha cleaned silicon substrate as the same method with AuNPs by drop casting. After this step, the silicon substrate decorated with gold nanoparticles was dried in desiccator. The plasma oxidation process for PdNPs and PtNPs was performed in Model 1021 plasma cleaner at 600 W and ~36 mTorr of mixture gas (25% O<sub>2</sub> and 75% Ar) pressure. To study the effect of plasma oxidation on PdNPs and PtNPs, the process was performed for different durations (5-45 min).

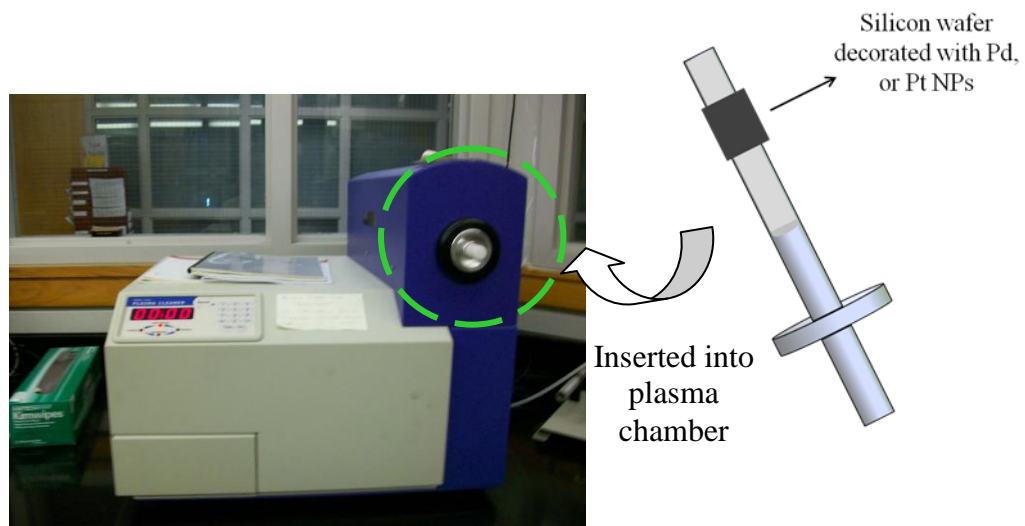


Figure 2.4 Digital images of Model 1021 plasma cleaner and the schematic shows sample stage.

## *2.8 Growth of graphene on palladium and platinum nanoparticles*

Graphene was grown in a CVD process as the same method with gold nanoparticles. Silicon wafer decorated with PdNPs, PtNPs that were plasma oxidized for 30 min were placed in the center of quartz tube equipped with precursor and gas lines for Ar/H<sub>2</sub> flow. Xylene precursor was injected through a syringe injector into a pre-heated zone (~ 220 °C) at the rate of 45 mL/h for about 2 min and subsequently transported into the reaction zone (~ 675 °C) inside the quartz tubes furnace. The xylene flow rate was reduced to 10 mL/h when H<sub>2</sub> in Ar (Ar/H<sub>2</sub>=1.8 SLM: 0.2 SLM, 10% v/v) carrier gas was introduced in the CVD reactor, where H<sub>2</sub> acted as an oxygen scavenger. The CVD reaction was continued for 1 h after which H<sub>2</sub> and xylene flow was discontinued and furnace was cooled down under Ar flow.

## *2.9 Characterization*

Scanning Electron Microscopy (SEM) images were obtained using FE-SEM JEOL-7000 at 20 kV. Tecnai F-20 was used to collect Transmission Electron Microscopy (TEM) images at 200 kV. SEM and TEM are used to characterize samples' morphology. TEM samples were obtained by dispersing as-prepared samples on lacey carbon TEM copper grids purchased from Ted Pella Inc. (Redding, CA). X-ray photoelectron spectra (XPS) were gathered by Kratos Axis 165 with Aluminum mono-gun. The analysis spot was set as "Slot" with >20  $\mu\text{m}$  aperture and 19.05 mm iris setting. XPS was used to characterize elements' chemical states. Raman data were acquired using a Bruker Senterra Raman microscope (Bruker Optics Inc. Woodlands, TX) with 785nm excitation, a 1200 rulings/mm holographic grating and a CCD detector, with the power at the sample ranging from 10 to 100 mW. Raman spectroscopy was used to characterize quality of graphene shells.



Figure 2.5 Digital images of (a) FE-SEM JEOL-7000 for SEM, (b) Tecnai F-20 for TEM, (c) Kratos Axis for XPS, and (d) Bruker Senterra for Raman.

## **2.10 Raman mapping for noble metal nanoparticles after graphene growth**

Raman spectral measurements were performed on silicon wafer decorated with AuNPs (table 2.1, sample 10), PdNPs (table 2.5, sample 13), and PtNPs (table 2.6, sample 12) after graphene growth. The spectral resolution is 3~5 cm<sup>-1</sup> in the range of 102-2658 cm<sup>-1</sup> with a laser power of 10 mW. A rectangular grid with area equal to 15μm× 15μm of the sample surface was chosen, the number of grid positions of both the X and Y directions is 10, and totally 100 points on the grid were scanned in full range. The chemical mapping was calculated by integrate the G-band peak area with a define range from 1500~1700 cm<sup>-1</sup>. 3-D map was plotted versus the sample video image, where X, Z axis shows the sample position and Y axis shows the normalized intensity of G-band peak (normalized by the highest G-band peak intensity in scanned area).

## **2.11 Disperse noble metal nanoparticles on silicon wafer**

As-prepared AuNPs, PdNPs, and PtNPs were dispersed on silicon wafer by drop-casting and MPTMS functionalization methods. In both methods, silicon wafers were first piranha cleaned by the method described before. Drop-casting method is dropping appropriate amount of solution containing as-prepared nanoparticles on clean silicon wafer, and then dry in air.

It is well known that thiol group in MPTMS has strong binding to metals such as gold, palladium, and platinum.<sup>51</sup> So, MPTMS functionalization method first self-assembled a layer of MPTMS on hydroxyl-terminated silicon wafer through –OCH<sub>3</sub> group<sup>104</sup> by immersing piranha cleaned silicon wafer in 2 mM MPTMS in reagent alcohol for 12 h. Then the functionalized silicon wafer was rinsed with reagent alcohol, and annealed at 80 °C in air for 1 h to obtain strong binding between MPTMS and silicon wafer. After annealing, functionalized silicon wafers are ready to be used as substrate to disperse noble metal nanoparticles. The functionalized substrate will be immersed in nanoparticle solution for 12 h, and rinsed with reagent alcohol after dispersion.

## *2.12 Raman analysis of methylene blue on noble metal nanoparticles*

AuNPs, PdNPs, and PtNPs were first MPTMS functionalized on three silicon wafers, respectively. The substrates decorated with noble metal nanoparticles then can be used for surface enhanced Raman spectroscopy. Methylene blue ( $20 \mu\text{L}$ ,  $10^{-5} \text{ M}$ ) was drop-cast on piranha cleaned silicon wafer and three silicon wafer MPTMS functionalized AuNPs, PdNPs, and PtNPs, respectively. Raman spectral measurements were performed on above four silicon wafers after methylene blue dried in air. The spectral resolution was  $3\sim5 \text{ cm}^{-1}$  in the range of  $102\text{-}2658 \text{ cm}^{-1}$  with a laser power of  $10 \text{ mW}$ .

## CHAPTER 3

### RESULT AND DISCUSSION

#### *3.1 Synthesis and characterization of gold nanoparticles*

Gold is face centered cubic crystal; the lattice vectors are orthogonal and of equal length (denoted as lattice constant  $a$ ). Equation 3.1 describes the relationship between adjacent ( $lmn$ ) lattice planes and lattice constant.

$$d_{(lmn)} = \frac{a}{\sqrt{l^2+m^2+n^2}} \quad (3.1)$$

Where  $d_{(lmn)}$  is the lattice spacing which can be measured from high-resolution TEM,  $a$  is lattice constant, and  $l, m, n$  are Miller indices.

The nucleation of gold nanoparticles is the result of competition between two opposing factors: the decrease of free energy because of the creation of new volume, and the increase of free energy because of the creation of new surface.<sup>105</sup> In order to explain our observations in parameter study of gold nanoparticles nucleation and growth, some fundamental thermodynamic equations can be applied:

$$\Delta G_v = -\frac{kT}{\Omega} \ln \left( \frac{C}{C_o} \right) = -\frac{kT}{\Omega} \ln (1 + \sigma) \quad (3.2)$$

$$\Delta G = \frac{4}{3}\pi r^3 \Delta G_v + 4\pi r^2 \gamma \quad (3.3)$$

$$r^* = -2 \frac{\gamma}{\Delta G_v} \quad (3.4)$$

$$\Delta G^* = \frac{16\pi\gamma^3}{3(\Delta G_v)^2} \quad (3.5)$$

$$P = \exp \left( -\frac{\Delta G^*}{kT} \right) \quad (3.6)$$

$$\Gamma = \frac{kT}{3\pi\lambda^3\eta} \quad (3.7)$$

$$R_N = nP\Gamma = \left\{ \frac{c_0' kT}{3\pi\lambda^3\eta} \right\} \exp\left(-\frac{\Delta G^*}{kT}\right) \quad (3.8)$$

$$J = -D \frac{\partial C}{\partial x} \quad (3.9)$$

$$D = \frac{kT}{3\pi\eta\lambda} \quad (3.10)$$

Where  $\Delta G_v$  is the decrease in Gibbs free energy per unit volume of solid phase,  $k$  is Boltzmann constant,  $T$  is the temperature;  $\Omega$  is the atomic volume,  $\sigma$  is the supersaturation,  $C$  and  $C_0$  are concentration and equilibrium concentration, respectively;  $\gamma$  is surface energy;  $r^*$  is critical size for nucleus,  $\Delta G^*$  is critical free energy for nucleation;  $P$  is nucleation probability;  $\Gamma$  and  $\lambda$  are the successful jump frequency and diameter of growth species, respectively;  $\eta$  is the viscosity of the solution.  $R_N$  is the rate of nucleation per unit volume;  $n$  is the number of growth species per unit volume, which equals to the initial concentration  $c_0'$ .  $J$  is diffusion flux,  $D$  is diffusion coefficient, and  $x$  is position.

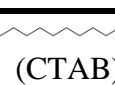
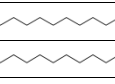
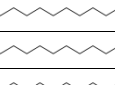
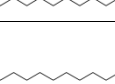
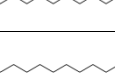
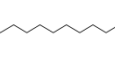
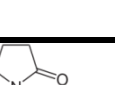
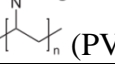
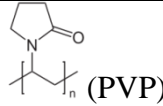
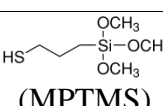
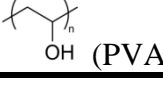
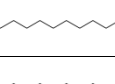
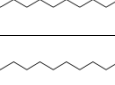
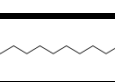
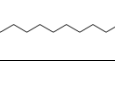
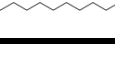
### 3.1.1 Synthesis gold nanoparticles in single-step

Gold nanoparticles were first prepared by single-step synthesis method with conditions listed in table 2.1 in experimental part. The gold nanoparticles synthesized at 130 °C were quenched immediately after synthesis with conditions listed in table 2.2. After synthesis, the morphologies and lattice fringes were observed for as-prepared gold nanoparticles through TEM, and results are summarized in table 3.1 and 3.2.

In single-step synthesis, gold nanoparticles developed through the reduction of ionic gold to metallic gold by NaBH<sub>4</sub>. Nucleation is homogeneous because of the absence of foreign nucleus. So, the shape of a gold nanoparticle under thermodynamic equilibrium condition can be predicted by Gibbs-Wulff theorem. When the surface energy is isotropic, the equilibrium shape

for a particle would be spherical to obtain minimum surface area for a given volume. However, the surface energy for crystalline solids is anisotropic. For instance, gold is face centered cubic (fcc) crystal structure, and the surface energies of low-index crystallographic facets is given in the order  $\gamma\{111\} < \gamma\{100\} < \gamma\{110\}$ .<sup>14</sup> Therefore, minimum total surface energy will be obtained from the balance of the surface area and the nature of the surface facets, both {111} and {100} facets would be contributed to the surface. This is further proved by TEM results, (111) and (200) crystal planes were observed in our system, which correspond to {111} and {100} facets, respectively. The crystal plane of nanoparticles can be calculated from lattice spacing under high-resolution TEM images by equation 3.1.

Table 3.1 Result summary for systematic study indicating size, shape distribution, lattice spacing, and the corresponding planes for the as-prepared AuNPs according to the table 2.1

Sample number	Surfactant structure	Average size (nm)	Shape distribution	Lattice spacing (nm) and the corresponding plane
1	 (CTAB)	5.71±1.71	Spherical	0.2062±0.003, (200)
2		4.67±1.53	Spherical	0.2152, (200)
3		4.59±1.46	Spherical	0.2217, (111)
4		5.28±0.90	Spherical	0.2077, (200)
5		7.48±2.9	Spherical	0.2332, (111)
6		7.10±3.06	Spherical	0.2031±0.001, (200)
7		13.98±3.9	Triangle: 10%; Cubic: 9.2%; Spherical: 80.8%.	0.2062, (200) 0.2379, (111)
8		5.92±1.59	Spherical	0.2111, (200)
9		9.42±3.11	Spherical	0.2099±0.002, (200) 0.2212, (111)
10		23.28±13.41	Hexagon: 1.4%; Rhombus: 10.4%; Square: 8.1%; Triangle: 2.5% Spherical: 65%.	0.2119±0.027, (200) 0.2322±0.002, (111) 0.2677, (110)
11	 (PVP)	2.98±1.66	Spherical	0.2103±0.0004, (200) 0.1842, (210)
12	KBr	14.93±5.41	Spherical	0.1973±0.003, (200) 0.2321±0.003, (111)
13	 (MPTMS)	5.73±1.92	Spherical	0.2010, (200) 0.2432, (111)
14	 (PVA)	3.25±0.42	Spherical	0.1964±0.002, (200)
15		4.71±0.97	Spherical	0.2361±0.004, (111)
16		4.27±1.74	Spherical	0.2270, (111)
17		3.42±0.72	Spherical	0.2118, (200)
18		3.64 ± 1.56	Spherical	0.2073, (200)
19		4.80 ± 1.60	Spherical	0.2032, (200)
20		4.35 ± 3.25	Spherical	0.2358, (111)

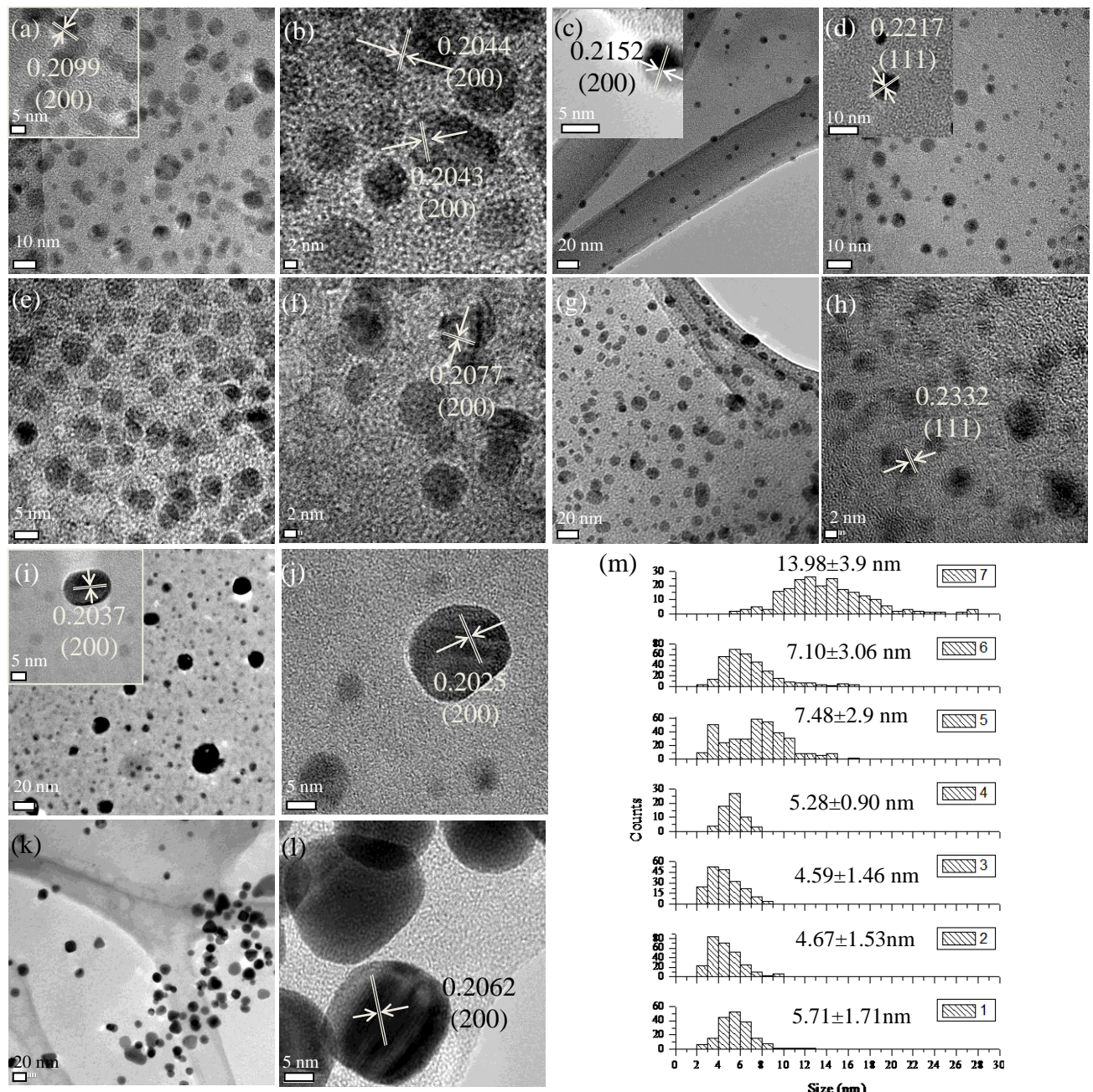
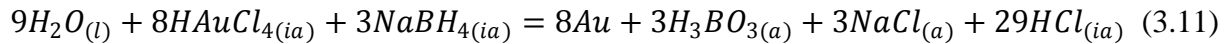


Figure 3.1 TEM images of AuNPs (table 2.1, sample 1-7) synthesized at different temperatures:  
 (a, b) 4 °C, (c) 25 °C, (d) 50 °C, (e, f) 70 °C, (g, h) 90 °C, (i, j) 110 °C, (k, l) 130 °C, and (m)  
 histogram showing AuNPs size distributions.

*Temperature effect:* The reduction of HAuCl<sub>4</sub> by NaBH<sub>4</sub> is shown in equation 3.11:



The Gibbs free energy for reaction ( $\Delta_r G$ ) at certain temperature can be calculated by software HSC 5.1, which is plotted out in figure 3.2. At temperature range from 4 °C to 130 °C,  $\Delta_r G$  keeps large negative quantity, indicates that such a reaction will be favored. Meanwhile, the absolute value of  $\Delta_r G$  decrease as the increase of temperature, because the reaction occurs with an evolution of heat (exothermic process). As been proved by this thermodynamic calculation for reaction Gibbs free energy ( $\Delta_r G$ ), HAuCl<sub>4</sub> can be easily reduced by strong reducing agent NaBH<sub>4</sub> in the temperature range we studied, so the size and shape of gold nanoparticles are decided by nucleation and growth processes.

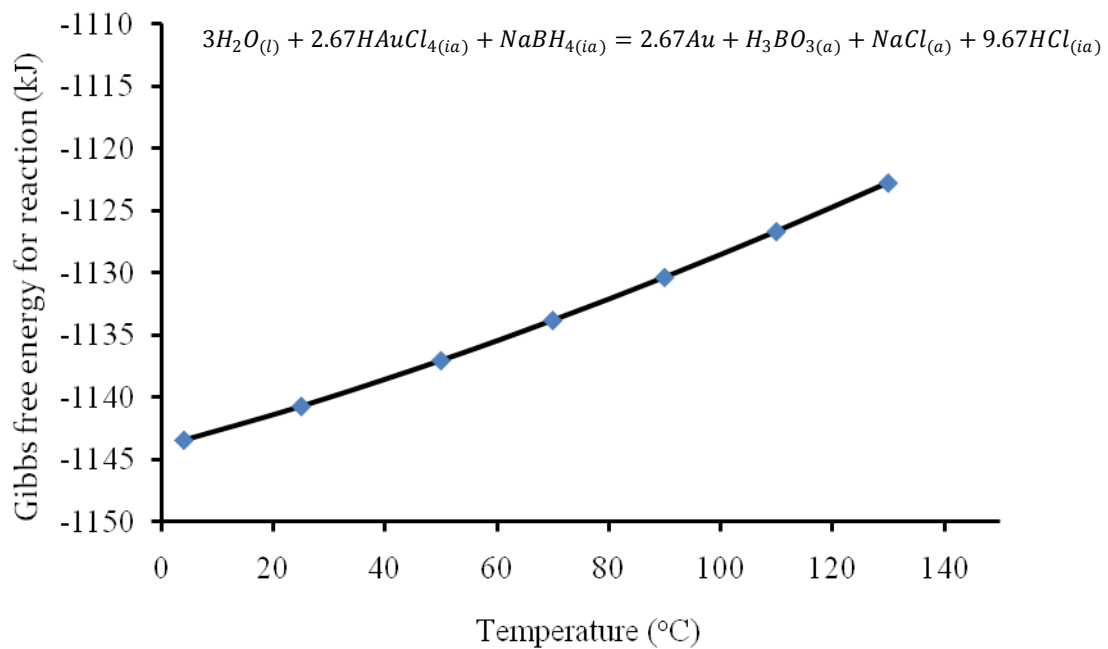


Figure 3.2 Reaction Gibbs free energy ( $\Delta_r G$ ) of reduction reaction of HAuCl<sub>4</sub> with NaBH<sub>4</sub> at different temperature.

According to equations 3.3 and 3.4, the minimum size of a new nucleus can exist ( $r^*$ ) is dominated by the energy barrier ( $\Delta G^*$ ) which is direct proportional to third order of surface energy ( $\gamma$ ) and inverse proportional to second order of volume Gibbs free energy ( $\Delta G_v$ ). Increasing  $\gamma$  or decreasing the absolute value of  $\Delta G_v$  results in the increase of  $\Delta G^*$  for nucleation and critical size for nucleus  $r^*$ . For a giving system,  $\Delta G_v$  varies with temperature ( $T$ ) and supersaturation ( $\sigma$ ), as shown in equation 3.2. Since  $\sigma$  dominates the change of  $\Delta G_v$ , and  $\sigma$  decreased as temperature increased, when temperature increased from 4 °C to 130 °C,  $\Delta G_v$  decreased, thus leading to the increase of  $\Delta G^*$  and  $r^*$ .

Also, at different temperature, the diffusion coefficient for gold ions diffused on gold nanoparticles can be derived from Stokes-Einstein equation (equation 3.10). For two gold nanoparticles with the same diameter, we have:

$$\frac{D_1}{D_2} = \frac{T_1}{T_2} \cdot \frac{\eta_2}{\eta_1} \quad (3.12)$$

If assuming that the viscosity of solution does not change, the change of diffusion coefficient from 4 °C to 130 °C would be:  $D_{277K}:D_{403K} = 277:403 \approx 1:1.5$ . In fact, the viscosity of solution will decrease as temperature increase, so the diffusion coefficient will increase more. According to Fick's law (equation 3.9), flux of gold ions to the surface of gold increases, thus gold nanoparticles have higher growth rate at higher temperature.

As the temperature increased closer to the boiling point of water, size distribution of gold nanoparticles becomes broader. At 130 °C, different shapes (cube, triangle) of nanoparticles also evolved. These are due to the annealing of stabilizer (CTAB) layers at high temperature, causing it to rupture around the growing nanoparticles. The growth rate of gold nanoparticles increased as the stabilizer layer turned thinner. Also, the rupturing process can lead to anisotropic growth of nanoparticles and result in the evolution of nanoparticles with different shapes.<sup>106</sup>

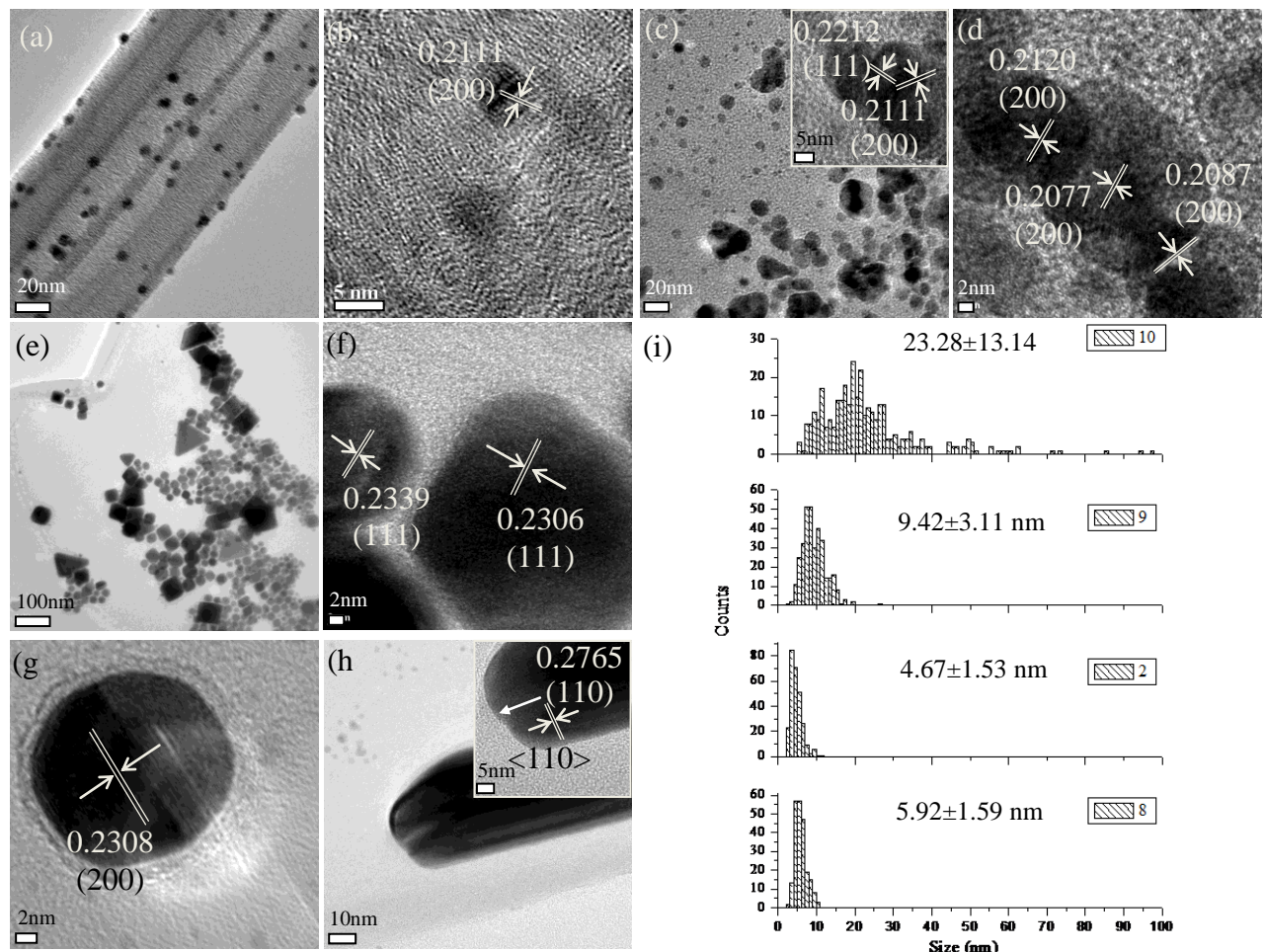


Figure 3.3 TEM images of AuNPs (table 2.1, sample 8-10) synthesized using different metal salt (HAuCl<sub>4</sub>.3H<sub>2</sub>O) concentration: (a, b)  $5 \times 10^{-6}$  M, (c, d)  $5 \times 10^{-4}$  M, (e, f, g, h)  $5 \times 10^{-3}$  M, and (i) histogram showing AuNPs size distributions.

*Metal salt ( $HAuCl_4 \cdot 3H_2O$ ) concentration:* TEM images and size distribution histogram for gold nanoparticles with different metal salt concentration are summarized in figure 3.3. As the increase of  $HAuCl_4 \cdot 3H_2O$  concentration, gold nanoparticles with larger size and broader size distribution were observed. Increasing the metal salt concentration resulted the increase of supersaturation, which reduced critical free energy ( $\Delta G^*$ ) and critical size ( $r^*$ ) for nucleus. According to equation 3.6, the possibility for nucleation ( $P$ ) was increased at the same time, ultimately resulted in high nucleation rate ( $R_N$ ). Meanwhile, high metal salt concentration gradient provided sufficient growth species around the nuclei and increased flux of gold ions, drives the nuclei grow into big particles. The broad size distribution suggests a high driving force for particle growth and a continuous nucleation process.

Since the surfactant CTAB molecules bind stronger to the {100} facets than the (111) facets,<sup>20</sup> the growth rate of each facet varies. A large amount of gold nanoparticles with different shapes (hexagon, rhombus, square, and triangle) were observed when metal salt concentration increased to  $5 \times 10^{-3}$  M, indicating that the surfactant is not sufficient to form tightly packed micelle around nanoparticles, thus the rate of anisotropic growth is high enough to generate gold nanoparticles with different shapes.

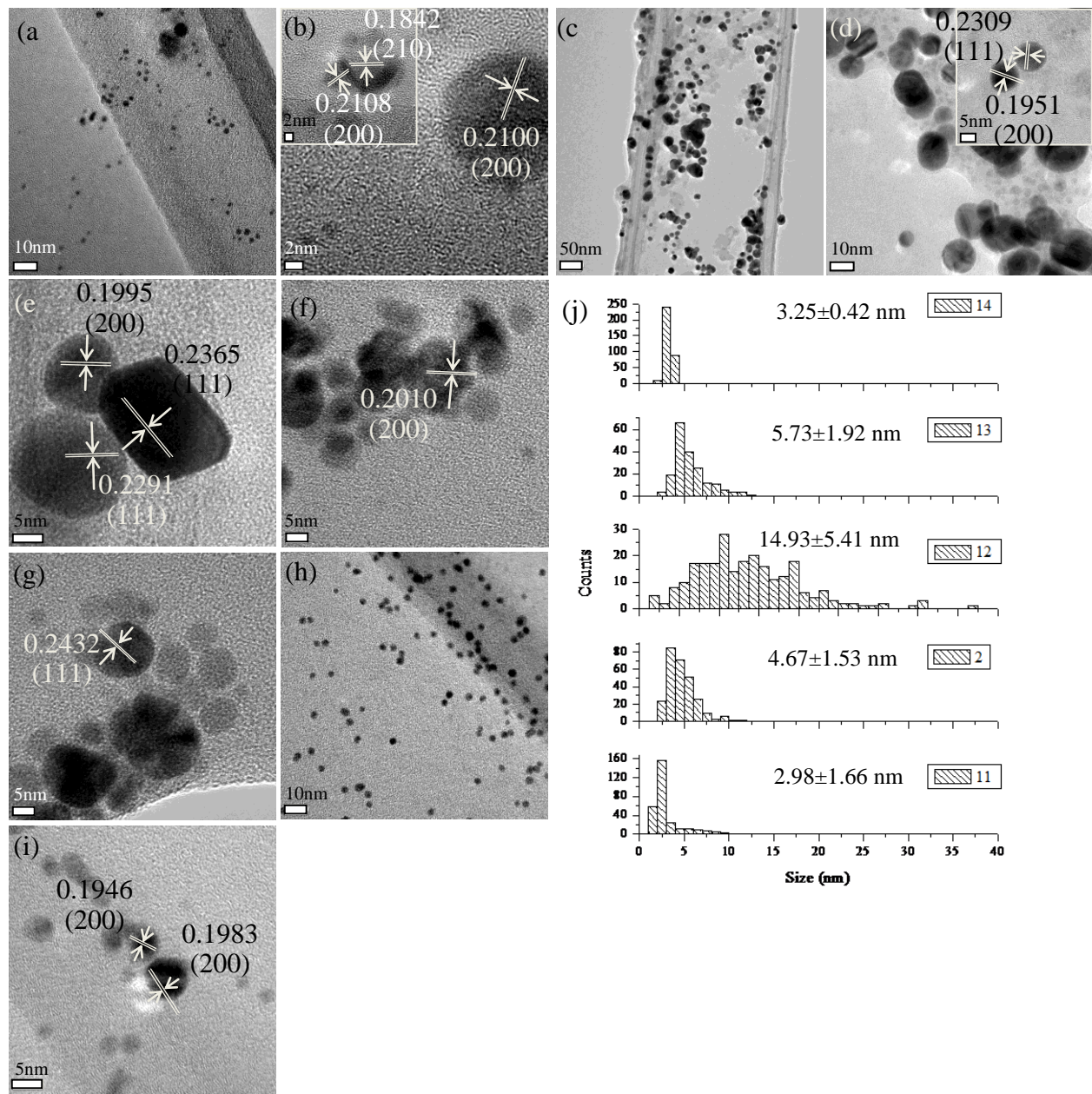


Figure 3.4 TEM images of AuNPs (table 2.1, sample 11-14) synthesized from different surfactants: (a, b) PVP, (c, d, e) KBr, (f, g) MPTMS, (h, i) PVA, and (j) histogram showing AuNPs size distributions.

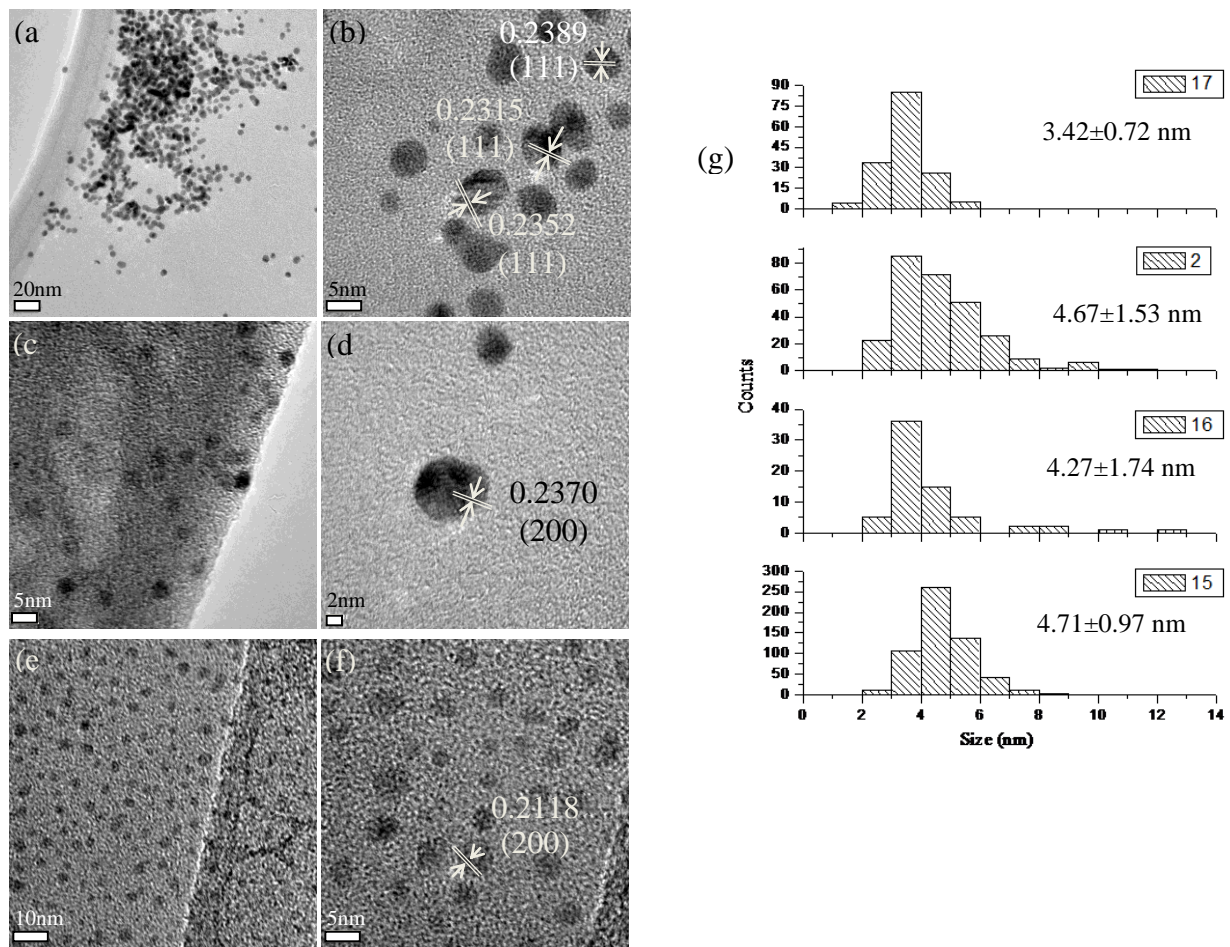


Figure 3.5 TEM images of AuNPs (table 2.1, sample 15-17) synthesized using different CTAB concentration: (a, b) 0 M, (c, d) 0.0074 M, (e, f) 0.8 M, and (g) histogram showing AuNPs size distributions.

*Effects of surfactant type and concentration:* To study the effect of different surfactant and the concentration on the morphology of gold nanoparticles, hexadecyltrimethylammonium bromide (CTAB), polyvinyl alcohol (PVA), polyvinylpyrrolidone (PVP), 3-mercaptopropyltrimethoxysilane (MPTMS), and potassium bromide (KBr) were used with the same concentration as capping agent for synthesis of gold nanoparticles. Also, the concentration of CTAB was tuned from 0 M to 0.8 M to study size and shape change of AuNPs. CTAB is widely used as a soft template in gold nanorods and nanowires synthesis. The molecule of CTAB is constituted by a hydrophilic head group and a hydrophobic carbon tail. In aqueous solution, a bilayer of CTAB will form on the surface of gold.<sup>32</sup> The first layer of CTAB bind to gold surface through the hydrophilic cationic head group (quaternary ammonium), and the hydrophobic carbon tails of bilayer CTAB will be packed together, leaving the hydrophilic head group from second layer CTAB facing to the bulk solution. Organic polymer PVA and PVP are also used as stabilizer in the synthesis of gold nanoparticles.<sup>107 108</sup> MPTMS is terminated with thiol group, which can strongly bind on the surface of gold.<sup>109</sup> These molecules can interact with gold nanoparticles with head group, while the thickness of the barrier layer can be tuned by molecules' tail groups. It was observed that PVP and PVA resulted in small-sized gold nanoparticles ( $2.98 \pm 1.66$  nm, and  $3.25 \pm 0.42$  nm, respectively). This may attributed to the thick polymer layer stabilizing the gold nuclei, which impeded the growth of the nanoparticles. In case of MPTMS, the particle size increased slightly as compared to polymer stabilizers. This may due to the packing of MPTMS on gold is not efficient enough, and certain extent of self-polymerization of MPTMS is also possible since it was in aqueous solution.

The role of bromide ions in morphological evolution of gold nanoparticles is a matter of debate. It is generally agreed that the ionic head group of CTAB ( $\text{CTA}^+$ ) stabilizes the nanorods

by forming a bilayer on gold surface. However, it was observed that only spherical nanoparticles are formed when CTA-Cl is used as surfactant.<sup>13</sup> So, Br<sup>-</sup> must play an important role in morphology control of gold nanoparticles synthesis. Garg and co-workers<sup>110</sup> proposed that Br<sup>-</sup> ions are adsorbed on gold by forming covalent bonds similar to Au-Br-Au bridging motifs, which could lead to gold nanoparticles growth and their broad size distribution.

The reduction in gold nanoparticles' size was observed as the increase of CTAB concentration, as shown in figure 3.5. This could attribute to tight packing of surfactant around the gold nuclei thus results in increasing of diffusion barrier for the metal salt. The viscosity of CTAB solution with different concentration can be found from related papers: at CTAB concentration of 0 M, 0.0074 M, 0.0294 M and 0.8 M, the viscosity of solution are 1.002 cP (DI water), 28.86 cP, 110.25 cP, and 30000 cP.<sup>111 112</sup> According to equation 3.7, for growth species with same size and at certain temperature, the jump frequency  $\Gamma$  will dramatically decrease as solution viscosity increase from 1.002 cP to 30000 cP (around 30000 times). But considering the low concentration of metal salt (HAuCl<sub>4</sub>) and strong reducing ability of NaBH<sub>4</sub>, HAuCl<sub>4</sub> can be easily consumed. And by given sufficient time, gold nanoparticles can still nucleate and grow even at high viscosity solution. Thus no dramatically decrease of nanoparticle size in high viscosity solution was observed. The change will be more noticeable at high concentration of metal salt.

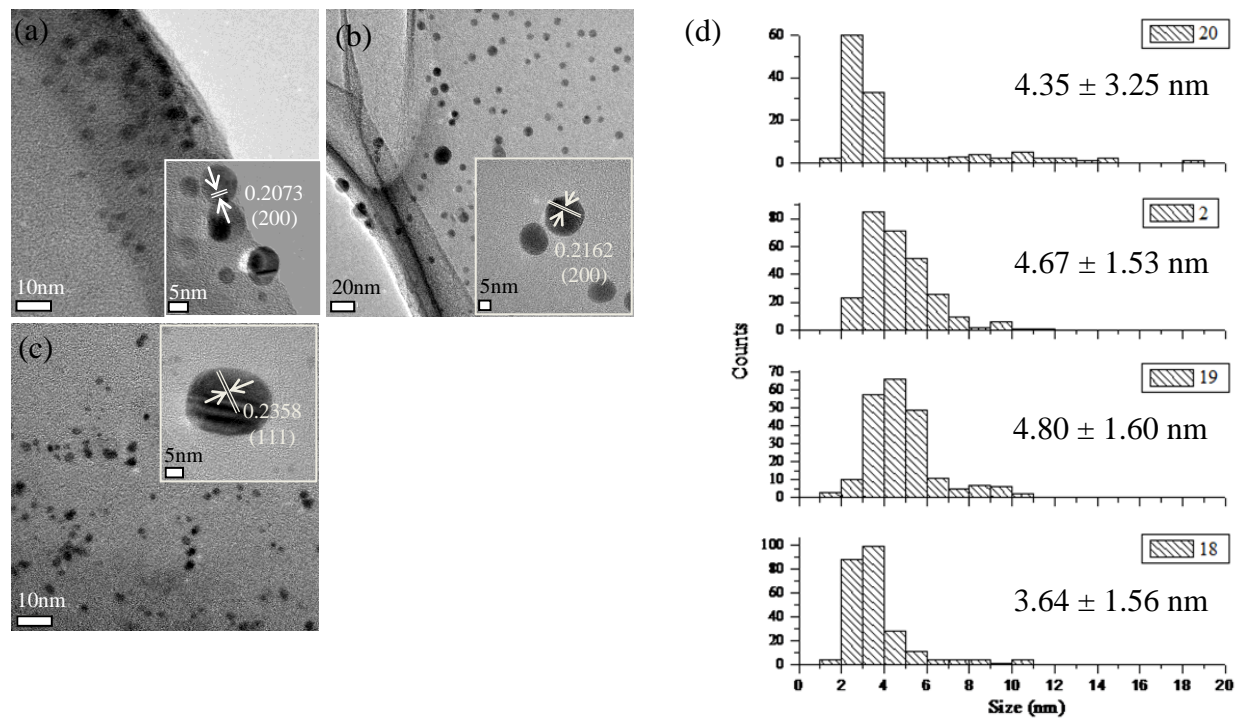


Figure 3.6 TEM images of AuNPs (table 2.1, 18-20) synthesized for different growth duration:  
 (a) 0.25 h, (b) 0.5 h, (c) 24 h, and (d) histogram showing AuNPs size distributions.

*Effect of duration:* The nucleation and growth of nanoparticles will proceed only if the concentration of solution is above a specific minimum concentration to overcome the Gibbs free energy barrier. For a system with given concentration of metal salt, the growth of gold nanoparticles is slowed down once the significant amount of metal salt is consumed. In our case, strong reducing agent NaBH<sub>4</sub> will result in a very fast consumption of the metal salt. In order to estimate how long the reaction last and to study the morphology evolution of gold nanoparticles in certain duration, gold nanoparticles were characterized from the same solution after adding reagents for 0.25 h, 0.5 h, 2 h, and 24 h, the results are shown in figure 3.6. Increasing of size was observed in first 0.25 h, after that, the size of synthesized gold nanoparticles unchanged. This indicates that reaction can be finished in 30 min and the as-synthesized nanoparticles were stable in the solution. The changes of nanoparticle size with each parameter in single-step were plot in figure 3.7.

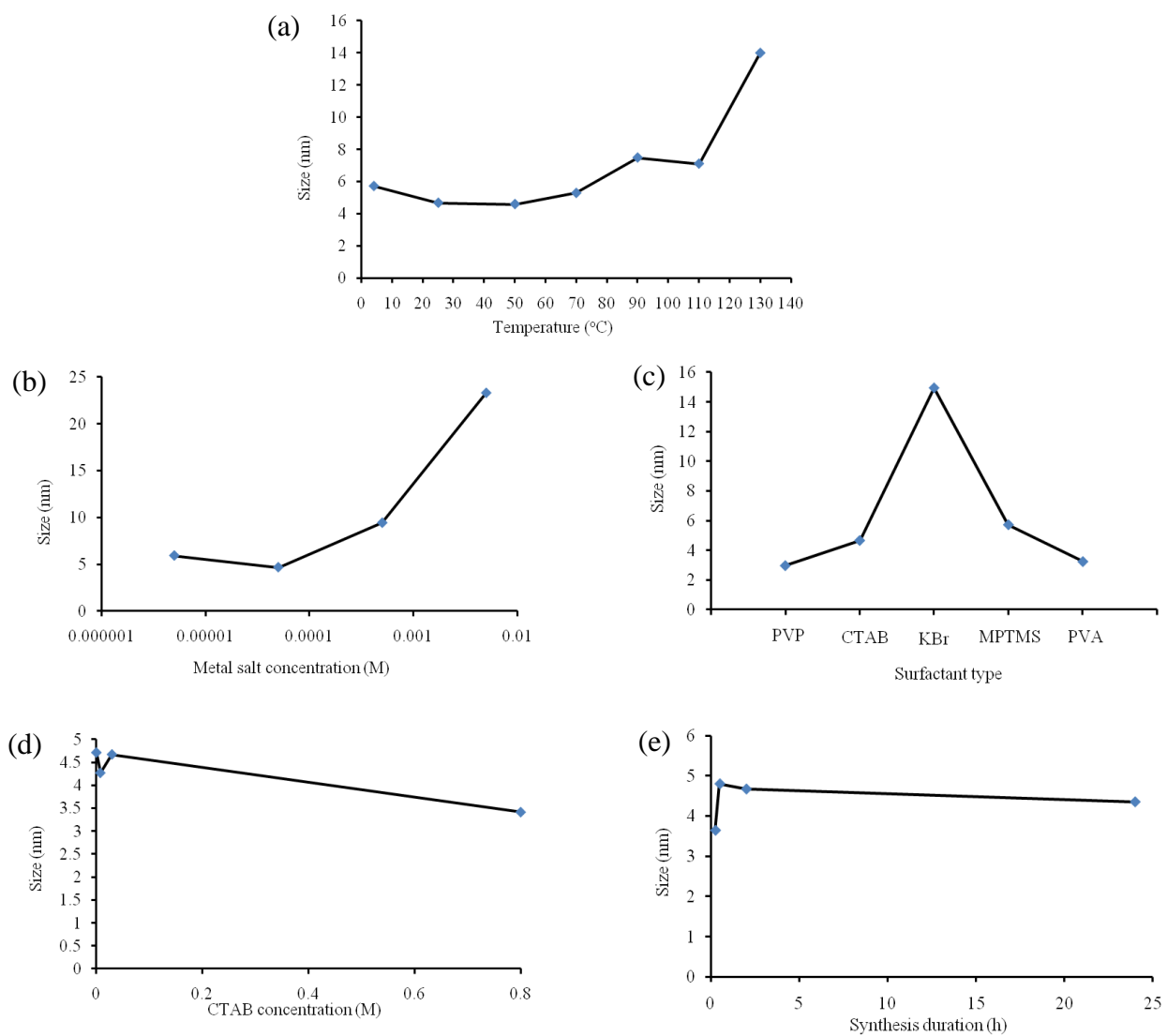


Figure 3.7 The change of gold nanoparticle size with different parameters: (a) temperature, (b) metal salt concentration, (c) surfactant type, (d) CTAB concentration, and (e) synthesis duration.

Table 3.2 Results summarizing the effect of quenching (table 2.2, sample 21-23) on AuNPs prepared at higher temperature (130 °C), indicating size, shape distribution, lattice spacing and the corresponding plane for after-quenched AuNPs.

Sample number	Average size (nm)	Shape distribution	Lattice spacing (nm) and the corresponding plane
21	$28.77 \pm 7.8$	Triangle: 11.5%; Cubic: 5.1%; Rod: 2.6%; Spherical: 80.8%.	$0.2342 \pm 0.001$ (111)
22	$27.65 \pm 7.81$	Triangle: 6.3%. Cubic: 3.6%; Rod: 2.7%; Spherical: 87.4%.	0.2082 (200) 0.2196 (111)
23	$14.53 \pm 3.43$	Spherical	$0.2329 \pm 0.002$ (111) $0.2041 \pm 0.004$ (200)

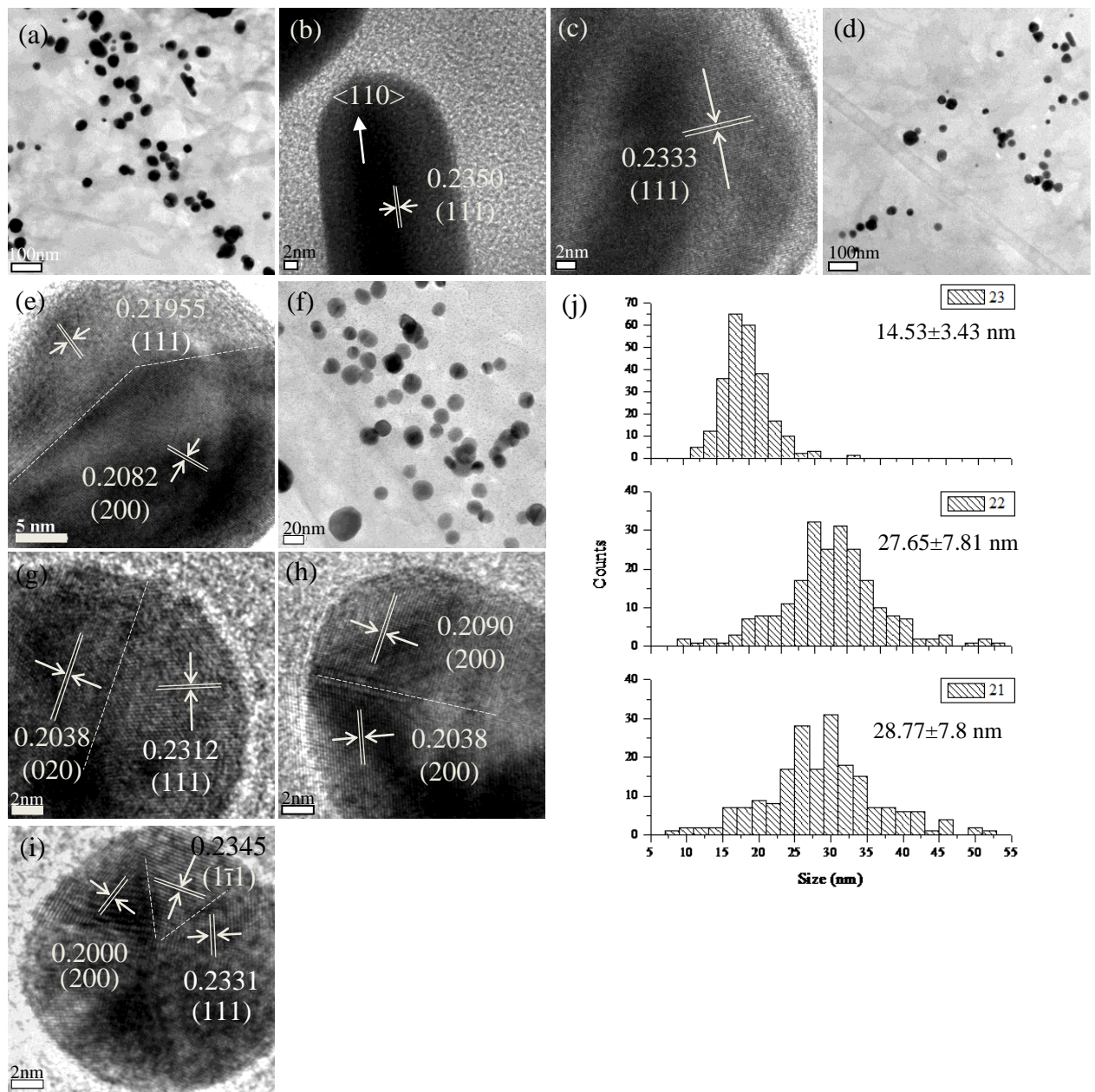


Figure 3.8 TEM images of AuNPs (table 2.2, sample 21-23) synthesized at 130 °C and then quenched at (a, b, c) 10 °C, (d, e) 0 °C, (f, g, h, i) -20 °C, and (j) histogram showing AuNPs size distributions.

*Effect of quenching:* Gold nanoparticles were first synthesized at 130 °C for 2 h. After reaction, the as-prepared gold solutions were immediately quenched at 10 °C, 0 °C, and -20 °C, respectively. It was observed that quenching process results in various crystal defects in nanoparticles. The defect formation was significant in case of lowest quenching temperature, at which nanoparticles developed not only twin boundaries but also resulted in vacancy defects and dislocations. Chopra et al.<sup>106</sup> also reported quenching process for nickel nanoparticles. The defect formation can be attributed to the sudden cessation of atomic level diffusion in the hot nanoparticle solution when it was quenched at low temperature. This also leads to straining of nanoparticle lattice. Comparing to the as-prepared gold nanoparticle solution before quenching, there is a noticeable increase in the size of quenched samples. The increase of nanoparticles size may be attributed to the rupture of surfactant during high-temperature synthesis, and the exposure of more active spots on particles, allowed further growth in aqueous where metal source ions also remain high activity before temperature decline. At lower temperature, the temperature decrease faster, and nucleation and growth of nanoparticles would be inhibited faster. This is further proved by the fact that as quenching temperature decrease, the resulting quenching sample has an average size closer to the size of sample before quenching.

### 3.1.2 Synthesis gold nanoparticles in seed-growth method

In this method, gold nanoparticles seed solution was first synthesized following similar method with single-step synthesis. Then as-prepared seed solution was added into aqueous mixture containing metal salt, CTAB, and weak reducing agent L-ascorbic acid (AA). The effects of parameters such as CTAB concentration, seed amount, temperature, and growth duration were studied. The seeding and growth conditions are listed in table 2.3 and 2.4 in experimental part. After synthesis, the morphologies and lattice fringes were observed for as-prepared gold nanoparticles through TEM, and results are summarized in table 3.3.

Figure 3.9 (a) is a schematic shows the color change of a typical seed-growth process. In seed-growth synthesis, (b - e) are TEM images of Au seed, and (f) shows the histogram for seed size distribution. Before adding seed, metal salt ( $\text{HAuCl}_4$ ) was first reduced by weak reducing agent AA from  $\text{Au}^{3+}$  to  $\text{Au}^+$ ,<sup>20</sup> indicated from the disappearance of the yellow color of solution (AA is too weak to reduce  $\text{Au}^{3+}$  to  $\text{Au}^0$ ). In seed-growth process, nucleation is heterogeneous because of the existence of nucleus. It is widely accepted that seeds can serve as nucleation centers for the reduction of metal ions at their surfaces.<sup>113</sup> However, for a  $\text{Au}_{\text{atom}}/\text{Au}^+$  (aqueous) system, the reduction potential is -1.5 V (vs. NHE), whereas the reduction potential of AA is +0.125 V (vs. NHE), not negative enough to reduce gold salt.<sup>114</sup> So, seed particles not just provide the surface for the growth of gold nanoparticles, but also catalyze the reduction processes through particle-mediated electron transfer from AA to gold ions.<sup>115</sup>

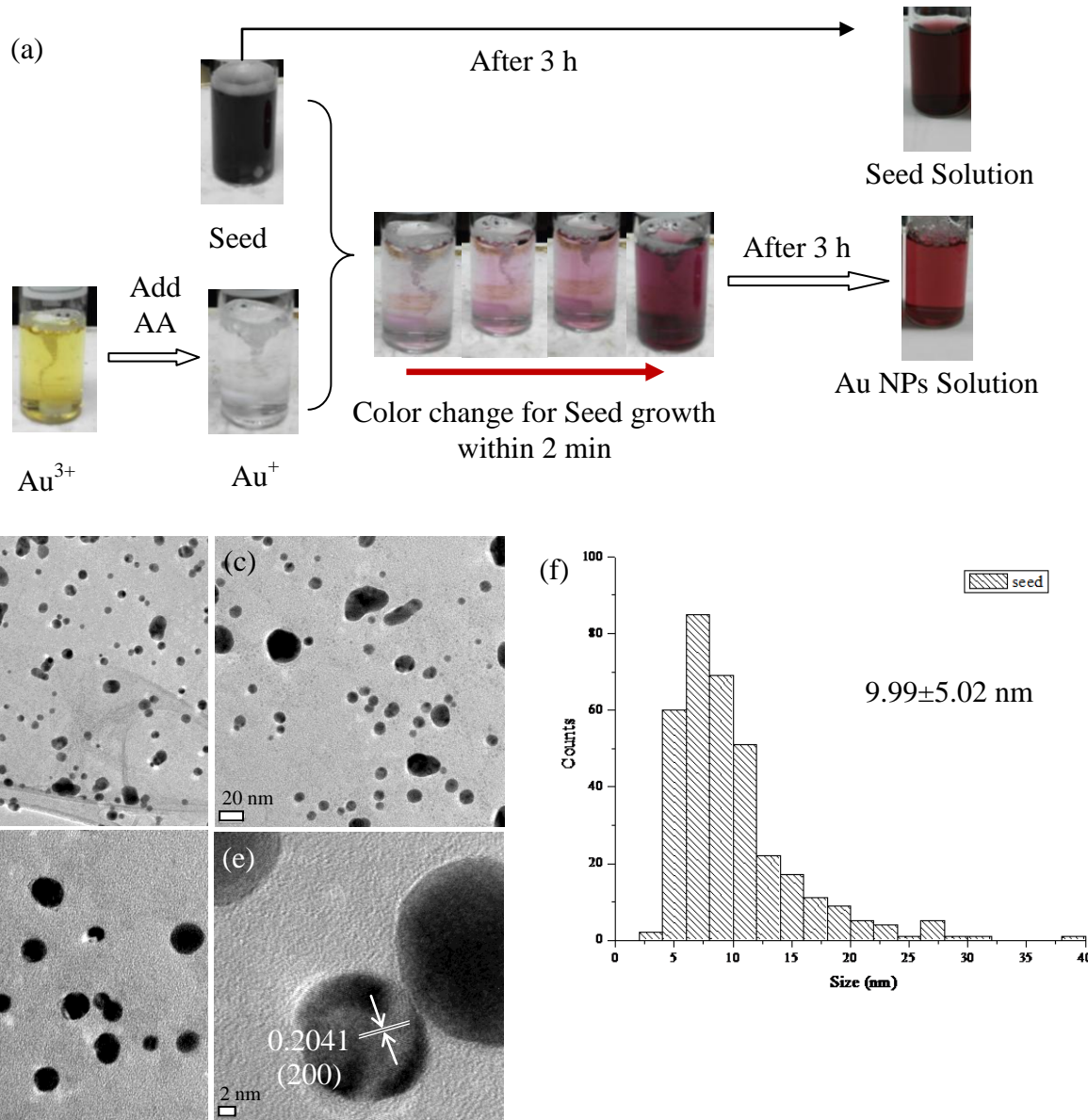


Figure 3.9 (a) A schematic showing the color change of a typical seed-growth process. (b - e) TEM images of Au seeds (table 2.3) and (f) a histogram showing AuNPs size distributions.

Table 3.3 Result summary for systematic study indicating size, shape distribution, lattice spacing, and the corresponding planes for the as-prepared AuNPs according to the table 2.4.

Sample number	Average size (nm)	Shape distribution	Lattice spacing (nm) and the corresponding plane
1	19.44±12.31	Hexagon: 4.5%; Pentagon: 0.2%; Rod: 1.0%; Triangle: 1.6%; Spherical: 92.7%.	0.2025 (200) 0.2321±0.008 (111)
2	15.93 ± 2.38	Oval: 0.8%; Rod: 3.7%; Triangle: 1.6%; Spherical: 94.7%	0.2025 (200) 0.2408 (111)
3	7.73±3.28	Hexagon: 0.2%; Rhombus: 0.2%; Triangle: 0.2%; Spherical: 99.4%.	0.2306 (111)
4	27.49±11.32	Spherical	0.2077 (200)
5	22.44±5.38	Hexagon: 0.4%; Rod: 18.9%; Square: 4.2%; Triangle: 10.5%; Spherical: 66.4%.	0.2037 (200)
6	17.73±6.14	Rod: 51%; Rhombus: 1.14%; Square: 1.14%; Triangle: 6.9%; Spherical: 39.8%.	0.2317 (111)
7	13.94±2.70	Oval: 3.2%; Rod: 5.6%; Triangle: 2.4%; Spherical: 88.8%	0.2351 (111)
8	23.64±14.33	Oval: 8.1%; Pentagon: 0.5%; Rod: 2.0%; Rhombus: 2.0%; Square: 0.5%; Triangle: 6.6%; Spherical: 80.3%	0.2296 (111)
	0~10nm		
	3.78±1.32		
9	10~350nm		
	29.69±10.50		
10	15.64±2.74	Oval: 3.9%; Rod: 1.0%; Triangle: 3.9%; Spherical: 91.2%	0.2382 (111)
11	16.62±2.56	Oval: 1.9%; Rod: 2.4%; Triangle: 1.9%; Spherical: 93.8%	0.2377 (111)
11	17.60±2.57	Rod: 4.2%; Triangle: 3.4%; Spherical: 92.4%	0.2255±0.015 (111) 0.2037 (200)

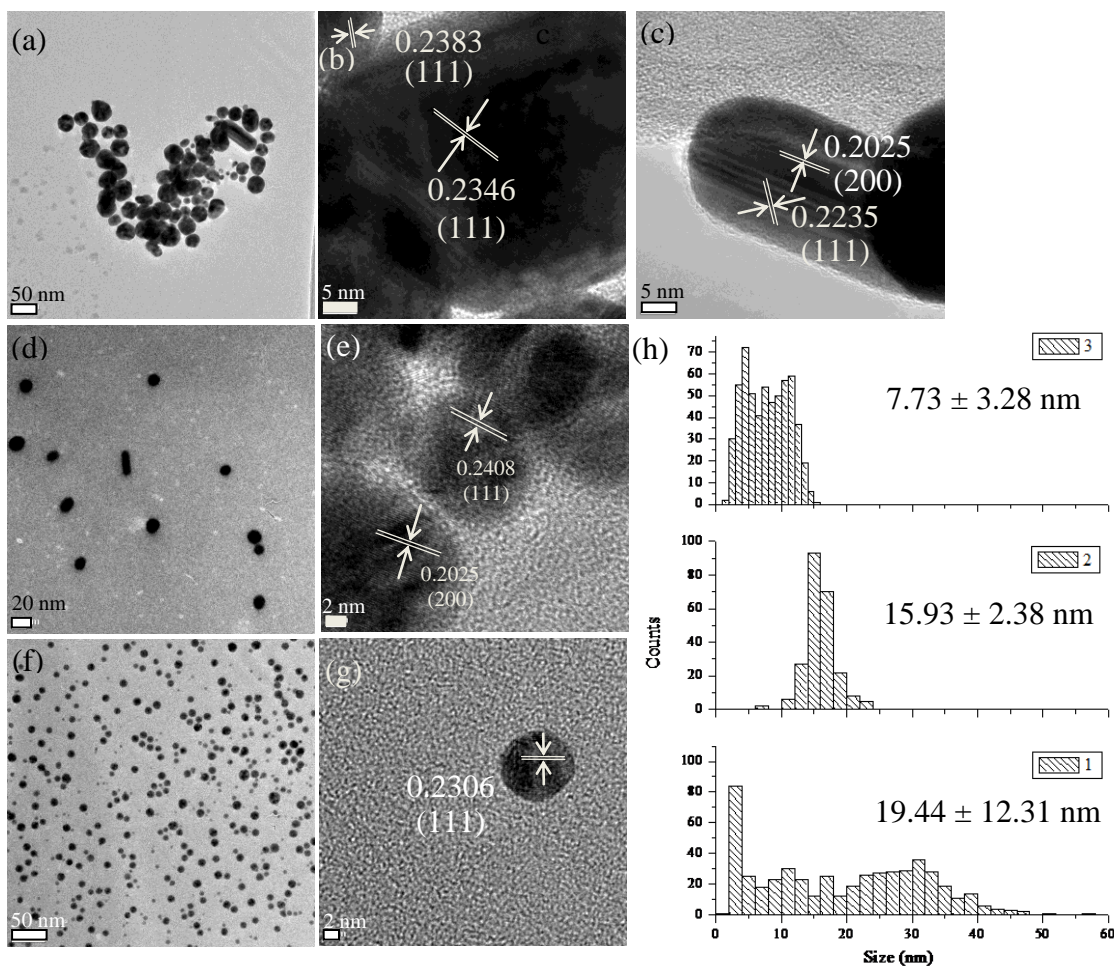


Figure 3.10 TEM images of AuNPs (table 2.4, sample 1-3) synthesized using different CTAB concentrations: (a, b, c) 0 M, (d, e) 0.075 M, (f, g) 0.5 M, and (h) histogram showing AuNPs size distributions.

*Effect of CTAB concentration:* Increasing the concentration of surfactant (CTAB), both average size and size distribution decreased, which is shown in figure 3.10 (from  $19.44 \pm 12.31$  nm to  $7.73 \pm 3.28$  nm). The size distribution of nanoparticles depends on the interplay between the nucleation and growth during the process. Without addition of CTAB in growth-step (sample 1, table 2.4), a large size distribution exists. The existence of numerous small particles suggests a high nucleation rate during the process, demonstrates that the presence of seeds not only serve as nucleus for further growth, but also appears to cause additional nucleation.<sup>116 117</sup> A slight amount of CTAB was induced from seed solution for the growth of sample 1 (table 2.4). The weak barrier layer favored the growth of gold, generated big size nanoparticles; meanwhile, the slight amount of CTAB still can selectively bound to different facets, inducted anisotropic growth and resulted in different shapes.<sup>20</sup>

As discussed in single-step method, the increase of CTAB concentration will lead to a tight packed barrier surround the seed, thus impede the mass transfer of gold ions to the surface of gold nanoparticles and reduce the growth rate. The viscosity of CTAB solution at concentration of 0 M, 0.075 M, and 0.5 M are 1.002 cP, 240 cP, and 15000 cP, respectively.<sup>111</sup>,<sup>112</sup> According to equation 3.10, for same size growing species at certain temperature, diffusion coefficient  $D_1:D_2:D_3 = \frac{1}{\eta_1}:\frac{1}{\eta_2}:\frac{1}{\eta_3} \approx 1:\frac{1}{240}:\frac{1}{15000}$ . Thus the diffusion rate of gold ions would be slow down at high concentration CTAB concentration, and gold seeds could not grow bigger. It should be noticed that the average size of sample 3 (table 2.4) is less than the average size of seed; and the amount of small size particles in sample 3 is large. This suggests that the nucleation still took place at high concentration of CTAB, and generated more small gold nanoparticles. Thus the average size of gold nanoparticles for sample 3 was shrinking down.

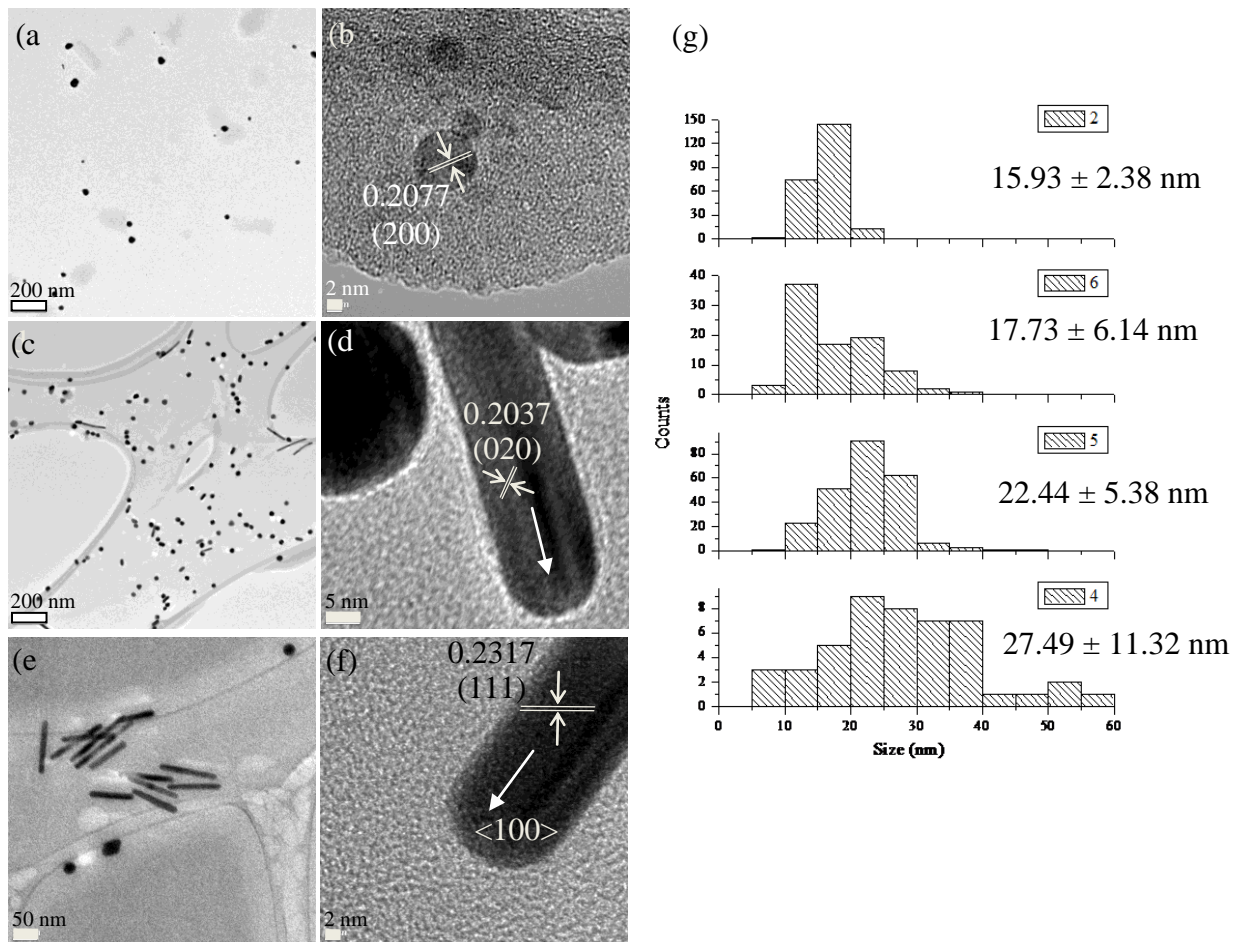


Figure 3.11 TEM images of AuNPs (table 2.4, sample 4-6) synthesized by adding different amount of seed solution: (a, b) 0.0005 mL, (c, d) 0.0625 mL, (e, f) 0.125 mL, and (g) histogram showing AuNPs size distributions.

*Effect of seed amount:* The seed amount plays an important role in morphological evolution of nanoparticles, the effect of adding different amount of seed in growth process is shown in figure 3.11. It was observed that both size and size distribution of the nanoparticles were lowered down as increasing the amount of seed. In a certain concentration of metal salt, less amount of nucleus, more gold ions could anchored on each nucleus and result in bigger nanoparticles. Thus the size of gold nanoparticles was bigger seed amount was small. Moreover, Jana et al.<sup>115</sup> observed that a smaller amount of seeds can lead to a burst of nucleation. This may explain the narrower size distribution when larger amount of seeds applied to the system.

*Effect of temperature:* Gold nanoparticles were synthesized at different temperature in the growth step. According to Stokes-Einstein equation (equation 3.10):  $\frac{D_1}{D_2} = \frac{T_1}{T_2} \cdot \frac{\eta_2}{\eta_1}$ . If assuming the viscosity maintained at different temperature, the diffusion coefficient at 25 °C, 90 °C, and 130 °C would be  $D_{298K}:D_{363}:D_{403K} = 298:363:403 \approx 1:1.22:1.35$ . Actually, the viscosity would decrease as temperature increase, so the diffusion coefficient would increase more at high temperature. TEM images and size distribution histogram are shown in figure 3.12. It was observed that, as temperature increased higher than the boiling point of water, the size of gold nanoparticles increased. The size of gold nanoparticles synthesized at 90 °C is slightly smaller than 25 °C. This can be attributed to: (1) according to calculation, the increase of diffusion coefficient does not remarkably increase in the studied temperature range; (2) More nanoparticles with oval-shape were synthesized at 90 °C, and the measured size for an oval particle is smaller than a spherical particle with same volume. Increasing the temperature higher than boiling point of water, the annealing causes the rupture of stabilizer layer around the growing species. This can dramatically increase the diffusion of gold ions to the surface of gold

nanoparticles and result in bigger size nanoparticles. Nucleation rate was also accelerated because of seeds, leading to the generation of small particles and broadening of size distribution.

*Effect of duration:* Gold nanoparticles were sampled after different growth duration. TEM images and size distribution histogram are shown in figure 3.13. An increase of nanoparticle size was observed, indicates that nanoparticles were grown fast in the first 1 h, and kept growing within 24 h in a slow rate. The changes of nanoparticle size with each parameter in seed-growth method were plot in figure 3.14.

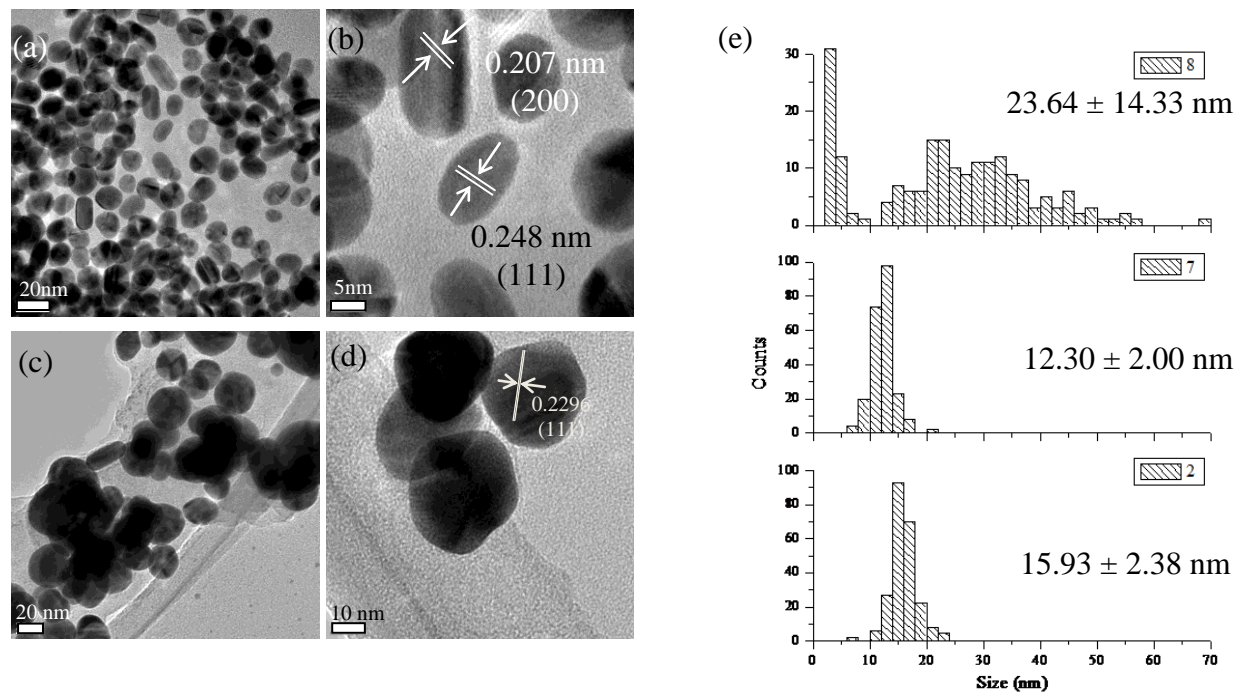


Figure 3.12 TEM images of AuNPs (table 2.4, sample 7-8) synthesized at different temperatures:  
 (a, b) 90 °C, (c, d) 130 °C and (e) histogram showing AuNPs size distributions.

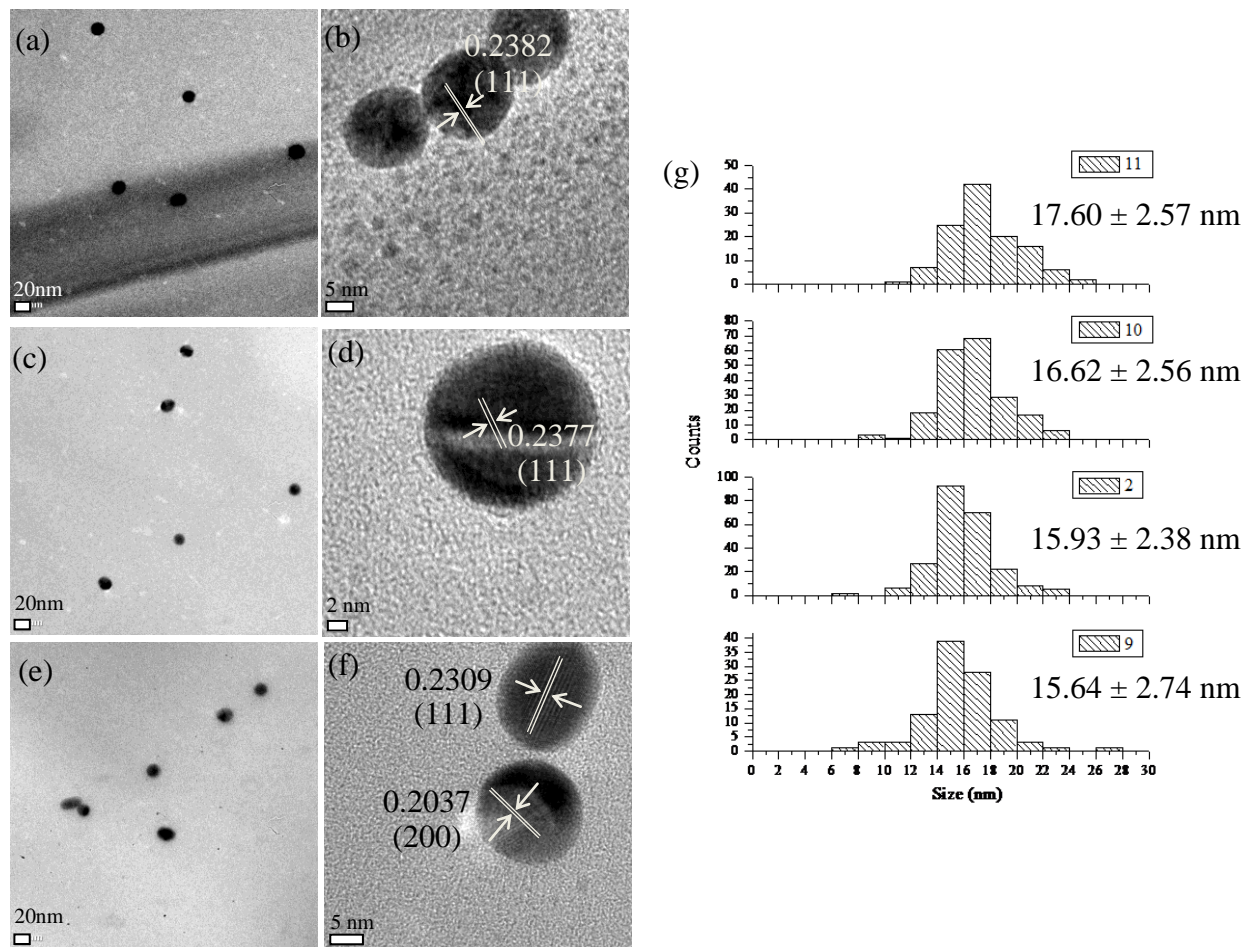


Figure 3.13 TEM images of AuNPs (table 2.4, sample 9-11) synthesized for different growth duration: (a, b) 1h, sample 9; (c, d) 9 h, sample 10; (e, f) 24 h, sample 11, and (i) histogram showing AuNPs size distributions.

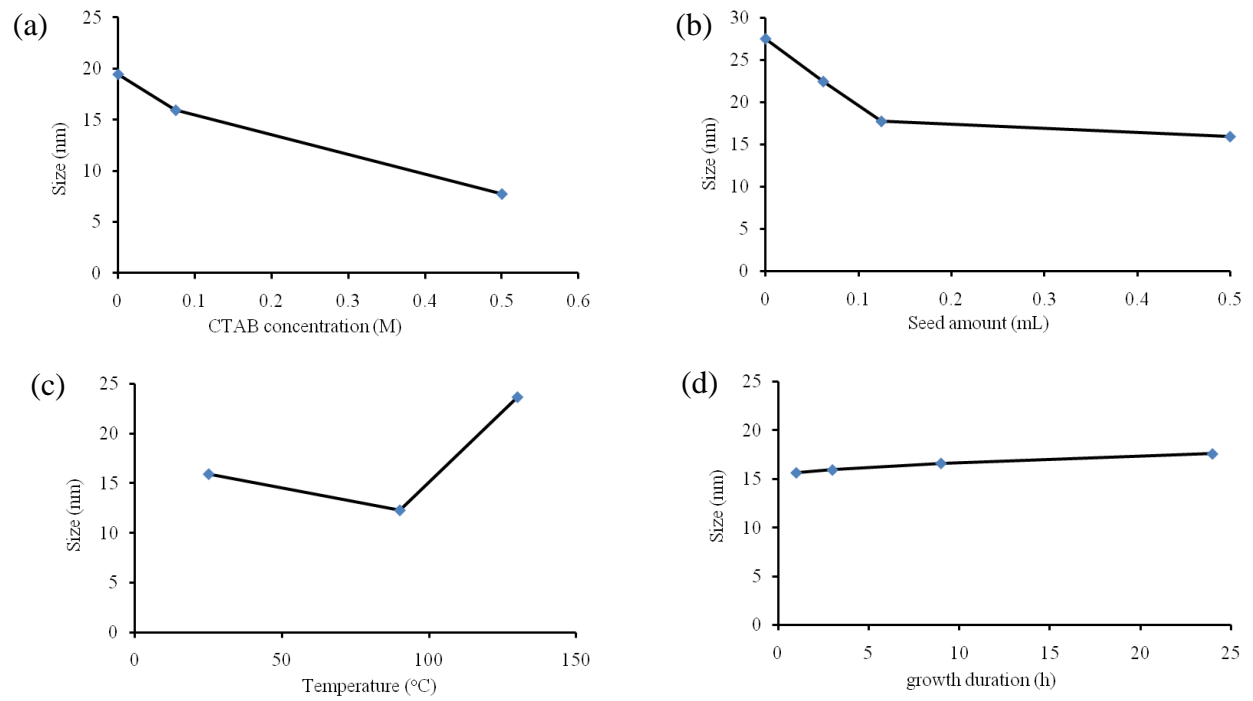


Figure 3.14 The change of AuNPs size with different parameters: (a) CTAB concentration, (b) seed amount, (c) temperature, (d) growth duration.

### *3.2 Synthesis and characterization of palladium nanoparticles*

Based on the study for gold nanoparticles synthesis, the systematic study for palladium nanoparticles was approached in a similar way. In this study, synthesis conditions such as PVP concentration, metal salt concentration, temperature, and synthesis duration were varied one parameter at a time (table 2.5). Average size, distribution of shapes, lattice spacing and the corresponding planes are summarized in table 3.4. TEM images and histograms of nanoparticle size distribution are shown in figure 3.15 to 3.18.

A decrease of nanoparticle size and a narrow size distribution was observed when higher amount of PVP was added. PVP is a widely used stabilizer for nanoparticle synthesis.<sup>118</sup> Increasing of PVP concentration resulted in the increase of capping layer thus hinder the growth of nanoparticles; so, the sizes of palladium nanoparticles decrease. It was observed that larger size and broad size distribution was obtained as increase metal salt concentration. This is attributed to a higher supersaturation of metal salt boost the nucleation and growth rate. We observed particles with larger size and broad size distribution when increasing temperature. As temperature increased from 100 °C to 150 °C, particle size changed from  $3.62 \pm 1.16$  nm to  $5.33 \pm 3.15$  nm, the shape of size distribution histograms suggest the existence of Ostwald ripening at high temperature. This is further supported in synthesis duration set: as the duration increase, the sizes of nanoparticles gradually increase, broaden the size distribution. The changes of nanoparticle size with each parameter in single-step were plot in figure 3.19.

Table 3.4 Result summary for systematic study indicating average size, shape distribution, lattice spacing, and the corresponding planes for the as-prepared PdNPs according to the table 2.5.

Sample number	Average size (nm)	Shape distribution	Lattice spacing (nm) and the corresponding plane
1	6.32±2.69	Hexagon: 4.2%, Triangle: 1.3%, Spherical: 94.5%	0.2346±0.004 (111)
2	6.21±3.84	Hexagon: 4.2%, Rhombus: 0.8%, Square: 0.4%, Triangle: 1.7%, Spherical: 92.9%	0.2319±0.008 (111)
3	3.62±1.16	Hexagon: 2.8%, Triangle: 0.9%, Pentagon: 0.9%, Square: 0.9%, Spherical: 94.5%	0.1975 (200) 0.2335±0.001 (111)
4	4.01±1.81	Hexagon: 3.4%, Pentagon: 0.5%, Rhombus: 0.2%, Square: 0.7%, Triangle: 0.2%, Spherical: 95%	0.2012 (200) 0.2315±0.003 (111)
5	4.48±2.05	Hexagon: 1.4%, Rhombus: 0.9%, Square: 2%, Triangle: 3.7%, Spherical: 92%	0.2336±0.011 (111) 0.1958 (200)
6	4.53±1.66	Hexagon: 0.2%, Pentagon: 0.4%, Rhombus: 0.6%, Square: 0.6%, Triangle: 0.8%, Spherical: 97.4%	0.2044 (200) 0.2301±0.005 (111)
7	8.44±2.87	Hexagon: 7.6%, Rod: 0.8%, Rhombus: 3%, Square: 2.3%, Triangle: 3%, Spherical: 83.3%	0.2296±0.003 (111)
8	5.23±3.65	Hexagon: 3.6%, Pentagon: 0.65%, Rhombus: 2.8%, Square: 0.43%, Triangle: 1.9%, spherical: 90.62%	0.1975 (200) 0.2287±0.002 (111)
9	5.33±3.15	Hexagon: 1.8%, Pentagon: 0.3%, Rhombus: 0.6%, Square: 0.9%, Triangle: 2.4%, Spherical: 94.0%	0.2037(200) 0.2286±0.003 (111)
10	4.66±2.11	Hexagon: 1.9%, Pentagon: 0.8%, Square: 1.3%, Triangle: 3.2%, Spherical: 93.8%	0.2025±0.002 (200) 0.2290±0.005 (111)
11	6.76±3.80	Hexagon: 2.4%, Pentagon: 0.3%, Rod: 0.3%, Rhombus: 1.5%, Square: 1.2%, Triangle: 1.5%, Spherical: 92.8%	0.2289±0.001 (111) 0.1993 (200)
12	8.09±4.04	Hexagon: 4.4%, Pentagon: 0.4%, Rod: 0.4%, Rhombus: 0.3%, Square: 1.6%, Triangle: 1.5%, Spherical: 91.4%	0.2304±0.007 (111) 0.1988 (200)
13	17.36±2.60	Cubic 89.6%; Triangle: 8.3%; Pentagon: 2.1%	0.1958±0.002 (200)

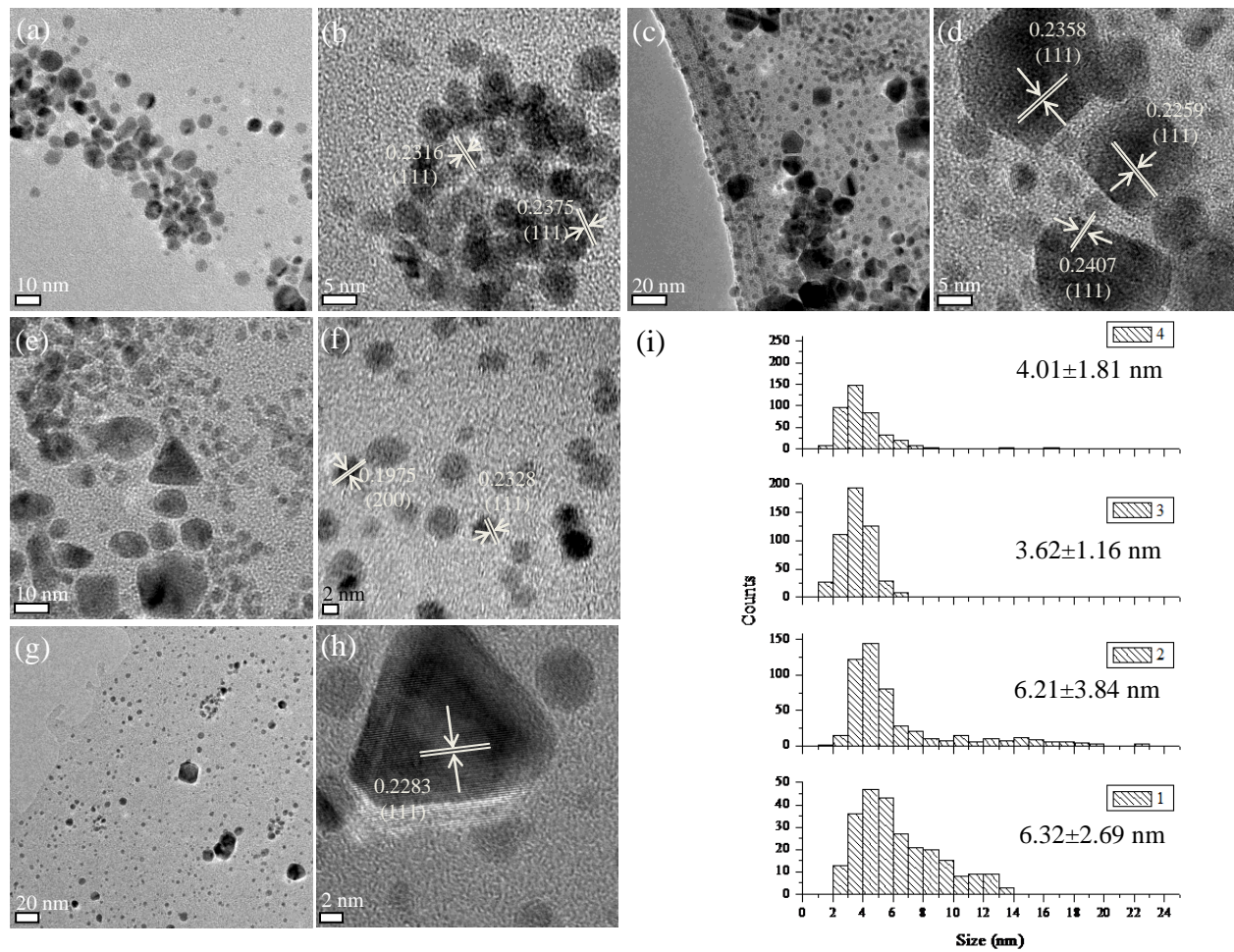


Figure 3.15 TEM images of PdNPs (table 2.5, sample 1-4) synthesized using different PVP concentrations: (a, b) 0.261 mM, (c, d) 0.522 mM, (e, f) 1.044 mM, (g, h) 2 mM, and (i) histogram showing PdNPs size distributions.

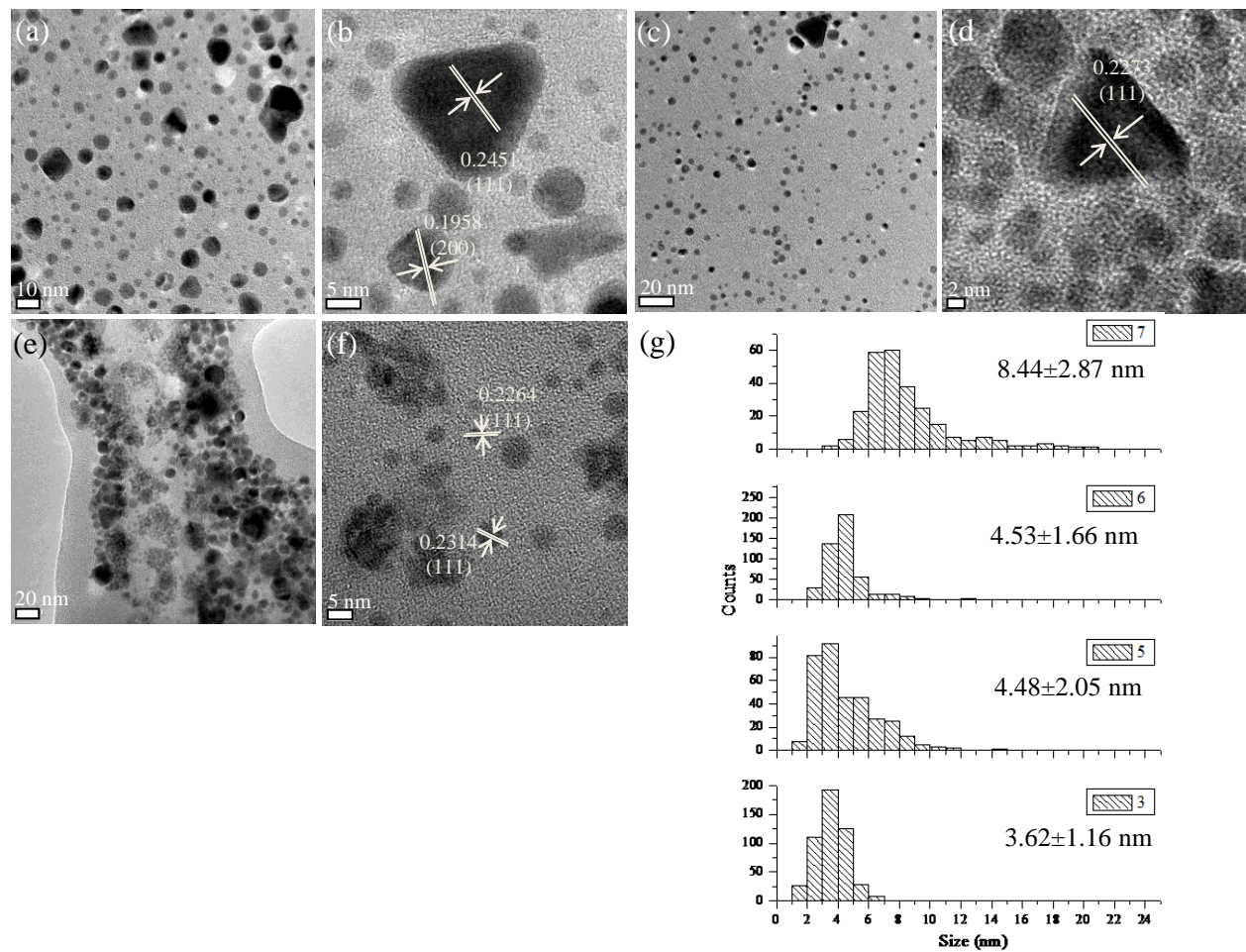


Figure 3.16 TEM images of PdNPs (table 2.5, sample 5-7) synthesized using different metal salt (PdCl<sub>2</sub>) concentration: (a, b) 0.05 mM, (c, d) 0.25 mM, (e, f) 0.5 mM, and (g) histogram showing PdNPs size distributions.

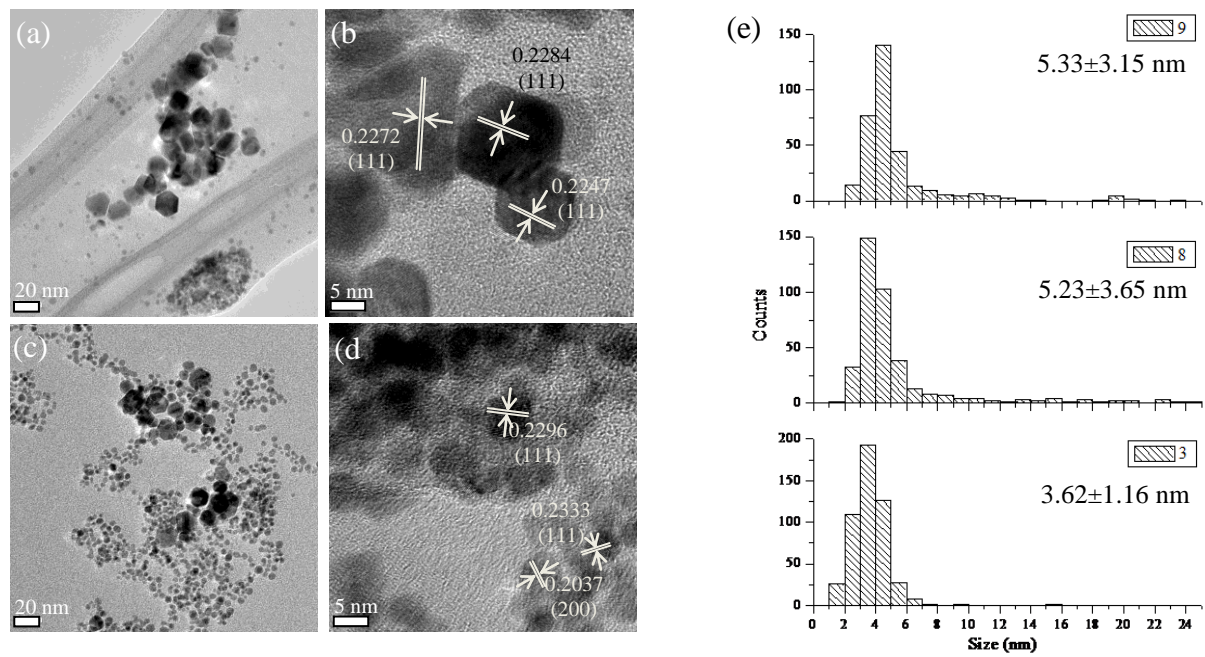


Figure 3.17 TEM images of PdNPs (table 2.5, sample 8-9) synthesized at different temperatures:  
(a, b) 125 °C, (c, d) 150 °C, and (e) histogram showing PdNPs size distributions.

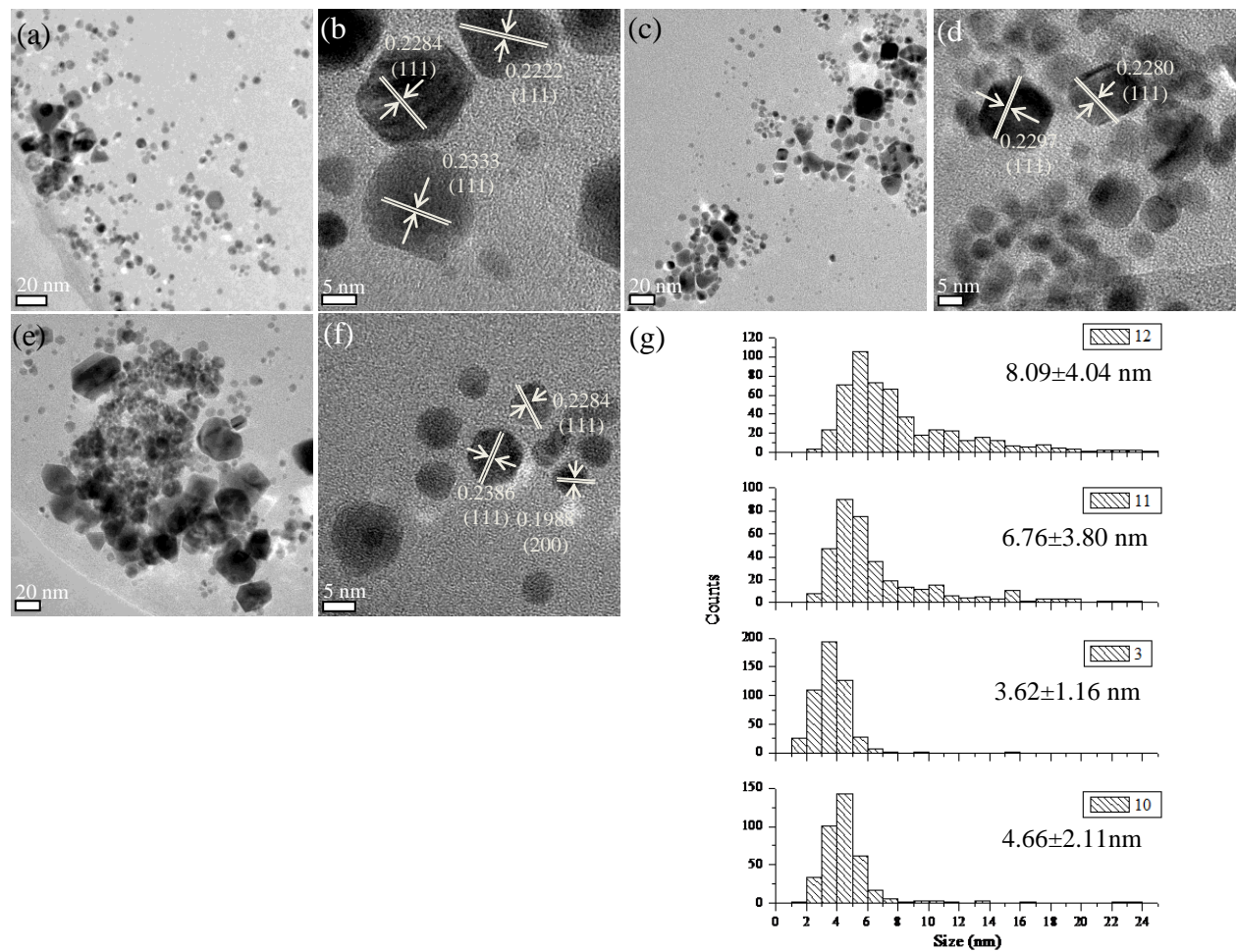


Figure 3.18 TEM images of PdNPs (table 2.5, sample 10-12) synthesized for different growth duration: (a, b) 1 h, (c, d) 6 h, (e, f) 10 h, and (g) histogram showing PdNPs size distributions.

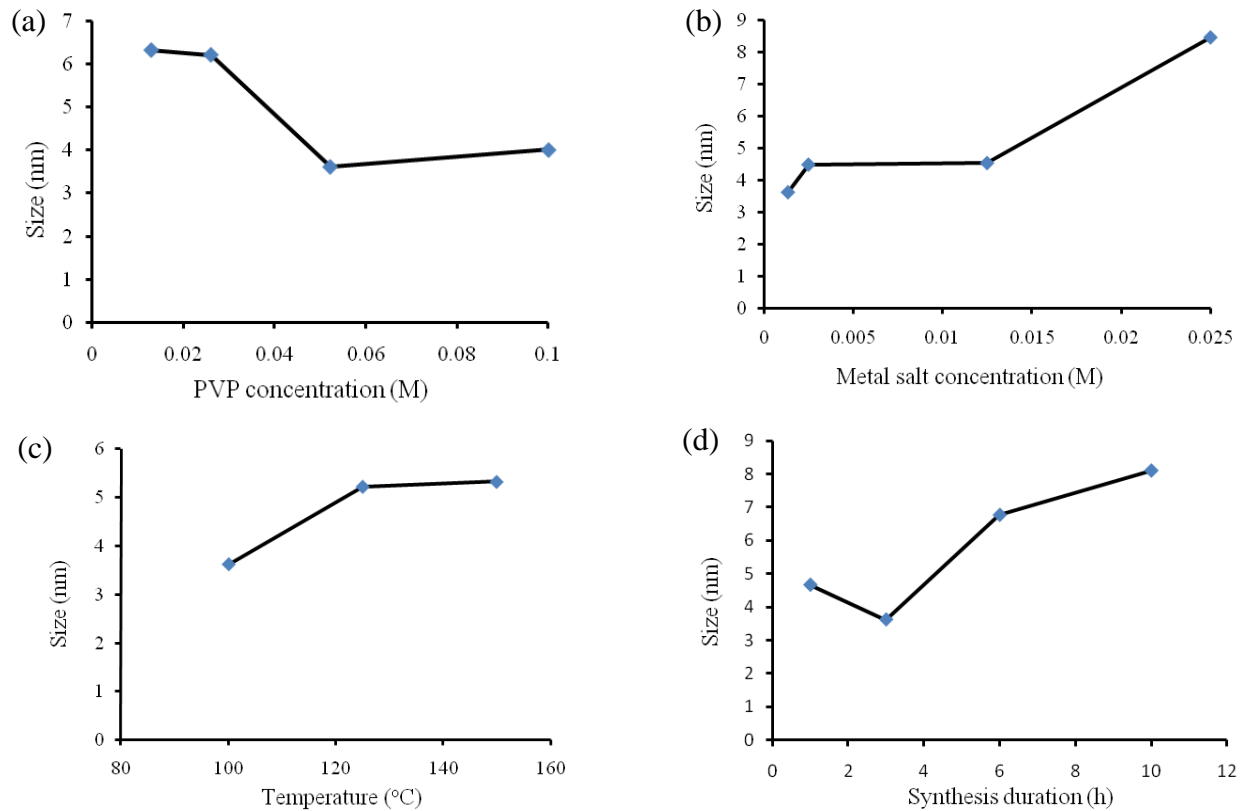


Figure 3.19 The change of PdNPs size with different parameters: (a) PVP concentration, (b) metal salt concentration, (c) temperature, (d) synthesis duration.

We also synthesized high yield palladium nanocubes based on the systematic study. The TEM images and size distribution histogram are shown in figure 3.20. Palladium is a widely used catalyst; among different shapes of palladium nanoparticles, palladium nanocubes have received significant attention because it was reported that palladium {100} facets have higher catalytic activity than {111},<sup>35</sup> and palladium cubes are enclosed by {100} facets. Shape control of palladium particles were obtained by adding halide species such as Br<sup>-</sup> and Cl<sup>-</sup> during the synthesis. First of all, Br<sup>-</sup> and Cl<sup>-</sup> have the affinity to bind {100} facets of palladium nanoparticles, which would help the formation of {100}. Secondly, in order to obtain uniform shapes, a moderate reducing rate is usually desired. Br<sup>-</sup> and Cl<sup>-</sup> ions can promote the formation of [PdBr<sub>4</sub>]<sup>2-</sup> and [PdCl<sub>4</sub>]<sup>2-</sup> complexes, thus can help us synthesis uniform nanocubes.

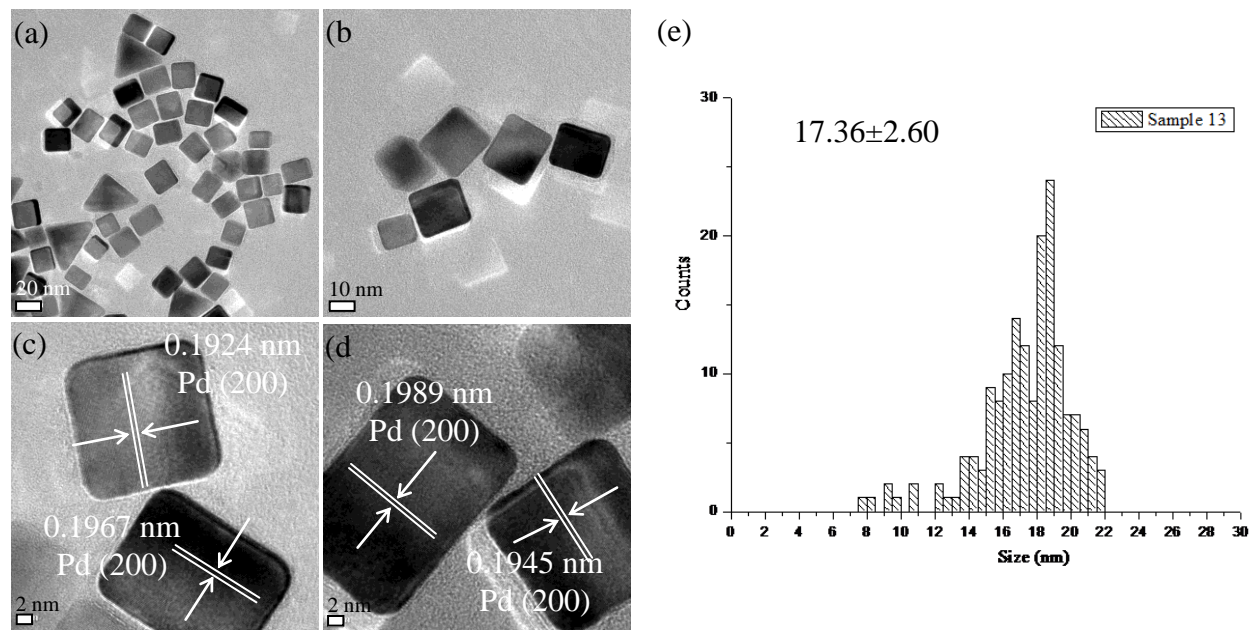


Figure 3.20 (a - d) TEM images of shape controlled PdNPs (table 2.5, sample 13), and (e) histogram showing PdNPs size distribution.

### *3.3 Synthesis and characterization of platinum nanoparticles*

In systematic study of platinum nanoparticles, metal salt concentration, PVP concentration, temperature, reducing agent, and synthesis duration were varied to observe the morphology change of platinum nanoparticles. Synthesis conditions are listed in table 2.6, and size, shape distribution and crystallinity for each sample are summarized in table 3.5. Figure 3.21 to figure 3.25 present TEM images and size distribution histograms for each sample.

Similar trends with Pd nanoparticles synthesis were obtained in the formation of platinum nanoparticles. Larger nanoparticles could be synthesized by increasing metal salt concentration, increasing temperature, or the decrease of stabilizer (PVP) amount. The mechanism has been demonstrated in systematic study of gold and palladium nanoparticles. Overall, we obtained small platinum nanoparticles with narrow size distribution. Ternaishi et al.<sup>119</sup> demonstrated that the small size and uniform size distribution is due to high nucleation rate. Also, in our observation, there is not much morphology change in each set. Especially, when the synthesis duration varies from 1 h to 24 h, average size just had a small fluctuation (from  $2.53 \pm 0.48$  to  $2.49 \pm 0.38$ ). However, by using strong reducing agent, we obtained large platinum nanoparticles with irregular shape, which is due to the violent reaction condition reduced the ability of PVP to stabilize platinum nanoparticles during the reaction and resulted the aggregation of nanoparticles. The changes of platinum nanoparticle size with each parameter were plotted in figure 3.26.

Another goal for systematic study is to control the shape of nanoparticles. Song et al.<sup>38</sup> demonstrated that silver ion can enhance the crystal growth rate along <100>. So silver nitrate was added to our system as shape-control additives (table 2.6, sample 13). In this approach, platinum nanoparticles with larger size ( $7.65 \pm 1.11$  nm) and distinguished shapes (triangle and octahedron) were successfully synthesized.

Table 3.5 Result summary for systematic study indicating average size, shape distribution, lattice spacing, and the corresponding planes for the as-prepared PtNPs according to the table 2.6

Sample number	Average size (nm)	Shape distribution	Lattice spacing (nm) and the corresponding plane
1	2.91±0.42	Spherical	0.2228±0.003 (111)
2	2.93±0.60	Spherical	0.1982±0.003 (200)
			0.2292±0.004 (111)
3	2.96±0.46	Spherical	0.1978 (200)
			0.2301±0.002 (111)
4	4.03±0.61	Spherical	0.2015 ±0.006 (200)
			0.229 (111)
5	3.07±0.36	Spherical	0.1980 (200)
			0.2280±0.004 (111)
6	2.45±0.39	Spherical	0.2331 (111)
7	1.78±0.33	Spherical	0.2546 {110}
			0.2419±0.004 (111)
8	3.12±0.40	Spherical	0.1950 (200)
			0.2247±0.005 (111)
9	6.47±3.51	Irregular	0.1980 (200)
			0.2286±0.003 (111)
10	2.53±0.48	Spherical	0.2285±0.003 (111)
11	2.77±0.39	Spherical	0.1971±0.001 (200)
			0.2287±0.003 (111)
12	2.49±0.38	Spherical	0.1963±0.002 (200)
			0.2227±0.003 (111)
13	7.65±1.11	Triangle and octahedron	0.222 (111)

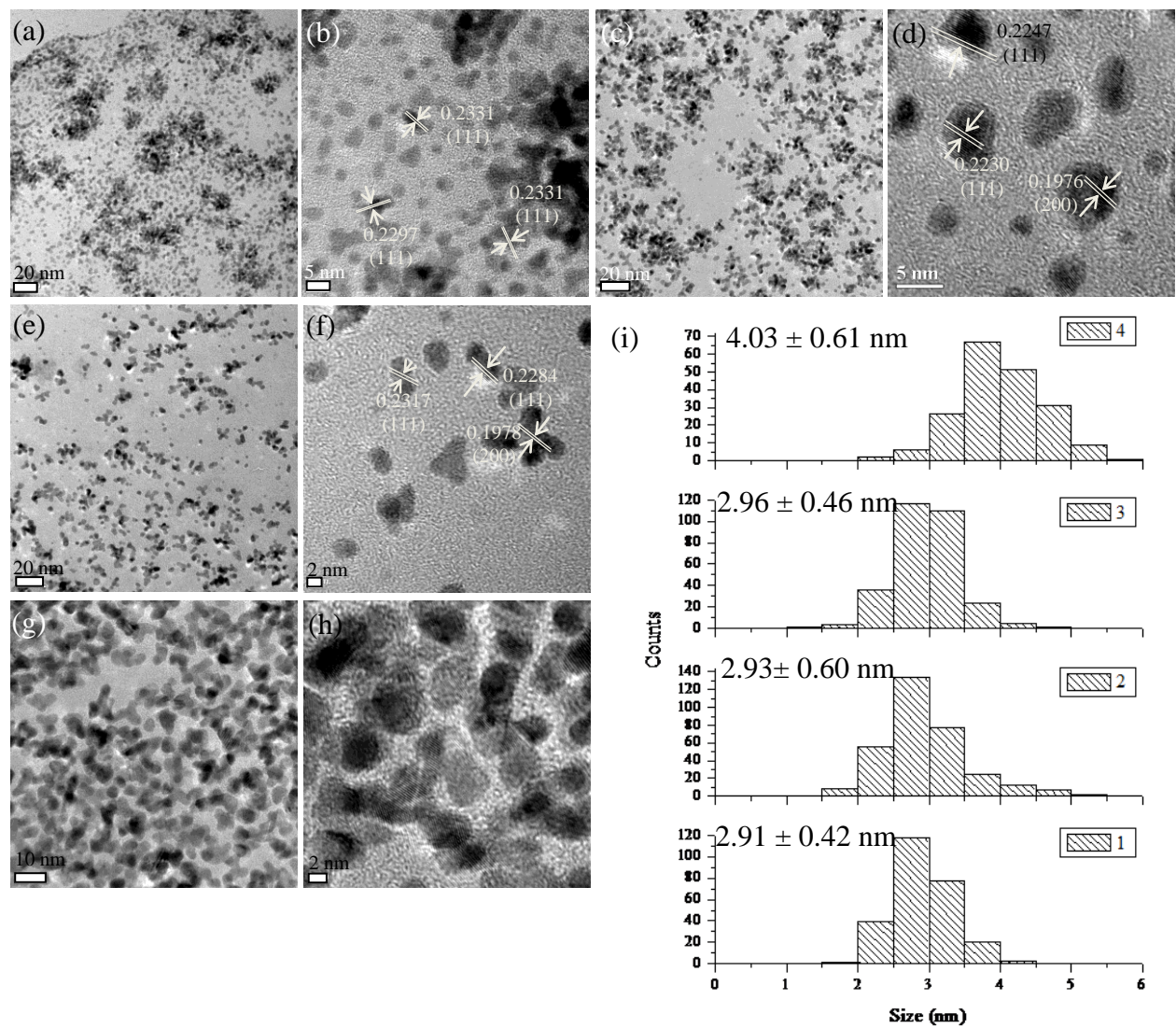


Figure 3.21 TEM images of PtNPs (table 2.6, sample 1-3) synthesized using different metal salt ( $\text{H}_2\text{PtCl}_6$ ) concentration: (a, b)  $1.93 \times 10^{-5}$  M, (c, d)  $6.0 \times 10^{-4}$  M, (e, f)  $1.93 \times 10^{-3}$  M, and (g) histogram showing PtNPs size distributions.

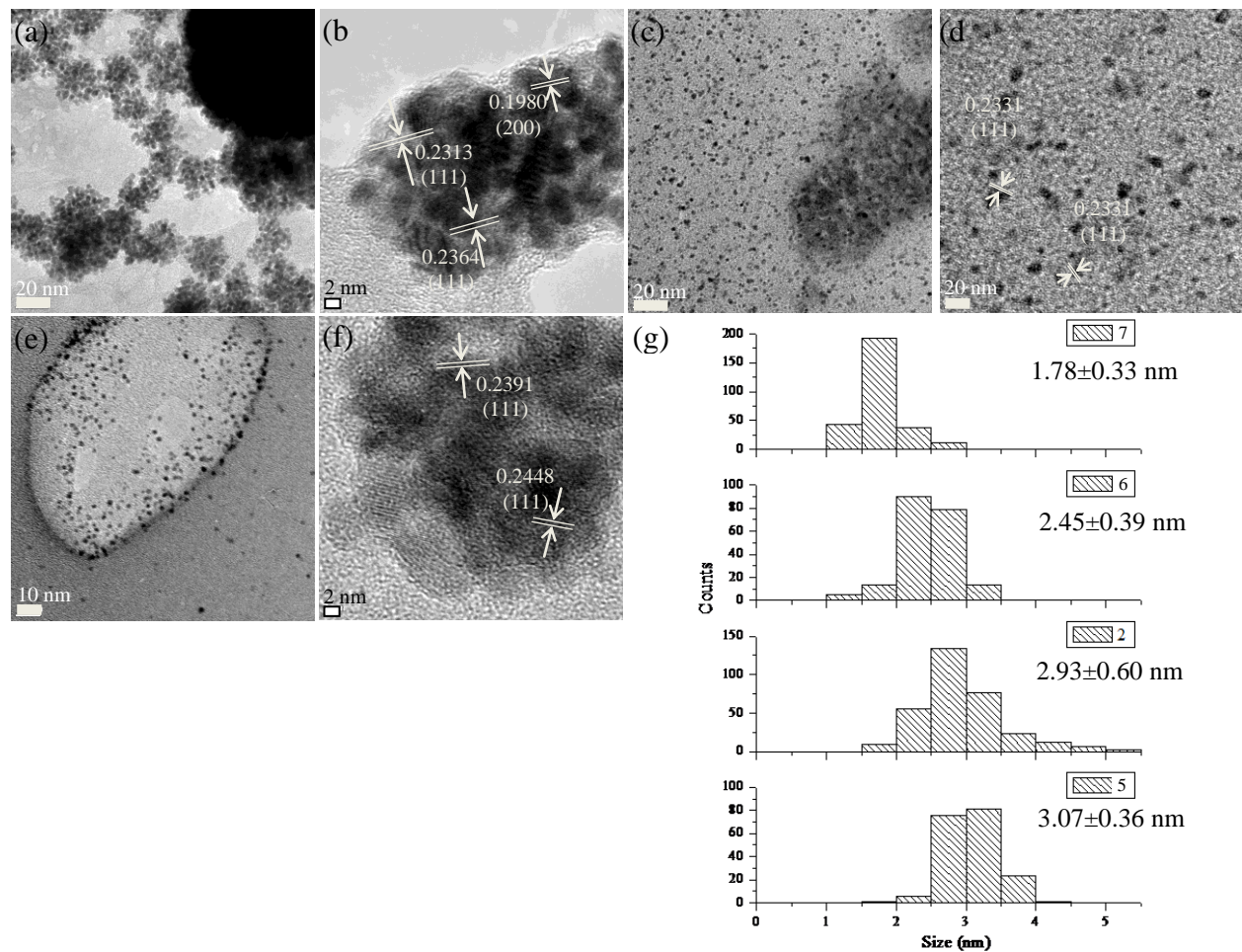


Figure 3.22 TEM images of PtNPs (table 2.6, sample 5-7) synthesized using different PVP amount: (a, b) 0 g, (c, d) 1.2 g, (e, f) 2 g, and (g) histogram showing PtNPs size distributions.

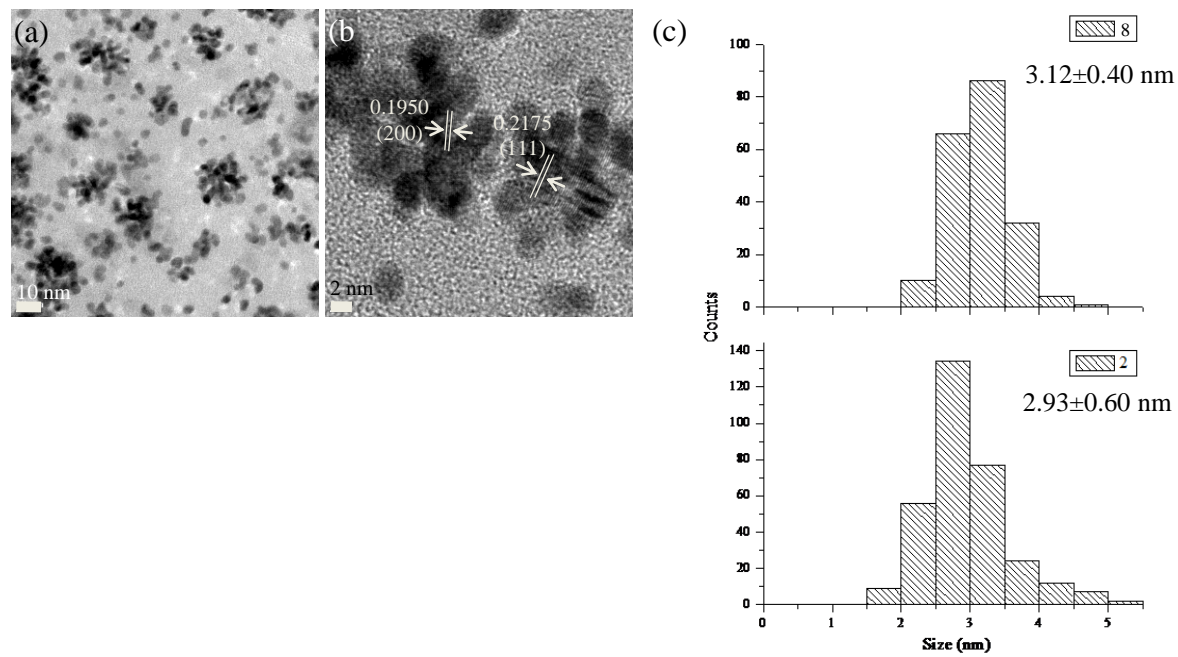


Figure 3.23 (a, b) TEM images of PtNPs (table 2.6, sample 8) synthesized at 150 °C, and (c) histogram showing PtNPs size distributions.

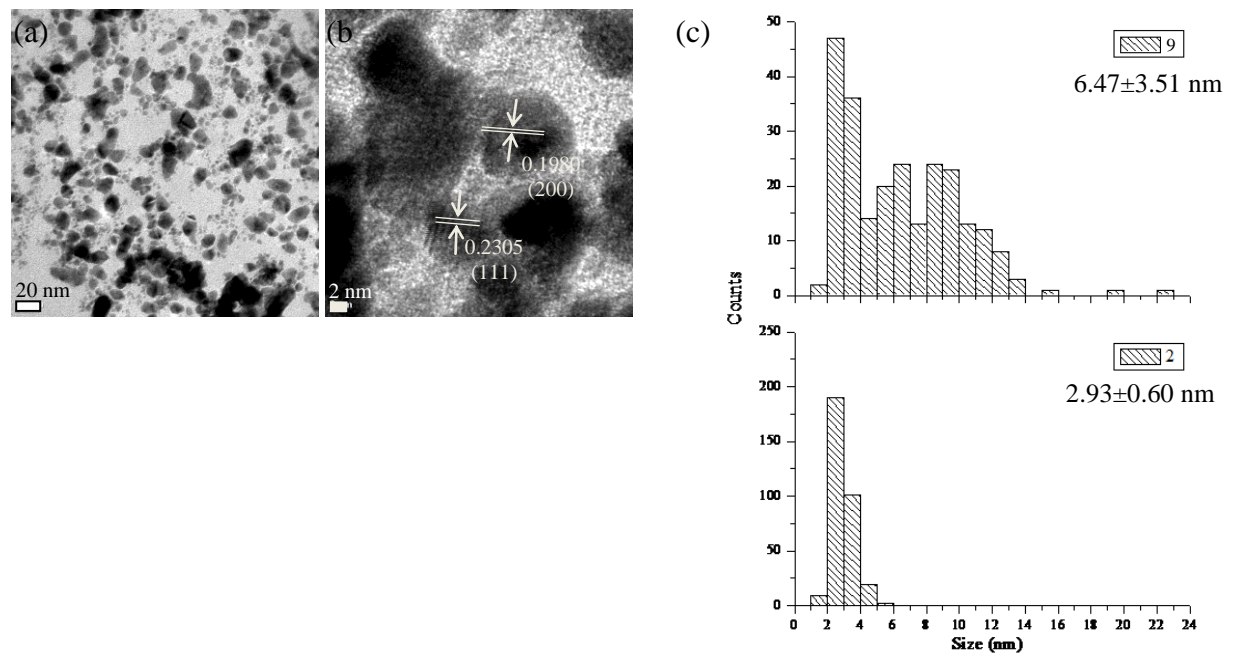


Figure 3.24 (a, b)TEM images of PtNPs (table 2.6, sample 9) synthesized using  $\text{NaBH}_4$  as reducing agent, and (c) histogram showing PtNPs size distributions.

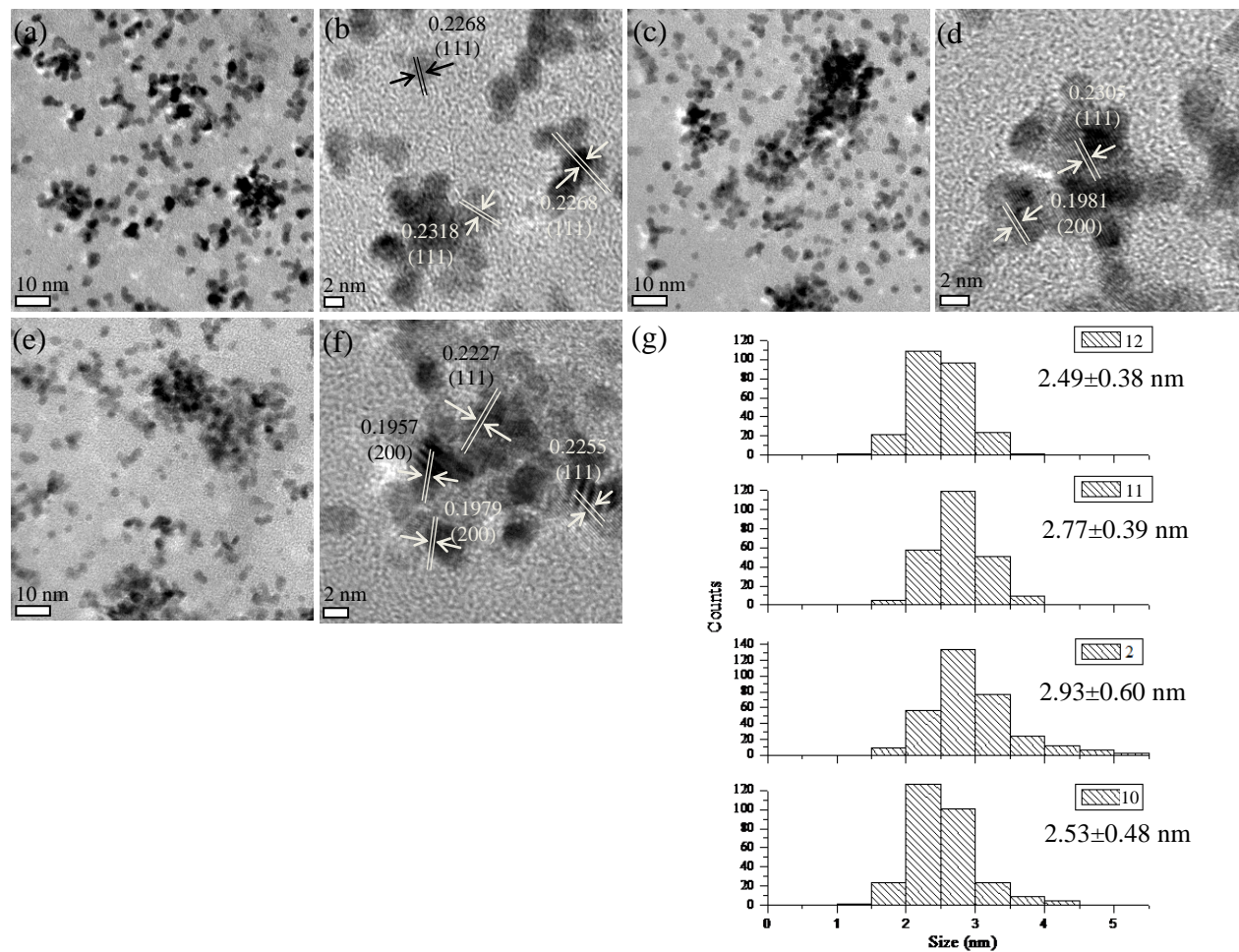


Figure 3.25 TEM images of PtNPs (table 2.6, sample 10-12) synthesized for different growth duration: (a, b) 1 h, (c, d) 10 h, (e, f) 24 h, and (g) histogram showing PtNPs size distributions.

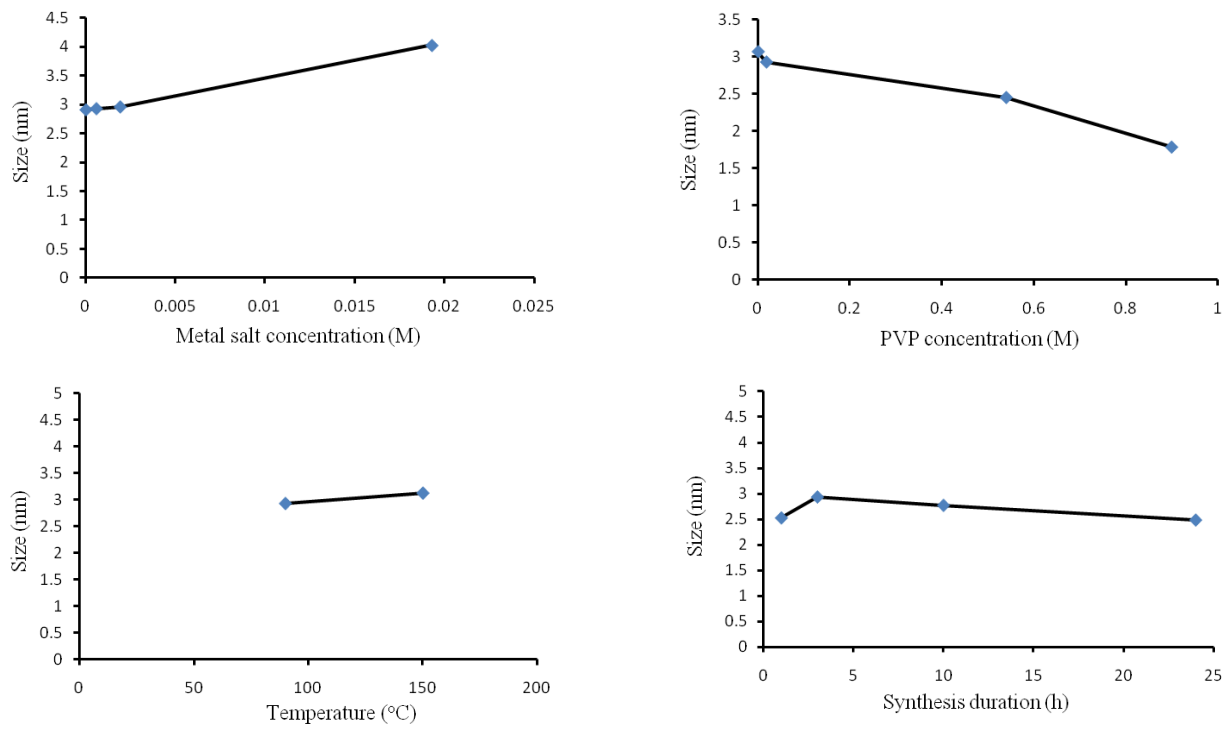


Figure 3.26 The change of PtNPs size with different parameters: (a) metal salt concentration, (b) PVP concentration, (c) temperature, (d) synthesis duration.

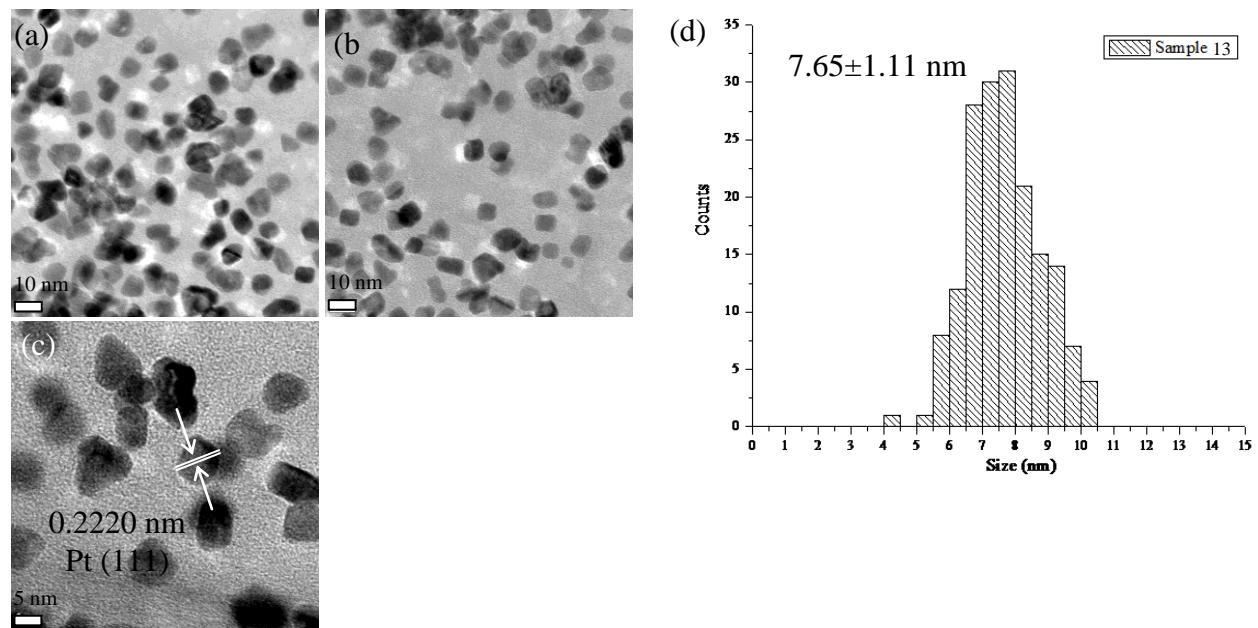


Figure 3.27 (a - c) TEM images of shape controlled PtNPs (table 2.6, sample 13), and (d) histogram showing PtNPs size distributions.

### *3.4 Plasma oxidation of noble metal nanoparticles*

The next step is the oxidization of noble metal nanoparticles. As demonstrated by Chopra et al.,<sup>102</sup> graphene shell can only be obtained on oxidized gold nanoparticles. The chemical state changes of gold, palladium and platinum is critical for understanding the oxidation behavior of noble metal nanoparticles, then help to further decide the oxidation condition for graphene growth step.

#### 3.4.1 Plasma oxidation duration study of gold nanoparticles

As a second step in this study, gold nanoparticles (table 2.1, sample 10) were selected for their plasma oxidation to result in gold oxide, which is critical for the growth of graphene shell in a chemical vapor deposition (CVD) process. X-ray photoelectron spectroscopy (XPS) was utilized to determine the formation of  $\text{AuO}_x$ . Figure 3.28 shows an overlapped XPS survey scans with binding energy ranging from 1000 to 0 eV and shows chemical composition of gold nanoparticles samples at various stages of plasma oxidation as a function of oxidation time. Different elements were detected: Au, Cl, N, Br, and B, which were from gold nanoparticles, unreacted  $\text{HAuCl}_4$ , CTAB, and  $\text{NaBH}_4$ , respectively. In addition, Si peak was also observed as the gold nanoparticles were drop-casted on silicon wafer. It could be observed that Si peaks increased in intensity as compared to non-plasma oxidized gold nanoparticles (Figure 3.28 a) and this could be attributed to removal of excessive surfactant (CTAB). The latter is removed as the plasma oxidation process is performed as proven by the fact that Br and N peaks disappeared beyond 15 min of plasma oxidation. The substrate is observed to be much clear but with certain extent of nanoparticle aggregation due to high energy plasma oxidation process.

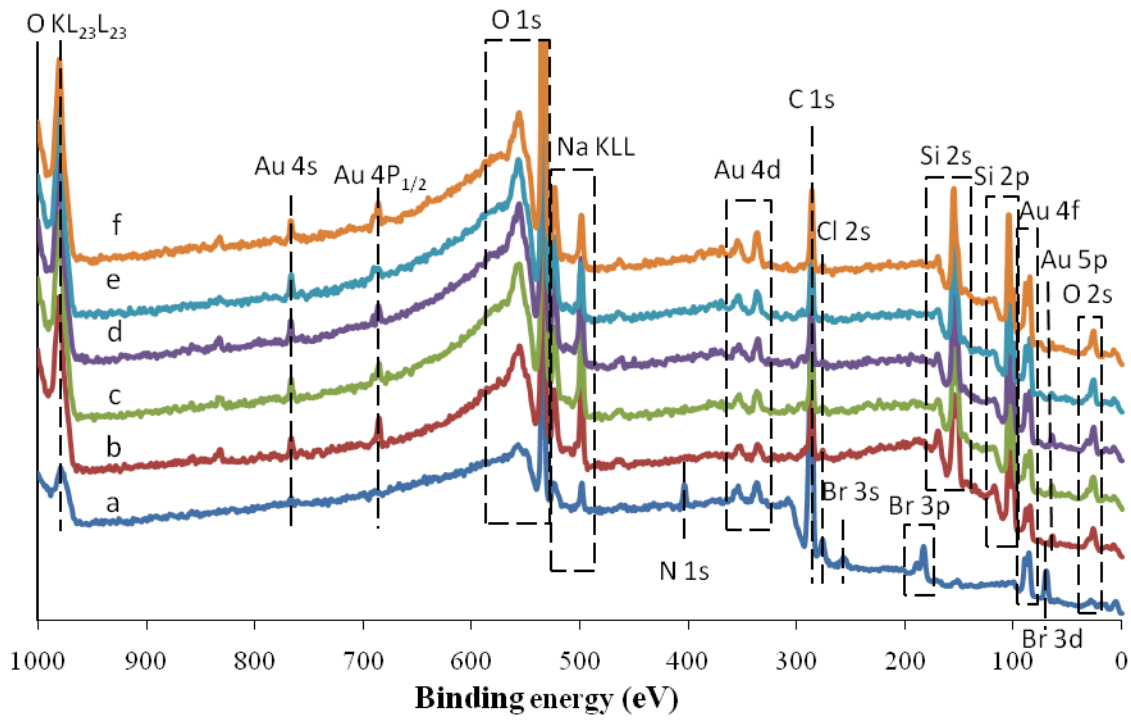


Figure 3.28 XPS spectra corresponding to AuNPs (a) before plasma oxidation and after (b) 15 min, (c) 30 min, (d) 45 min, (e) 60 min, (f) 75 min of plasma oxidation duration. Note: AuNPs (table 2.1, sample 10) were dispersed on Si wafer by drop casting method.

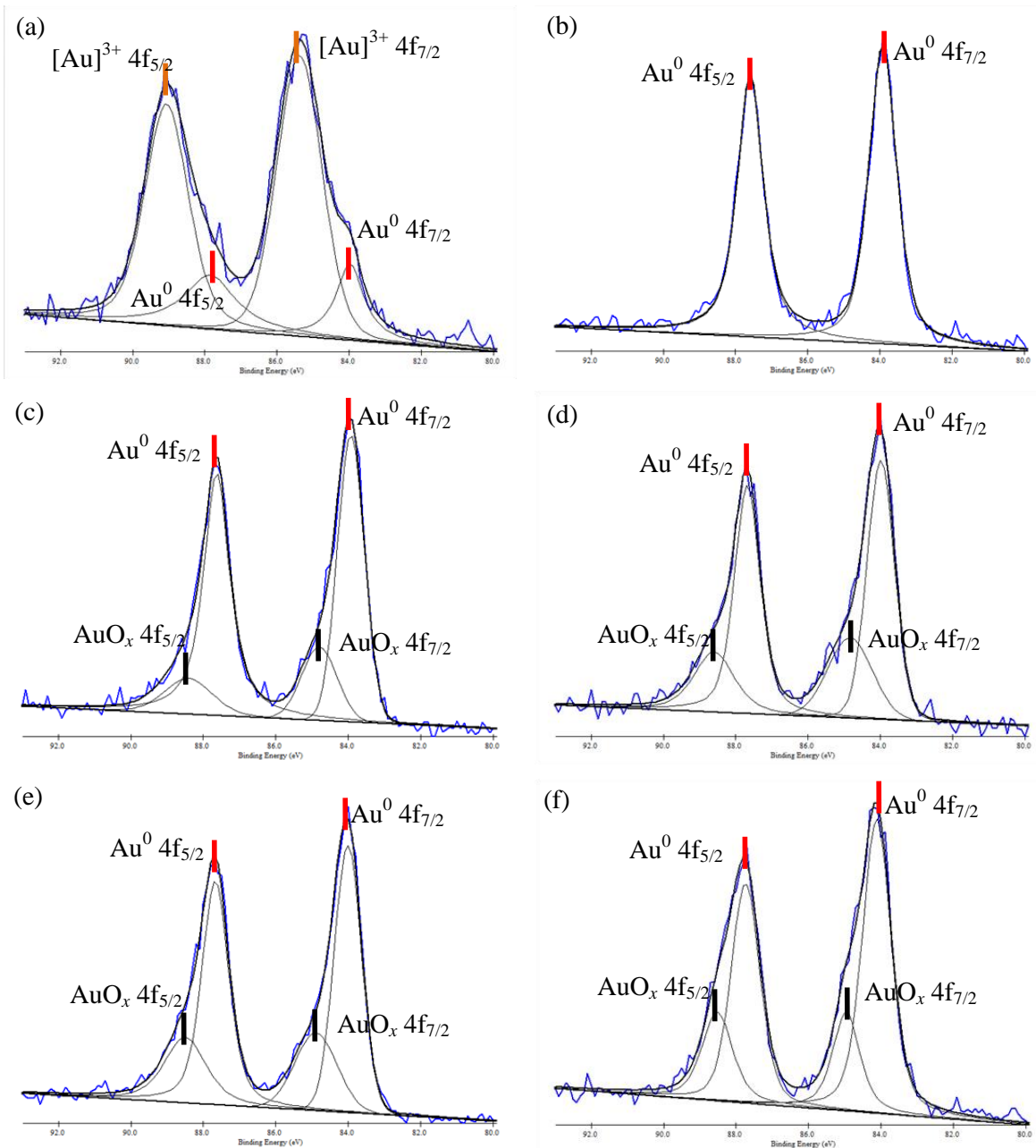


Figure 3.29 Deconvoluted XPS spectra (from figure 3.28), subtracted by linear background, and fitted with Au 4f peaks corresponding to AuNPs (a) before plasma oxidation and after (b) 15 min, (c) 30 min, (d) 45 min, (e) 60 min, (f) 75 min of plasma oxidation duration. Note: AuNPs (table 2.1, sample 10) were dispersed on unmodified Si wafer by drop casting method.

Table 3.6 Binding energy (eV) derived from XPS study for AuNPs (table 2.1, sample 10 with different plasma oxidation duration) corresponding to the spectra as shown in figure 3.29

Plasma duration (min)	Bind Energy (eV)					
	Au 4f <sub>5/2</sub>			Au 4f <sub>7/2</sub>		
	[Au <sup>3+</sup> ]	AuO <sub>x</sub>	Au <sup>0</sup>	[Au <sup>3+</sup> ]	AuO <sub>x</sub>	Au <sup>0</sup>
0	89.06	/	87.85	85.38	/	83.98
15	/	/	87.59	/	/	83.92
30	/	88.41	87.63	/	84.8	83.93
45	/	88.6	87.68	/	84.84	83.99
60	/	88.5	87.67	/	84.89	84.01
75	/	88.52	87.74	/	84.96	84.12

In regard to O peaks, apart from gold oxide, there could be several origins of this peak such as absorbed organic molecules, surface SiO<sub>2</sub> from substrate, presence of BO<sub>2</sub><sup>-</sup> due to reaction of NaBH<sub>4</sub>. So the formation of gold oxide could only be detected by detailed analysis of gold XPS. Figure 3.29 presents detailed deconvolution of Au 4f peaks.

The peaks observed in figure 3.29 (a) at 89.06 eV and 85.38 eV were assigned to Au<sup>3+</sup> in HAuCl<sub>4</sub> and is due to the presence of unreacted metal salt.<sup>120</sup> This can be further supported by the disappearance of Cl peak after plasma oxidation process beyond 15 min because of the decomposition of the metal salt to metal nanoparticles. Pure element Au peaks consistent with Au 4f<sub>7/2</sub> and Au 4f<sub>5/2</sub> were observed at ~ 83.9 eV and 87.5 eV, respectively, irrespective of plasma oxidation process.<sup>83</sup> As the plasma oxidation process was performed for different durations (15 – 75 min), two new peaks corresponding to AuO<sub>x</sub> at ~ 84.80 eV and 88.50 eV emerged (table 3.6). These peaks correspond to the chemical shift of Au 4f levels that have been strong indicators of gold oxide. This confirmed the presence of gold oxide shell with gold nanoparticle core. Oxidation behavior of gold nanoparticles was further estimated as shown in figure 3.30. This clearly shows the formation of gold oxide with the disappearance of metal salt and reduction in percentage of pure gold component. Overall, it was observed that about 31% gold oxide was formed as the plasma oxidation process was continued to 45 min. Further oxidation did not result more formation of gold oxide and there was even a slight decrease of gold oxide percentage after plasma 75 min. This may due to the decomposition of gold oxide under high temperature after lasting plasma oxidation. The XPS data presented in this study is important for understanding plasma-based oxidation behavior of gold nanoparticles and the role of excessive metal salt that was utilized as a precursor for gold nanoparticles formation.

Table 3.7 The ratio of AuO<sub>x</sub> calculated as peak area of AuO<sub>x</sub> over the sum of Au and AuO<sub>x</sub> peaks area as shown as figure 3.29

Plasma time (min)	HAuCl <sub>4</sub>	Au peaks	AuO <sub>x</sub> peaks	Oxidized Ratio (%)
	peaks area	area	area	(AuO <sub>x</sub> / (Au+ AuO <sub>x</sub> ) ×100%)
0	3284.33	972.97	0	0
15	0	3654.04	0	0
30	0	2722.95	733.29	21.22
45	0	2301.00	1035.82	31.04
60	0	4161.10	1892.08	31.26
75	0	2758.28	1081.19	28.16

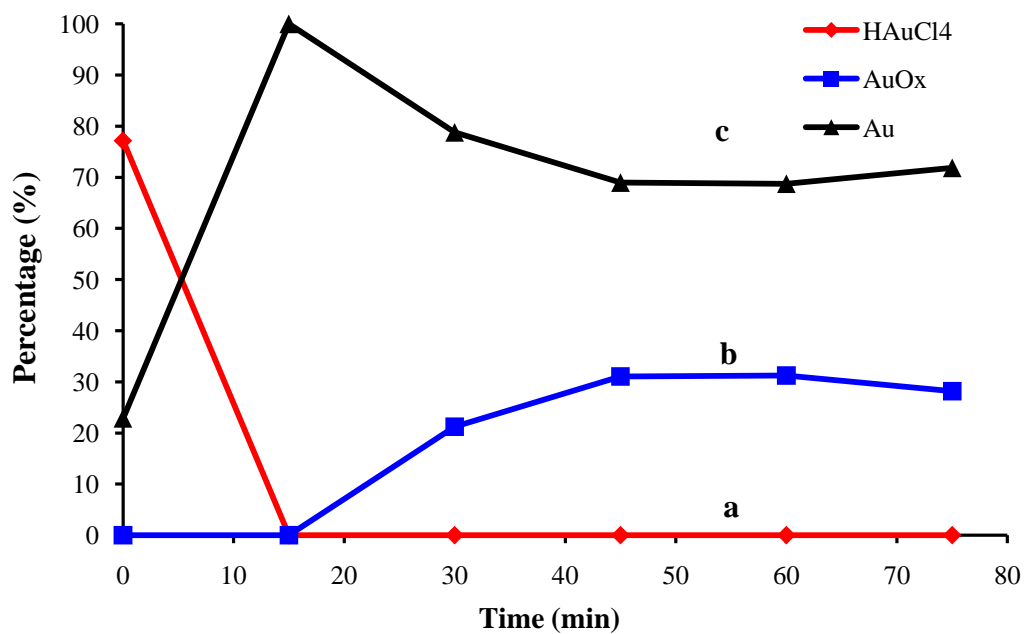


Figure 3.30 Oxidation behaviors of AuNPs (table 2.1, sample 10) as a function of plasma duration, percentages of (a) HAuCl<sub>4</sub>, (b) AuO<sub>x</sub>, (c) Au corresponding to the calculation in table 3.7

SEM was invested to study the surface migration of gold nanoparticles under plasma oxidation for different duration; the results are shown in figure 3.31. It was observed in figure 3.31 (a) that as-prepared gold nanoparticles are constructed by different crystal facets, and the topography can be distinguished from the contrast of SEM. After plasma for 15 min, sharp edge disappeared, the surface of gold nanoparticles became rough, which suggests a melting process during plasma oxidation. Despite the fact that bulk gold is inert as its melting point as high as about 1060 °C, gold nanoparticles have much lower melting point.<sup>121</sup> So, it is possible that gold nanoparticles undergo surface migration during plasma oxidation. We also observed that adjacent nanoparticles would stick to each other after 15 min oxidation, and the aggregation would increase in longer plasma duration, indicated from figure 3.31 (b) to (f).

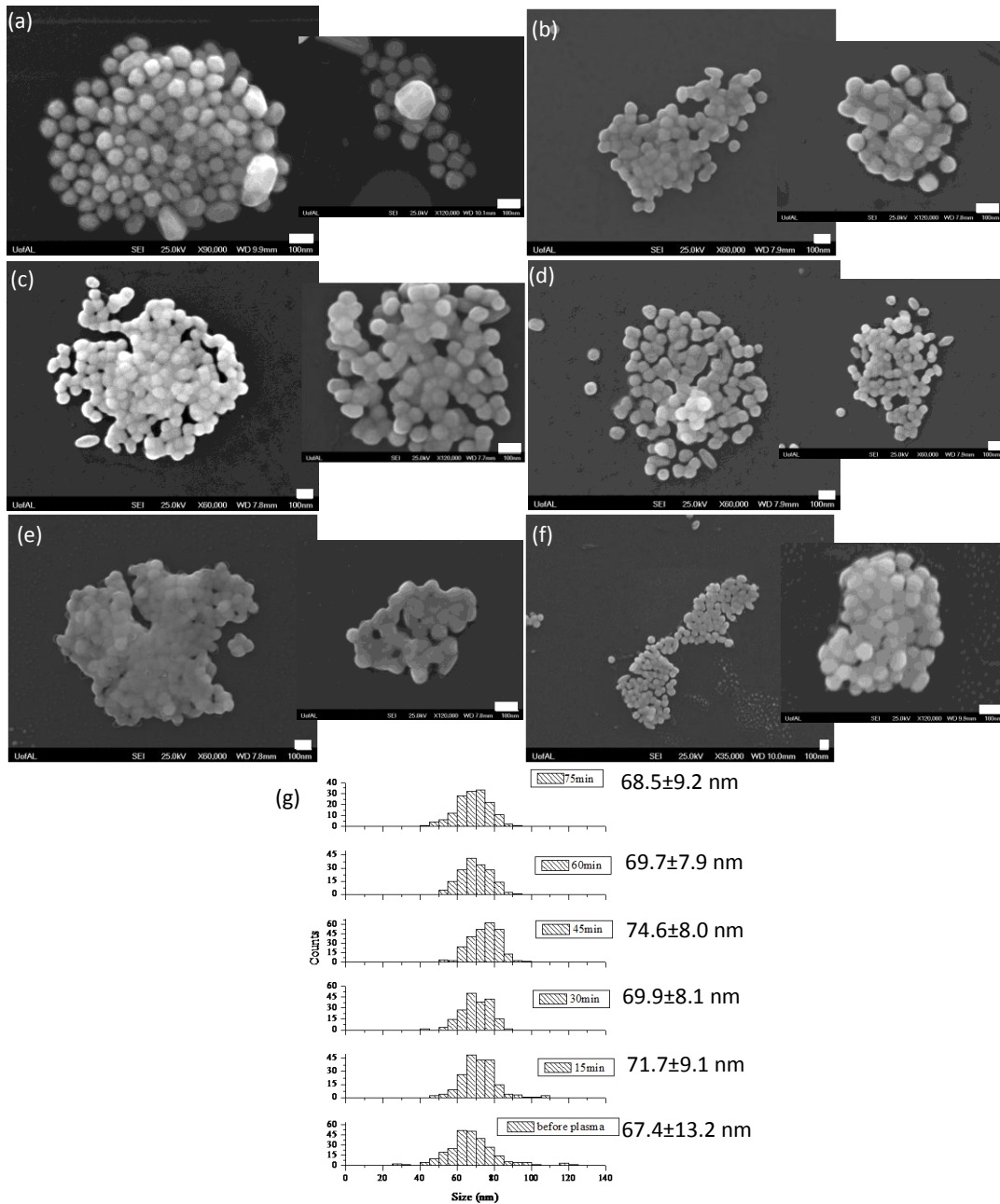


Figure 3.31 SEM images of AuNPs (table 2.1, sample 10) (a) before plasma oxidation and after plasma oxidation for b) 15 min, c) 30 min, d) 45 min, e) 60 min, and f) 75 min. And (g) histogram shows size distributions of gold nanoparticles. Note: AuNPs were dispersed on unmodified Si wafer by drop casting method. All scale bar stands for 100 nm.

### 3.4.2 Plasma oxidation of palladium nanoparticles

As synthesized palladium nanoparticles (table 2.5, sample 13) were selected for plasma oxidation duration study. XPS was utilized to determine formation of palladium oxide. Figure 3.32 shows an overlapped XPS survey scans with binding energy ranging from 1000 to 0 eV and shows chemical composition of palladium nanoparticles at various stages of plasma oxidation as a function of oxidation duration. Elements Pd, Na, C, and Si presented in spectra were from palladium nanoparticles, metal salt, PVP, and silicon substrate, respectively. In regard to O peaks, apart from palladium oxide, the absorbed organic molecules and surface  $\text{SiO}_2$  from substrate can also attribute to peak intensity. Thus the formation of palladium oxide could only be detected by detailed analysis of Pd XPS peaks. Figure 3.33 shows detailed deconvolution of Pd 3d peaks.

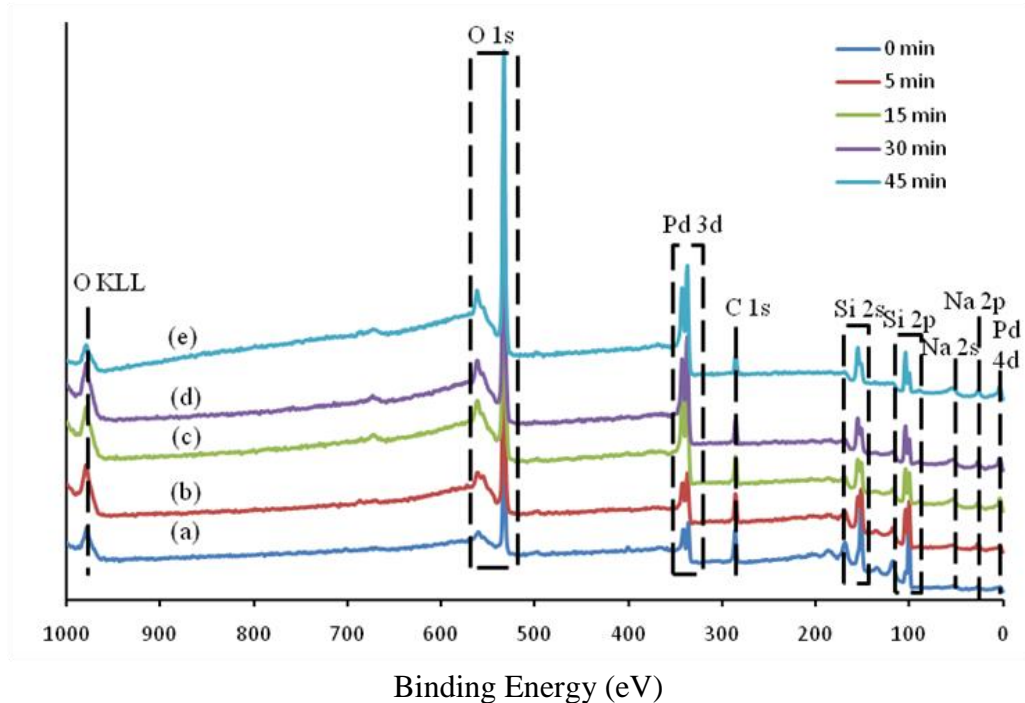


Figure 3.32 XPS spectra corresponding to PdNPs (a) before plasma oxidation and after (b) 5 min, (c) 15 min, (d) 30 min, (e) 45 min of plasma oxidation duration. Note: Shape controlled PdNPs (table 2.5, sample 13) were dispersed on Si wafer by drop casting method.

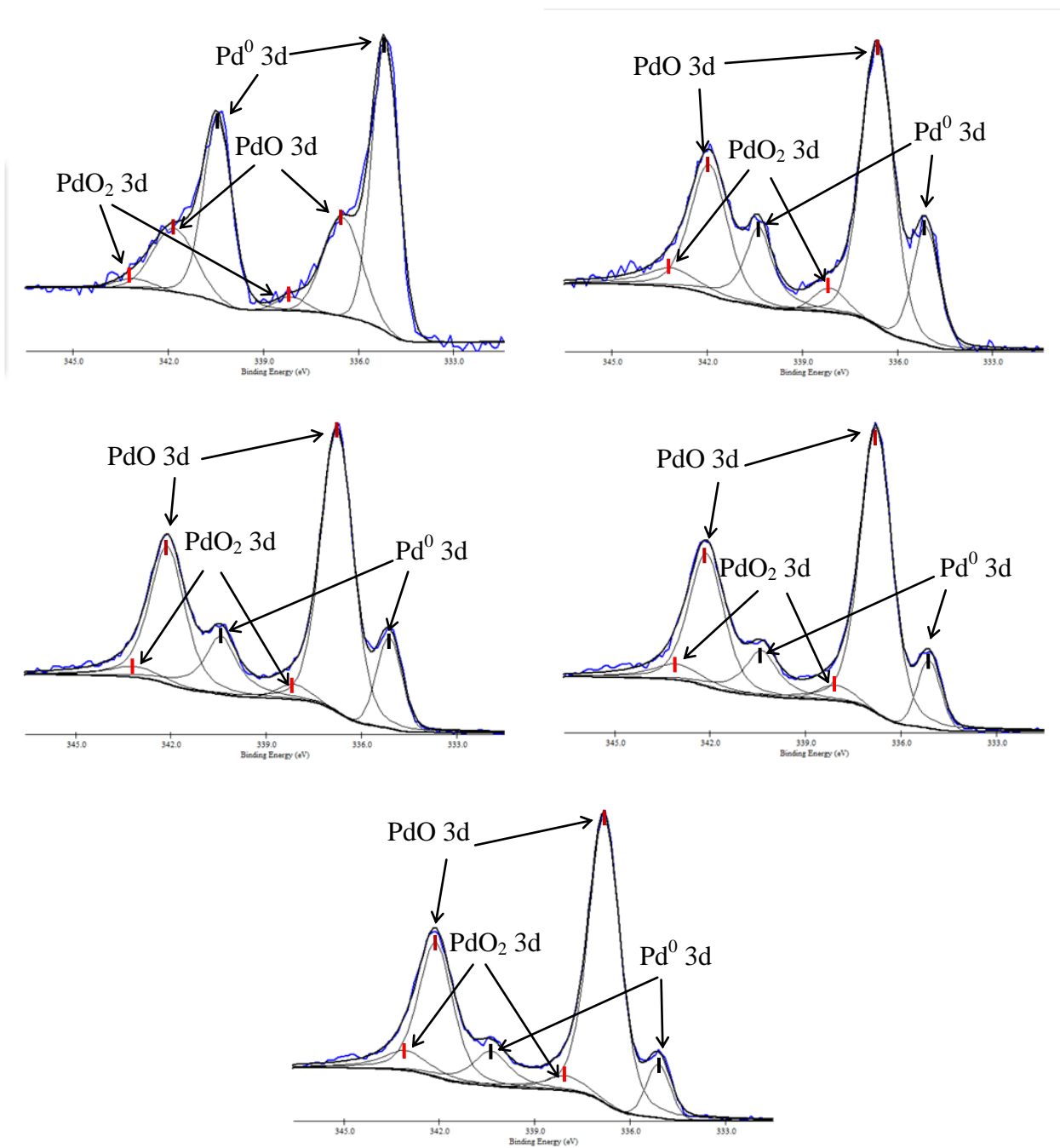


Figure 3.33 Deconvoluted XPS spectra (from figure 3.32), subtracted by Shirley background, and fitted with Pd 3d peaks corresponding to PdNPs (a) before plasma oxidation and after (b) 5 min, (c) 15 min, (d) 30 min, (e) 45 min of plasma oxidation duration. Note: Shape controlled PdNPs (table 2.5, sample 13) were dispersed on Si wafer by drop casting method

Table 3.8 Binding energy (eV) derived from XPS study for shape controlled PdNPs with different plasma oxidation duration corresponding to the spectra as shown in figure 3.33.

Plasma		Bind Energy (eV)					
duration (min)		Pd 3d <sub>3/2</sub>			Pd 3d <sub>5/2</sub>		
		PdO <sub>2</sub>	PdO	Pd <sup>0</sup>	PdO <sub>2</sub>	PdO	Pd <sup>0</sup>
0	343.09	341.81	340.44	338.12	336.50	335.16	
5	343.09	341.94	340.37	338.14	336.64	335.10	
15	343.16	342.11	340.42	338.14	336.76	335.12	
30	343.06	342.11	340.39	338.05	336.78	335.12	
45	343.06	342.11	340.37	338.06	336.81	335.11	

It was observed that as-prepared palladium nanoparticles are constituted major by element Pd (peaks consistent with Pd 3d<sub>5/2</sub> and 3d<sub>3/2</sub> were observed at ~335.16 eV and 340.44 eV, respectively), some PdO (peaks consistent with 3d<sub>5/2</sub> and 3d<sub>3/2</sub> were observed at 336.50 eV and 341.81 eV, respectively) and PdO<sub>2</sub> (peaks consistent with 3d<sub>5/2</sub> and 3d<sub>3/2</sub> were observed at 338.12 eV and 343.09 eV, respectively). The formation of palladium oxide before plasma was due to the high activity of palladium nanoparticles, especially on the cubic corners and high temperature (80 °C) for palladium nanoparticle synthesis. As the plasma oxidation process was performed for different durations (5 - 45 min), the peaks corresponding to palladium oxide increased constantly, indicates the formation of palladium oxide. Oxidation behavior of palladium nanoparticles was further estimated as shown in figure 3.34. Palladium nanoparticles were constantly oxidized by plasma, formed PdO and PdO<sub>2</sub>. Based on the constitution vs. time plots, it was observed that Pd nanoparticles can be efficiently oxidized in 5 min. In the product of oxidation, PdO was the major component, suggests that PdO is more stable in the oxidation product. Overall, it was observed that ~85.22% palladium oxide was formed as the plasma oxidation process was continued till 45 min. Comparing to the oxidation behavior of gold nanoparticles, palladium nanoparticles we used are much easier to be oxidized.

Table 3.9 The ratio of PdO<sub>x</sub> calculated as peak area of PdO<sub>x</sub> over the sum of Pd and PdO<sub>x</sub> peaks area as shown as figure 3.33.

Plasma time (min)	Pd peaks	PdO peaks	PdO <sub>2</sub> peaks	Oxidized Ratio (%)
	area	area	area	(PdO <sub>x</sub> / (Pd+ PdO <sub>x</sub> ) ×100%)
0	14921.18	7209.07	854.14	35.08
5	8092.54	19174.82	2742.53	73.03
15	15898.07	49369.34	4160.40	77.10
30	12049.58	49778.17	5559.61	82.12
45	10199.6	51773.81	7035.27	85.22

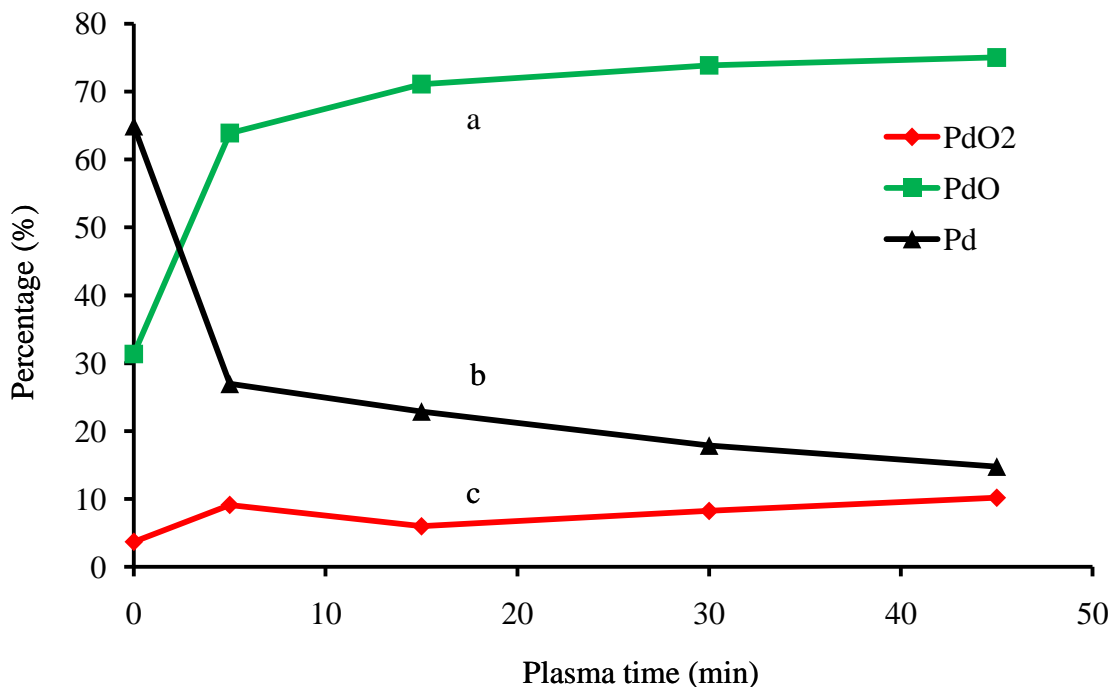


Figure 3.34 Oxidation behavior of shape controlled PdNPs as a function of plasma duration, percentages of (a) PdO, (b) Pd, and (c) PdO<sub>2</sub> corresponding to the calculation in table 3.9.

### 3.4.3 Plasma oxidation duration study of platinum nanoparticles

As synthesized platinum nanoparticles (table 2.6, sample 13) were selected for plasma oxidation duration study. XPS was utilized to determine formation of platinum oxide. Figure 3.35 shows an overlapped XPS survey scans with binding energy ranging from 1000 to 0 eV and shows chemical composition of platinum nanoparticles at various stages of plasma oxidation as a function of oxidation duration. Elements Pt, C, N, and Si presented in spectra were from platinum nanoparticles, PVP, and silicon substrate, respectively. The reduce of C peak and disappearance of N peak after oxidation suggests that excess surfactant PVP was removed by plasma and left some carbon residue. Also, the increase of Si peaks intensity as compared to Pt nanoparticles before plasma (Figure 3.35 a) indicates the removal of excess surfactant (PVP).

In regard to O peaks, apart from platinum oxide, the absorbed organic molecules and surface  $\text{SiO}_2$  from substrate can also constitute to peak intensity. Thus the formation of platinum oxide could only be detected by detailed analysis of Pt XPS peaks. Figure 3.36 present detailed deconvolution of Pt 4f peaks.

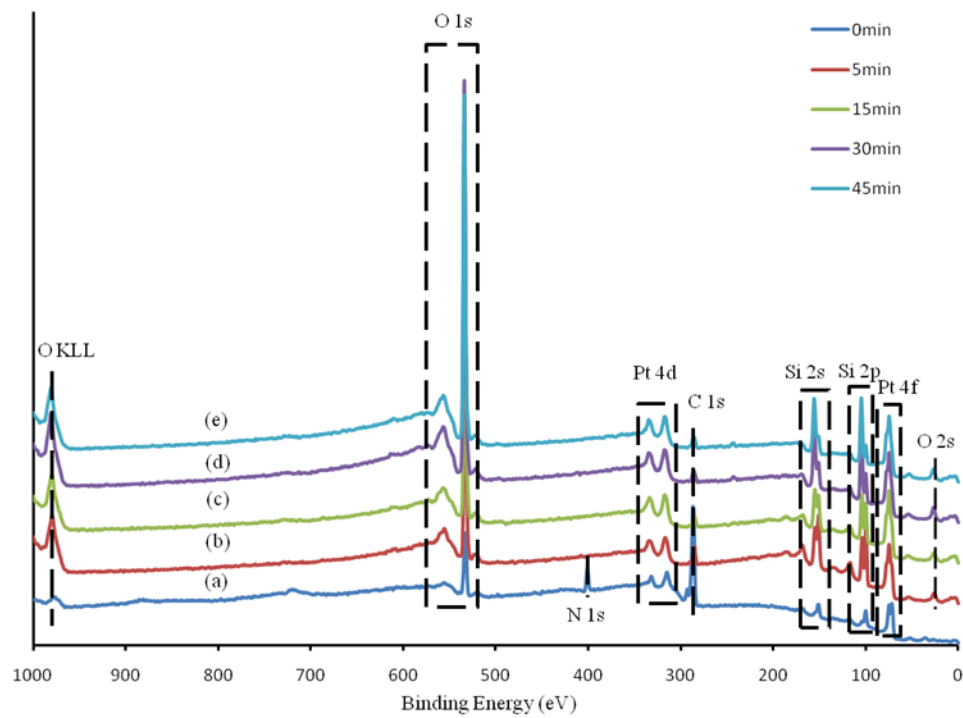


Figure 3.35 XPS spectra corresponding to PtNPs (a) before plasma oxidation and after (b) 5 min, (c) 15 min, (d) 30 min, (e) 45 min of plasma oxidation duration. Note: Shape controlled PtNPs (table 2.6, sample 13) were dispersed on Si wafer by drop casting method.

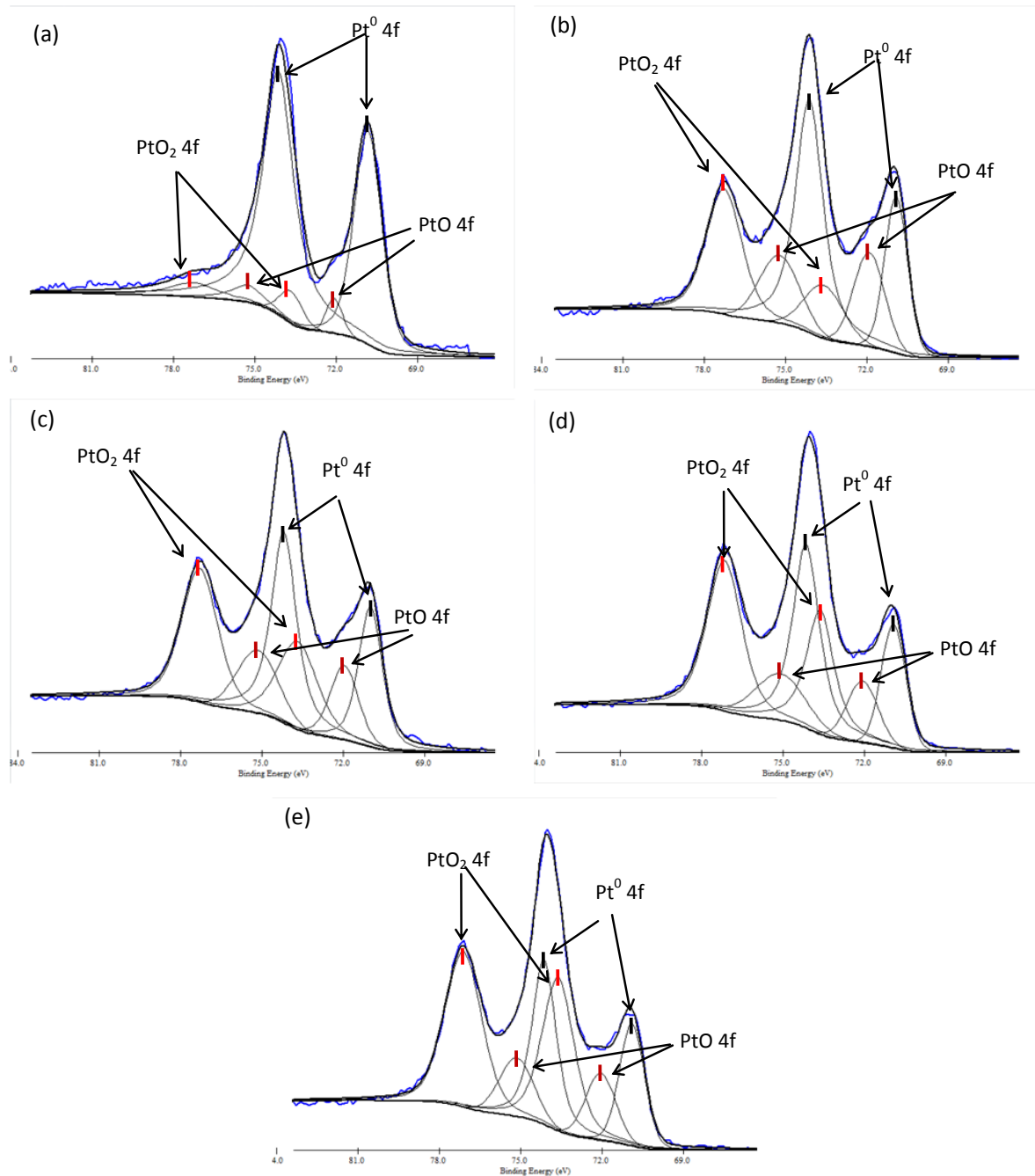


Figure 3.36 Deconvoluted XPS spectra (from figure 3.35), subtracted by Shirley background, and fitted with Pt 4f peaks corresponding to PtNPs (a) before plasma oxidation and after (b) 5 min, (c) 15 min, (d) 30 min, (e) 45 min of plasma oxidation duration. Note: Shape controlled PtNPs (table 2.6, sample 13) were dispersed on unmodified Si wafer by drop casting method.

Table 3.10 Binding energy (eV) derived from XPS study for shape controlled PtNPs with different plasma oxidation duration corresponding to the spectra as shown in figure 3.36.

Plasma		Bind Energy (eV)					
duration (min)		Pt 4f <sub>5/2</sub>			Pt 4f <sub>7/2</sub>		
		PtO <sub>2</sub>	PtO	Pt <sup>0</sup>	PtO <sub>2</sub>	PtO	Pt <sup>0</sup>
0		77.28	75.26	74.13	73.67	72.07	70.83
5		77.26	75.22	74.12	73.58	71.91	70.91
15		77.28	75.15	74.18	73.67	71.95	70.99
30		77.16	75.10	74.15	73.63	72.07	70.93
45		77.12	75.15	74.14	73.62	72.05	70.90

It was observed that as-prepared platinum nanoparticles were constituted major by element Pt (peaks consistent with  $\text{Pt } 4f_{7/2}$  and  $4f_{5/2}$  were observed at ~70.83 eV and 74.13 eV, respectively), a slight amount of PtO (peaks consistent with  $4f_{7/2}$  and  $4f_{5/2}$  were observed at 72.07 eV and 75.26 eV, respectively), and  $\text{PtO}_2$  (peaks consistent with  $4f_{7/2}$  and  $4f_{5/2}$  were observed at 73.67 eV and 77.28 eV, respectively). The formation of platinum oxide before plasma was due to the elevate temperature ( $200^{\circ}\text{C}$ ) for platinum nanoparticle synthesis. As the plasma oxidation process was performed for different durations (5 – 45 min), the peaks corresponding to platinum oxide increased constantly, indicates the formation of platinum oxide. Oxidation behavior of platinum nanoparticle was further estimated as shown in figure 3.37. Platinum nanoparticles were constantly oxidized by plasma, formed PtO and  $\text{PtO}_2$ . Based on the constitution vs. time plots, it was observed platinum nanoparticles can be efficiently oxidized in 5 min. In the product of oxidation, the percentage of PtO decreased after 5 min oxidation, while the percentage of  $\text{PtO}_2$  kept increasing. This suggested that  $\text{PtO}_2$  is more stable in the oxidation product, and the as-formed PtO may partially convert to  $\text{PtO}_2$  in longer plasma duration. Overall, it was observed that ~66.74% platinum oxide was formed as the plasma oxidation process was continued till 45 min. Comparing to the oxidation behavior of gold nanoparticles in our study, the platinum nanoparticles we used are much easier to be oxidized.

Table 3.11 The ratio of PtO<sub>x</sub> calculated as peak area of PtO<sub>x</sub> over the sum of Pt and PtO<sub>x</sub> peaks area as shown as figure 3.36.

Plasma time (min)	Pt peaks	PtO peaks	PtO <sub>2</sub> peaks	Oxidized Ratio (%)
	area	area	area	(PtO <sub>x</sub> / (Pt+ PtO <sub>x</sub> ) ×100%)
0	26243.57	2063.83	2618.2	15.14
5	23092.98	10633.11	13729.16	51.34
15	24189.9	11274.75	22197.85	58.05
30	22103.3	9995.2	24989.3	61.28
45	17627.07	8681.198	26685.97	66.74

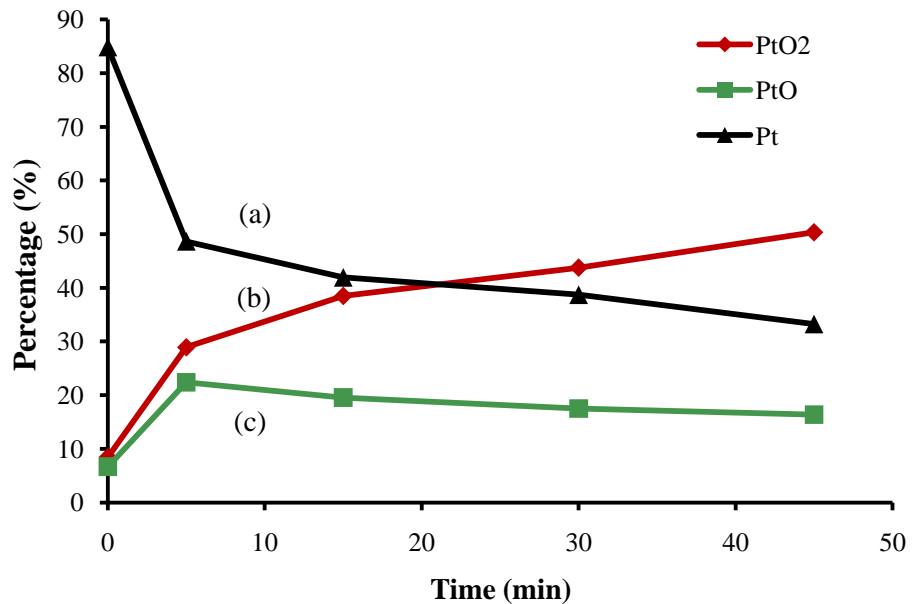


Figure 3.37 Oxidation behavior of shape controlled PtNPs (table 2.6, sample 13) as a function of plasma duration, percentages of (a) Pt, (b) PtO<sub>2</sub>, and (c) PtO corresponding to the calculation in table 3.11.

The thickness of oxide shell of noble metal nanoparticles was also analyzed. For the XPS analysis, the analyzing depth (H) is at 1~10 nm. The average diameter of as-prepared noble metal nanoparticles can be calculated from TEM images, and the ratio of metallic metal and oxidized metal at room temperature could be calculated from XPS. Thus, it is possible to calculate the thickness of oxide shell at different plasma oxidation point. Since the volume for a spherical cap ( $V_{cap}$ ) could be calculated using (schematic is shown in figure 3.38 a):

$$V_{cap} = \frac{\pi}{3} H^2 (3R - H)$$

Set H is 8 nm. If the percentage of metallic gold calculated from XPS is Au%, then,

$$\frac{\frac{\pi}{3}(H-a)^2(3r_1-H+a)}{\frac{\pi}{3}H^2(3R-H)} = Au\% \quad (1)$$

$$\frac{\frac{4\pi}{3}R^3 - \frac{4\pi}{3}r_1^3)\rho_{Au}}{M_{Au}} = n_{(Au \text{ been oxidized })} \quad (2)$$

$$V_{Au_2O_3} = 0.5n_{(Au \text{ been oxidized })}M_{Au_2O_3}/\rho_{Au_2O_3} \quad (3)$$

$$\frac{4\pi}{3}(r_1 + a)^3 = \frac{4\pi}{3}(r_1)^3 + V_{Au_2O_3} \quad (4)$$

Where R is the radius of nanoparticles before oxidation,  $a$  is the thickness of oxide shell,  $r_1$  is the radius of remained metallic nanoparticles.  $\rho_{Au}$ ,  $\rho_{Au_2O_3}$  are the density of gold and gold oxide,  $M_{Au}$ ,  $M_{Au_2O_3}$  are the molecular weight of gold and gold oxide.  $V_{Au_2O_3}$  is the volume of gold oxide. The average size of gold nanoparticles before oxidation is 23.28 nm.

The system of equations can also been used to estimate the thickness of oxide shell for palladium and platinum. The average size of palladium and platinum nanoparticles used for plasma oxidation is 17.36 nm and 7.65 nm. So for platinum nanoparticles, H=7.65 nm. By submitting the percentage of metallic state metal calculated from XPS results, the oxide shell thickness on nanoparticles vs. different oxidation time can be estimated, which are shown in figure 3.38 (b-d).

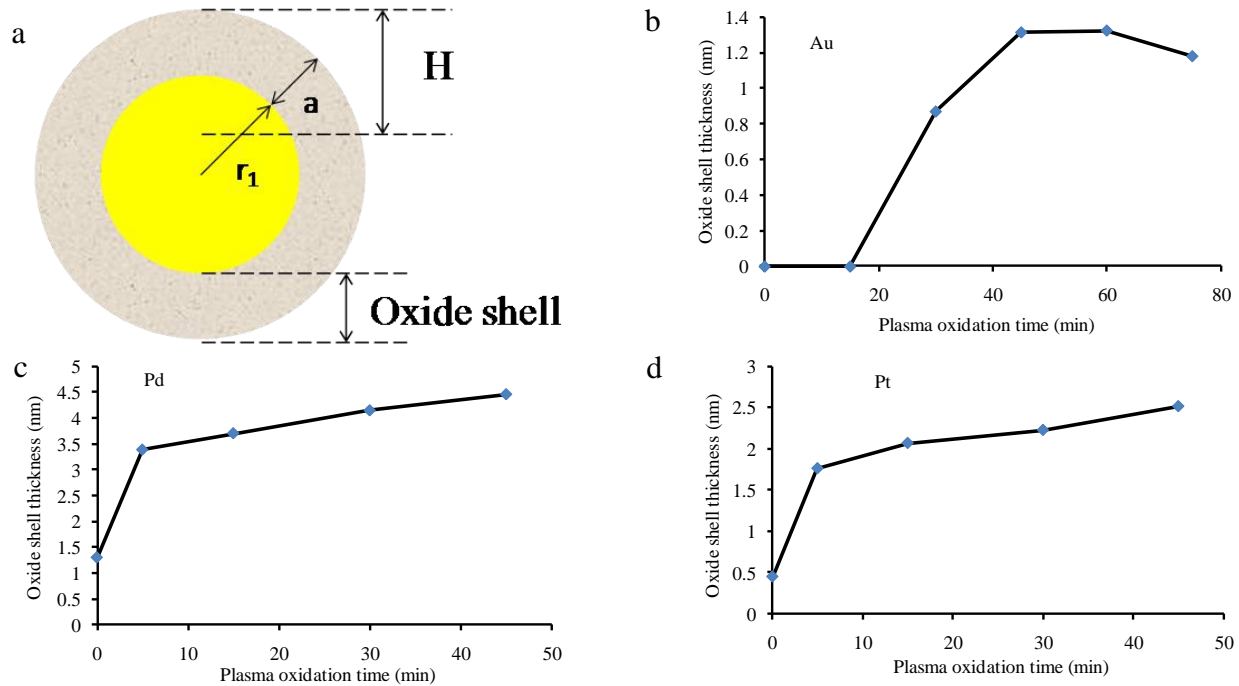


Figure 3.38 (a) Schematic for the gold nanoparticles been oxidized, and thickness of oxide shell vs. plasma oxidation time for (b) AuNPs, (c) PdNPs, and (d) PtNPs.

### *3.5 Fabrication of graphene encapsulated noble metal nanoparticles*

The growth and plasma oxidation study of noble metal nanoparticles is of critical importance for the step of graphene growth in a CVD process.<sup>102</sup> Towards this end, gold nanoparticles (table 2.1, sample 10), palladium nanoparticles (table 2.5, sample 13), and platinum nanoparticles (table 2.6, sample 13) were grown under conditions that resulted in different shapes and sizes. They were drop-casted on a silicon substrate and plasma oxidized for 30 min. The duration was selected based on XPS results and facilitates complete elimination of metal salt as well as excessive surfactant.

Based on the observation of Chopra et al.<sup>102</sup>, most important to the graphene shell growth on gold nanoparticles is the presence of oxidized gold nanoparticles, which is also achieved by the plasma oxidation step. It has been hypothesized that presence of gold oxide is critical for the graphene growth because the former is highly unstable at high temperatures. Thus, graphene growth that occurs at 675 °C will lead to reduction of gold oxide into gold and meanwhile accept electrons from the incoming carbon feed, finally will result in the formation of graphene shell encapsulate gold nanoparticles. Same mechanism is expected for palladium and platinum nanoparticles, thus all nanoparticles were plasma oxidized before graphene growth.

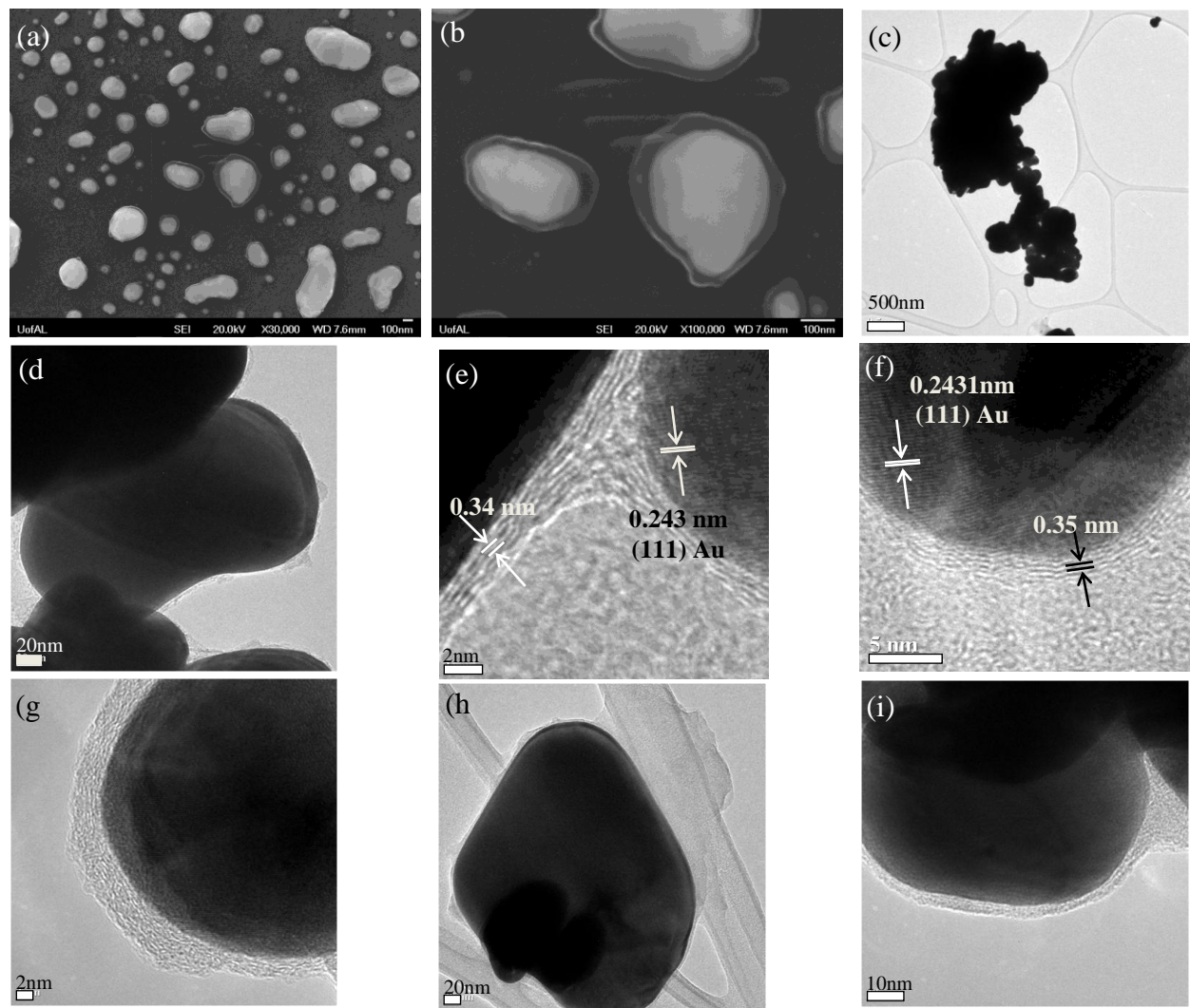


Figure 3.39 (a, b) SEM images and (c - i) TEM images of graphene encapsulated AuNPs on Si wafer. Note: AuNPs (table 2.1, sample 10) were dispersed on unmodified Si wafer by drop-casting method and utilized to grow graphene shells.

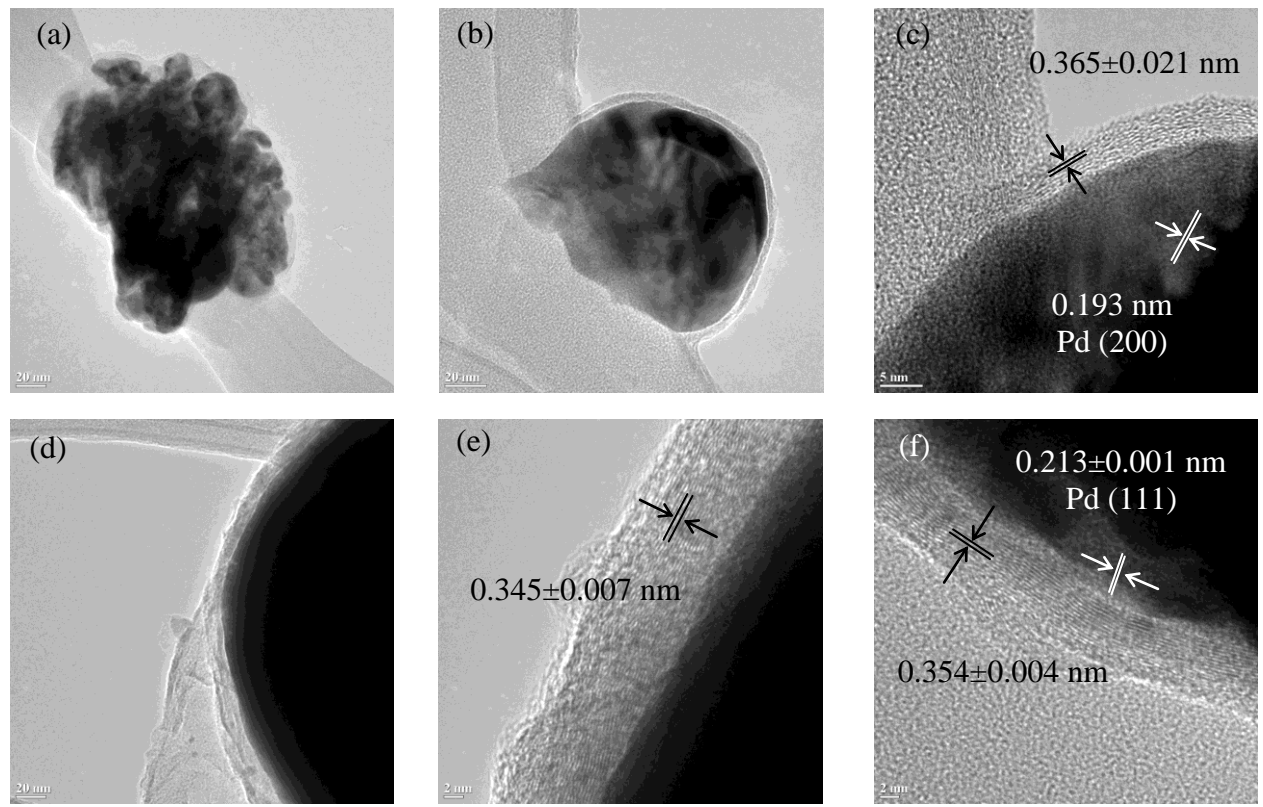


Figure 3.40 TEM images of graphene encapsulated PdNPs on Si wafer. Note: PdNPs (table 2.5, sample 13) were dispersed on unmodified Si wafer by drop-casting method and utilized to grow graphene shells.

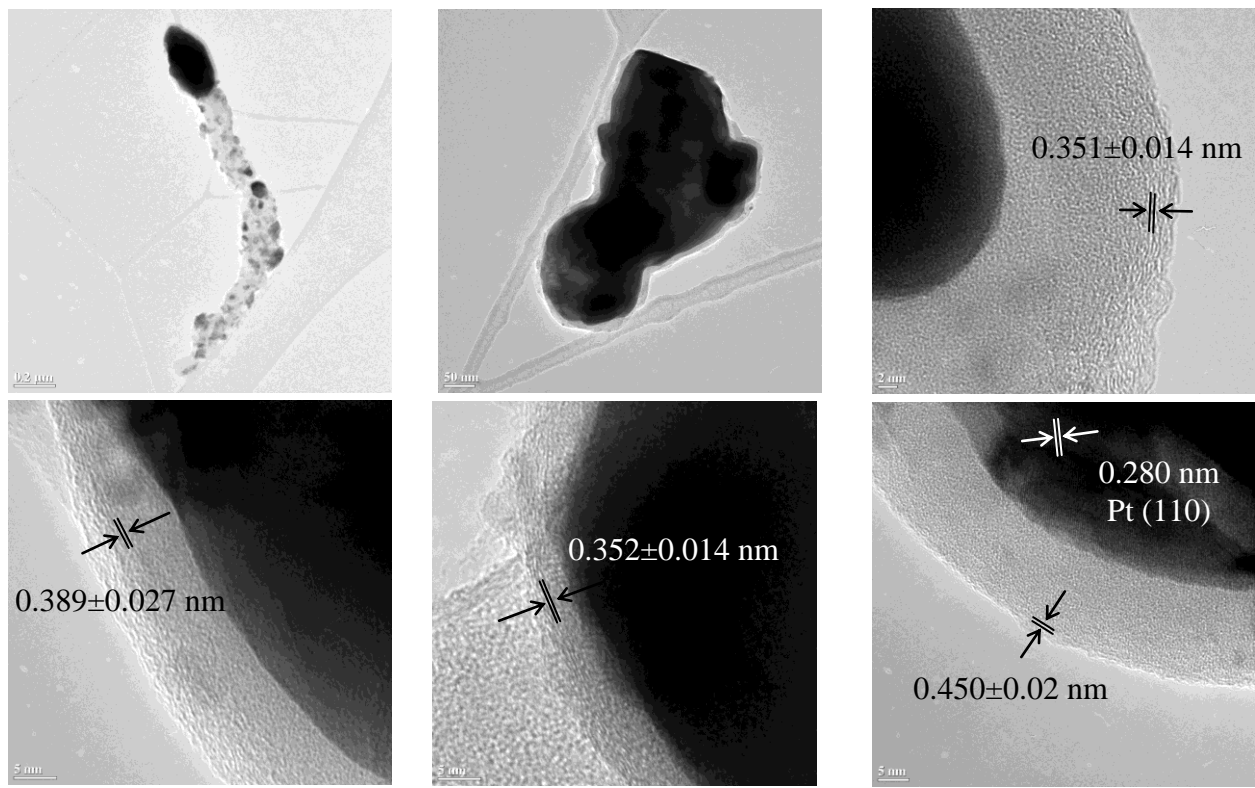


Figure 3.41 TEM images of graphene encapsulated PtNPs on Si wafer. Note: PtNPs (table 2.6, sample 13) were dispersed on unmodified Si wafer by drop-casting method and utilized to grow graphene shells.

Based on SEM and TEM images for graphene encapsulated gold nanoparticles (figure 3.39), significant aggregation and surface migration of gold nanoparticles were observed. Thus they could not maintain distinguished facets, with size increased to  $124.21 \pm 71.82$  nm. It should be noted that gold nanoparticles were dispersed on silicon wafer by drop-casting, the high density of particles and the close distance could further lead to their aggregation. The observed graphene shells have a thickness around 1 to 2 nm, with lattice spacing of  $\sim 0.35$  nm, well fitted to c-axis distance of graphene.<sup>122</sup> Some amorphous carbon also formed during CVD process, which was further confirmed by Raman spectroscopy that clearly showed D and G bands corresponding to disordered and graphitic carbon content, respectively.

Based on observation, we propose that graphene growth follows several steps: during CVD growth, Xylene first been reduced by hydrogen and deposited on gold surface, followed by the ordering and crystallization of C. Three processes took place simultaneously: (1) graphene fragments formed and spread; (2) gold nanoparticles changed shape at high temperature; (3) coalescence of particles initially closed with each other. After CVD process, more big gold clusters formed, and the average size of gold particles even increased to  $124.2 \pm 71.8$  nm. The graphene segments originally formed from “corners” kept wrapping the gold cluster and eventually formed graphene shell on the surface of particles.

XPS was applied to determine the chemical state of gold and carbon after graphene growth. In figure 3.42 (A-c), Fe 2p peaks were found and suggested Fe contamination. The iron contamination may attribute to that carbon source (xylene) was feed using a steel pipe. To minimize Fe contamination the tip of pipe was changed to glass. Au deconvolution peaks were demonstrated in figure 3.42 (B, a-c). As mentioned above, HAuCl<sub>4</sub>, Au, AuO<sub>x</sub> peaks were assigned. It was observed that AuO<sub>x</sub> peaks disappeared after graphene growth. Although AuO<sub>x</sub> is

instable at high temperature and especially should be reduced at H<sub>2</sub> environment, considering the fact that graphene shell only formed for oxidized gold nanoparticles, it is reasonable to believe that AuO<sub>x</sub> plays the most important role for the formation of graphene shell. C peak was also deconvoluted in figure 3.42 (B, d) for graphene growth sample, from which  $\pi-\pi^*$  peak (289.08 eV) was observed and indicated the formation of graphene.<sup>123</sup>

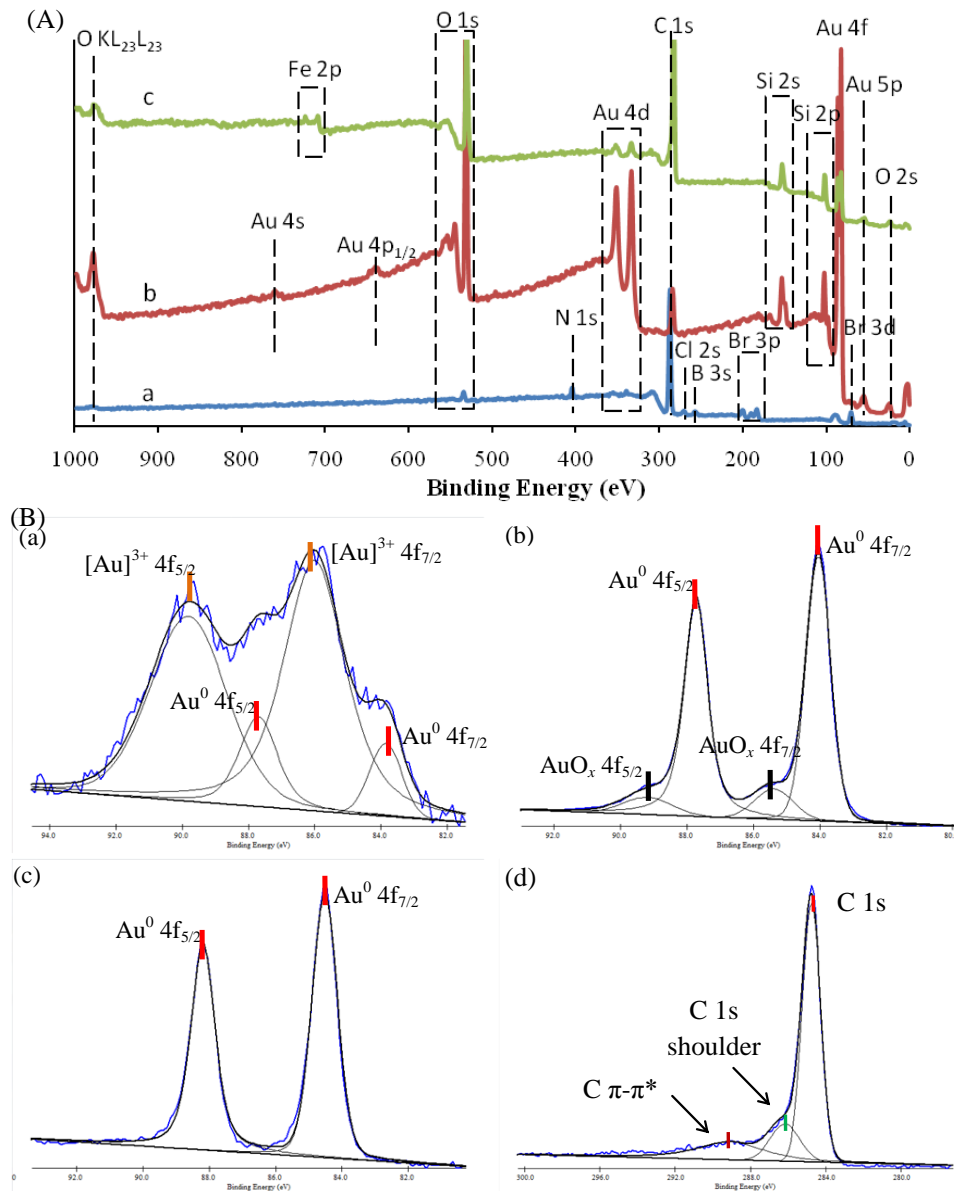


Figure 3.42 A) XPS spectra corresponding to AuNPs (a) before plasma oxidation, (b) after 30 min of plasma oxidation, and (c) after 1 h of graphene growth. B) Deconvoluted XPS spectra subtracted by linear background and fitted with Au 4f peaks corresponding to AuNPs (a) before plasma oxidation, (b) after 30 min of plasma oxidation, and (c) after 1 h of graphene growth. (d) Deconvoluted XPS of C 1s after graphene growth. Note: AuNPs (table 2.1, sample 10) were dispersed on unmodified Si wafer by drop casting method.

Table 3.12 Binding energy (eV) chart derived from XPS study for AuNPs (table 2.1, sample 10 before, after plasma oxidation, and after graphene growth) corresponding to the spectra as shown in figure 3.42.

Conditions	Bind Energy (eV)					
	Au 4f <sub>5/2</sub>			Au 4f <sub>7/2</sub>		
	[Au <sup>3+</sup> ]	AuO <sub>x</sub>	Au <sup>0</sup>	[Au <sup>3+</sup> ]	AuO <sub>x</sub>	Au <sup>0</sup>
Before Plasma	89.81	/	87.70	86.01	/	83.86
After Plasma	/	89.19	87.73	/	85.38	84.05
With Graphene	/	/	88.19	/	/	84.52

### *3.6 Raman mapping for nanoparticles after graphene growth*

Raman mapping was used to study the uniformity of the graphene growth on silicon wafer. The graphene encapsulated gold nanoparticles (table 2.1, sample 10), palladium nanoparticles (table 2.5, sample 13), and platinum nanoparticles (table 2.6, sample 13) samples were scanned for a  $15 \mu\text{m} \times 15 \mu\text{m}$  area with 100 points. The generated Raman spectra were then mapped with G band by integrating peak area from  $1500 \text{ cm}^{-1}$  to  $1700 \text{ cm}^{-1}$ . In the map, different colors and height show normalized intensities (single G-band peak intensity divided by highest intensity). Raman mapping plot were shown in figure 3.43 to figure 3.45, with inserted a typical Raman spectroscopy for each sample. It was observed that graphene encapsulated gold, palladium, and platinum have clear D-, G-band. The distribution of graphene structure on the surface of substrate can be estimated from Raman 3-D mapping. The “hot spots” are corresponding to high intensity of G-band peak, which can be attributed from the clusters of noble metal nanoparticles with graphene structure. The aggregation of noble metal nanoparticles is due to the drop-casting method and migration of nanoparticles during plasma oxidation and graphene growth.

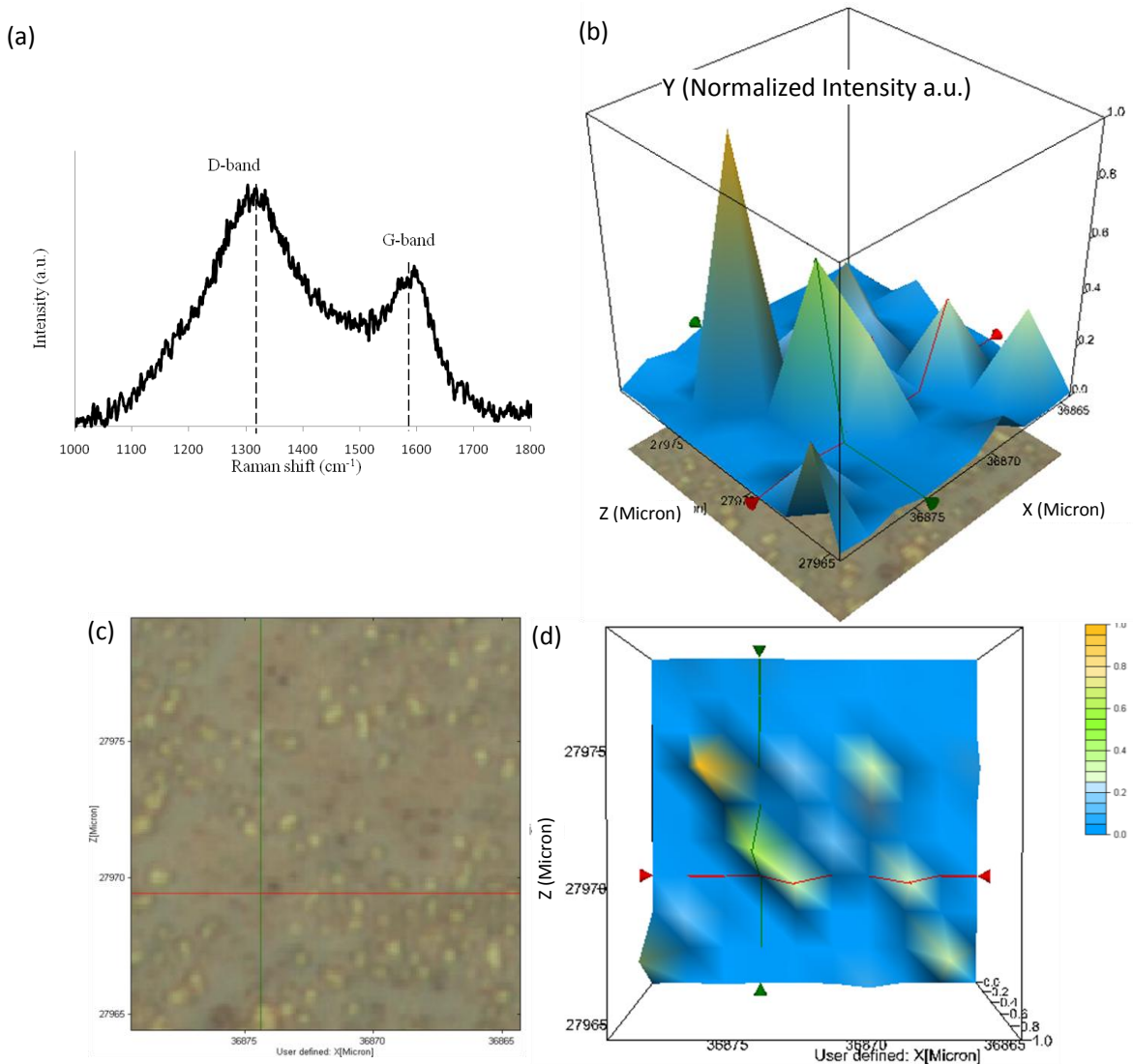


Figure 3.43 Raman 3D mapping for AuNPs after graphene growth. (a) Raman spectroscopy of graphene encapsulated AuNPs, (b) 3D map for graphene structure on sample surface, (c) sample surface has been scanned, and (d) vertical view of the 3D map. Note: AuNPs (table 2.1, sample 10) were dispersed on piranha cleaned Si wafer by drop casting method.

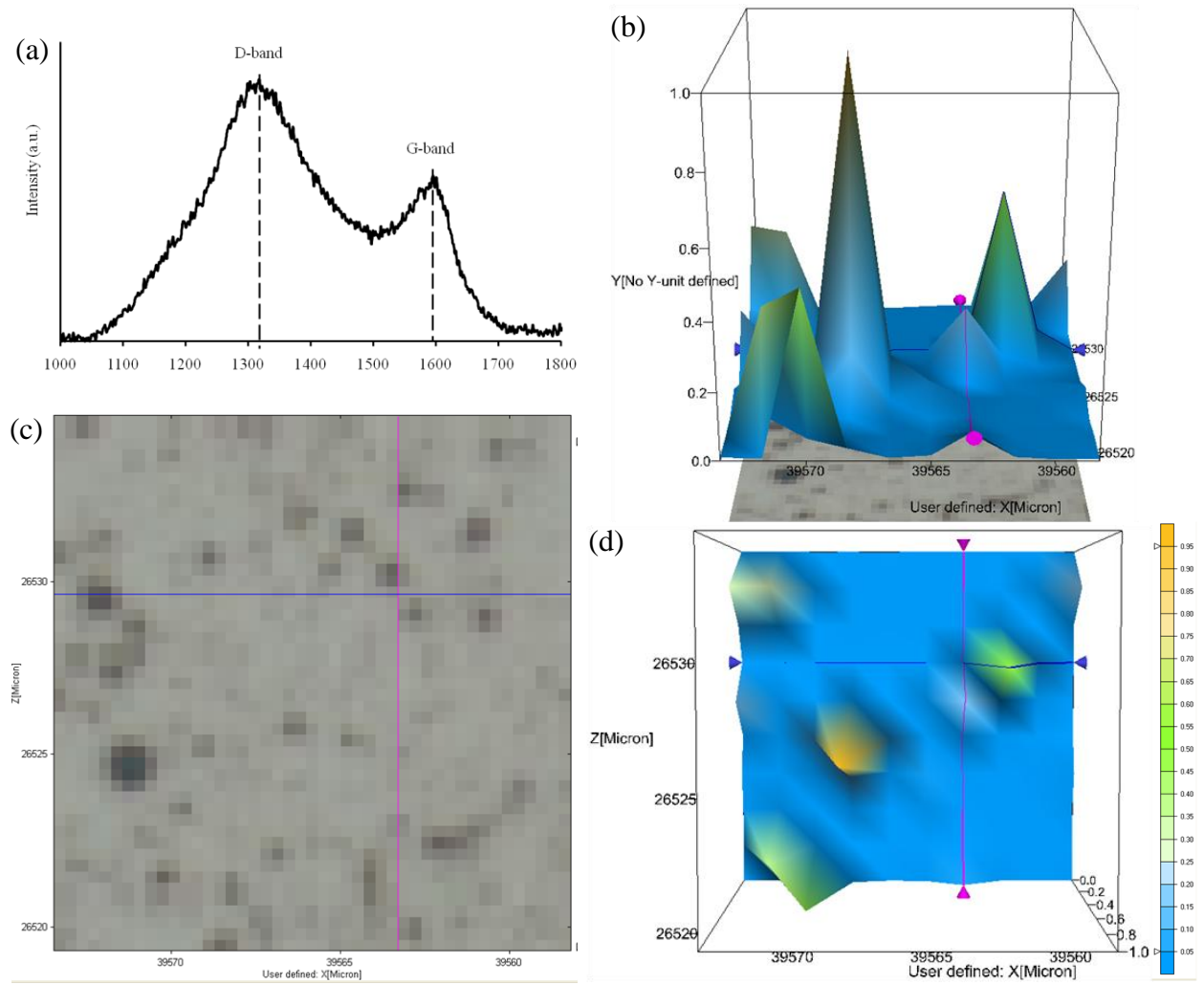


Figure 3.44 Raman 3D mapping for PdNPs after graphene growth. (a) Raman spectroscopy of graphene encapsulated PdNPs, (b) 3D map for graphene structure on sample surface, (c) sample surface has been scanned, and (d) vertical view of the 3D map. Note: *PdNPs (table 2.5, sample 13) were dispersed on piranha cleaned Si wafer by drop casting method.*

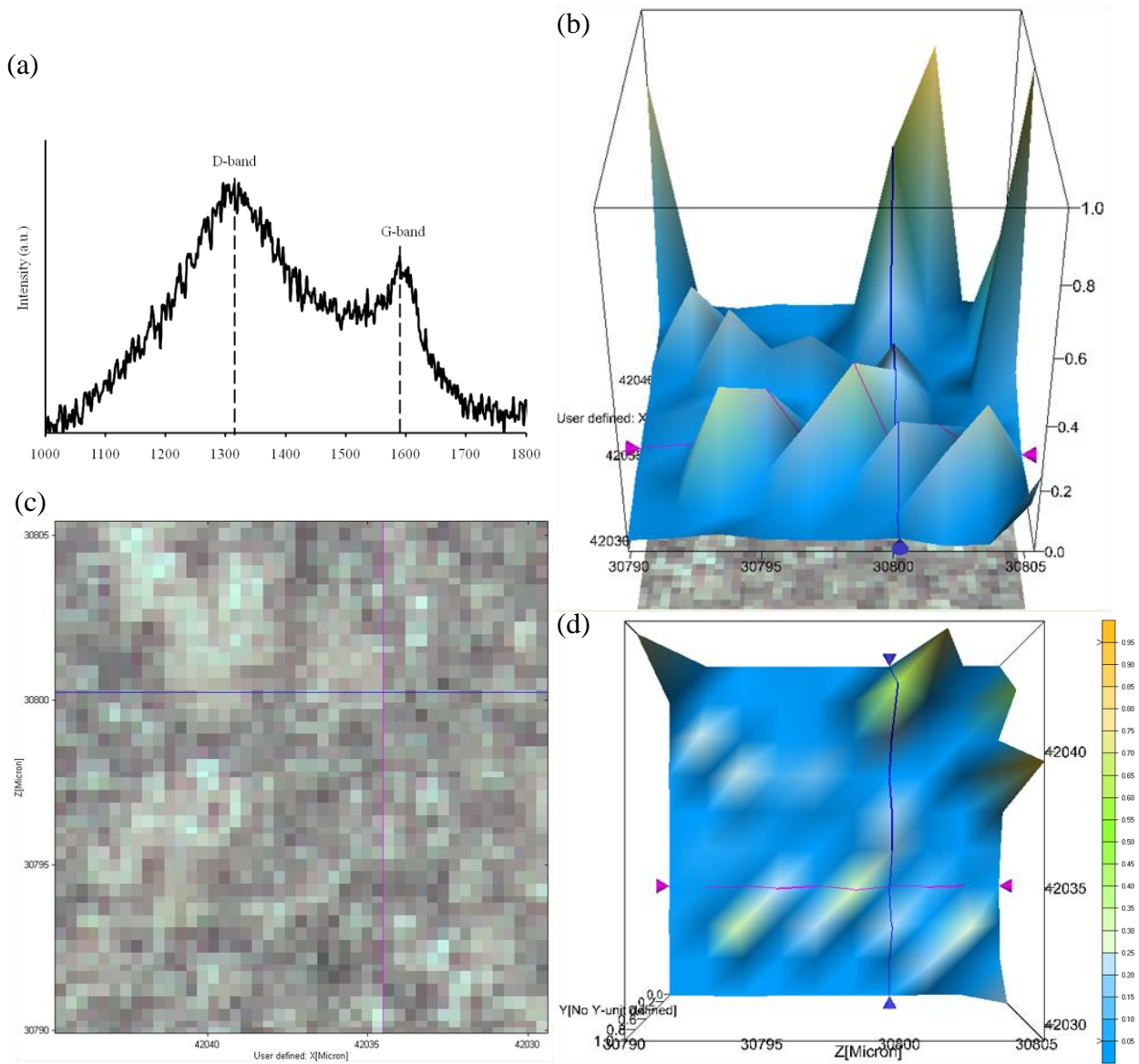


Figure 3.45 Raman 3D mapping for PtNPs after graphene growth. (a) Raman spectroscopy of graphene encapsulated PtNPs, (b) 3D map for graphene structure on sample surface, (c) sample surface has been scanned, and (d) vertical view of the 3D map. Note: PtNPs (table 2.6, sample 13) were dispersed on piranha cleaned Si wafer by drop casting method.

### *3.7 Dispersion of noble metal nanoparticles*

The purpose of dispersion nanoparticles on substrate by MPTMS functionalization is to get a uniform dispersed nanoparticles layer. A rough transition metal surface can enhance chemicals' Raman signal through excitation of localized surface plasmon. So, a suitable density mono-dispersed nanoparticles layer can provide the rough surface and enhance Raman scattering.

We functionalized silicon wafer with different concentration (12.4 mM and 2 mM, respectively) of MPTMS, compared the dispersion of commercial gold nanoparticles on those two functionalized silicon wafer. It was observed that silicon wafers functionalized with lower concentration (2 mM) of MPTMS obtained higher dispersion density for commercial gold nanoparticles, as shown in figure 3.46 (a - d). It was demonstrated that only when MPTMS form well-ordered monolayer with thiol headgroups uniformly distributed on the uppermost surface can efficiently pattern metal particles; while the MPTMS layer will become rough and less ordered when increasing the concentration of MPTMS.<sup>125</sup>

By decreasing the concentration of MPTMS and annealing functionalized silicon wafer at 80 °C, efficiency of pattern metal nanoparticles was increased. Then we used this approach further dispersed gold, palladium, and platinum nanoparticles on functionalized silicon wafer. Their SEM images were shown in figure 3.46 (e - h), which indicate that those noble metal nanoparticles can be patterned on MPTMS functionalized silicon wafer through our approach.

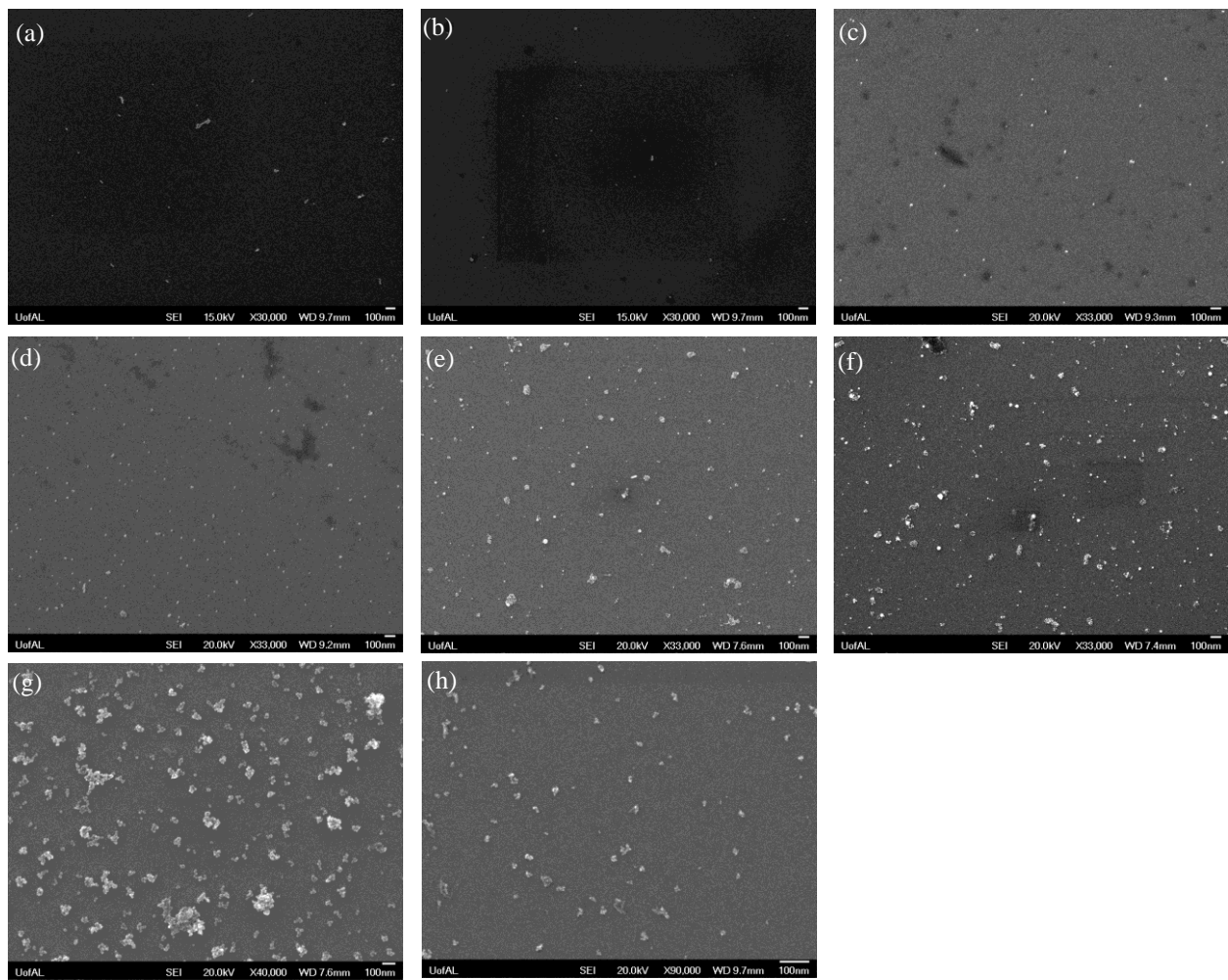


Figure 3.46 SEM images of (a, b) Commercial AuNPs dispersed on MPTMS (12.4 mM) functionalized silicon wafer, (c, d) Commercial AuNPs dispersed on MPTMS (2 mM) functionalized silicon wafer, (e, f) synthesized AuNPs (table 2.1, sample 7) dispersed on MPTMS (2 mM) functionalized silicon wafer, (g) synthesized PdNPs (table 2.5, sample 8) dispersed on MPTMS, (h) synthesized PtNPs (table 2.6, sample 8) dispersed on MPTMS.

### *3.8 Raman spectroscopy of methylene blue on noble metal nanoparticles*

As prepared gold nanoparticles, palladium nanoparticles, and platinum nanoparticles were dispersed on silicon wafer, SEM images were shown in 3.36 (e - f). The silicon wafers decorated with different kinds of nanoparticles were used as substrates for same amount of drop-casted methylene-blue (MB). MB was also drop-casted on bare silicon wafer as a control sample. Raman spectra for dried MB on different substrates were shown in figure 3.47. Peaks were assigned in table 3.13.

Surface Raman enhancement can be clearly observed on gold, and platinum. But it was not noticeable on palladium. For example, for band  $1620\text{ cm}^{-1}$ , which can be assigned as  $\nu(\text{C}-\text{C})$  ring, the intensity on bare silicon wafer ( $I_{ref}$ ) is 304.4. While  $I_{Au} = 1155.5$ ,  $I_{Pd} = 494.5$ , and  $I_{Pt} = 2626.8$ . So  $I_{ehc}/I_{ref}$  for AuNPs, PdNPs, and PtNPs are 3.8, 1.6, and 8.6, respectively.

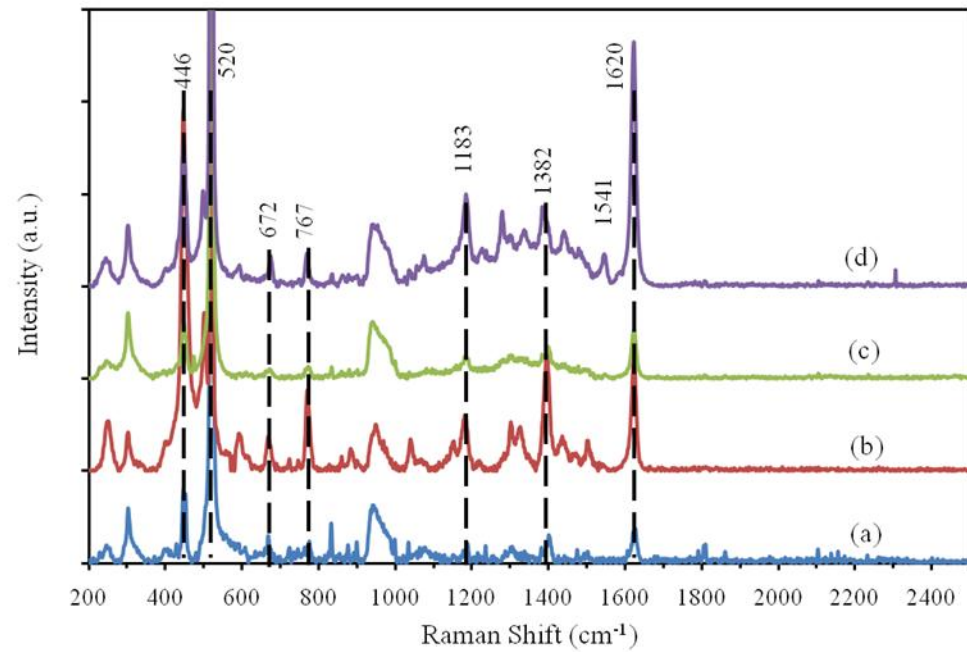


Figure 3.47 Raman spectroscopy for (a) Methylene-Blue (MB) dried on piranha cleaned silicon wafer by drop-casting, MB dried on silicon wafer decorated with (b) AuNPs, (c) PdNPs, (d) PtNPs.

Table 3.13 Assignment for Raman peaks of methylene blue

Raman shift/ cm <sup>-1</sup>	446	672	767	1183	1382	1541	1620
Peak assignment	$\delta(\text{C}-\text{N}-\text{C})$	$\gamma(\text{C}-\text{H})$	$\beta(\text{C}-\text{H})$	$\nu(\text{C}-\text{N})$	$\alpha(\text{C}-\text{H})$	$\text{vasym}(\text{C}-\text{C})$	$\nu(\text{C}-\text{C})$ ring

Where  $\delta$  is skeletal deformation,  $\gamma$  is out-of-plane bending,  $\beta$  is in-plane-bending,  $\nu$  is stretching,  $\alpha$  is in-plane ring deformation.

## CHAPTER 4

### CONCLUSIONS AND FUTURE WORK

Gold, palladium, and platinum nanoparticles were synthesized in aqueous solution. The influence of synthesis conditions on the size, shape, and crystallinity of nanoparticles was studied by varying parameters such as temperature, metal salt concentration, surfactant type and concentration, seed amount, reducing agent type, duration, and shape-control additives. Several conclusions can be made based on the fundamental studies described in this thesis:

(1) In gold nanoparticles single-step synthesis, the reaction Gibbs free energy ( $\Delta_r G$ ) kept large negative quantity in varies conditions, favored the formation of gold nanoparticles. Nanoparticle nuclei homogenously, supersaturation  $\sigma$  dominates particles size. Increasing temperature  $T$ , supersaturation decrease, resulted in a decrease of absolute value of volume Gibbs free energy  $|\Delta G_v|$ . Since critical size  $r^*$  for nucleus is reverse proportional to  $|\Delta G_v|$ , the minimum particle size increases. It should be noticed that when temperature increased higher than boiling point of water, the annealing for stabilizer will cause it rupture around the particles. Since CTAB bind more strongly on {100} facets of Au, the rupture of stabilizer may stimulate anisotropic growth of nanoparticles, generate different shapes of gold nanoparticles. A quenching step after synthesis gold at high temperature would induce defects to gold nanoparticles.

(2) Increasing surfactant concentration, size of particles will be reduced because of a generation of packed capping layer around particles. High concentration of metal salt boosts both nucleation and growth of nanoparticles. Also, it was observed that smaller amount of seed not

only can be nucleus for particle growth, but also can stimulate nucleation and result in a broad particle size distribution.

(3) Ostwald ripening was observed in synthesis palladium nanoparticles. The shape of Pd nanoparticles can be well controlled by adding KBr and KCl to increase anisotropic growth, resulting Pd nanocubes enclosed with {100} facets. The parameter study of synthesizing platinum nanoparticles mainly produced small Pt particles with narrow size distribution this can be attributed to fast nucleation process. To generate larger size of platinum nanoparticles, either violent synthesis conditions (reduced by strong reducing agent like NaBH<sub>4</sub>) or shape-control additives (e.g. AgNO<sub>3</sub>) can be induced.

The second part studied the oxidation behavior of noble metal nanoparticles. Plasma oxidation is an efficient approach for noble metal cleaning and oxidation, and the chemical state can be indicated by XPS. For gold nanoparticles, oxygen plasma first removes the excessive surfactant, reduces the unreacted metal salt (HAuCl<sub>4</sub>) to metallic gold, and then oxidizes Au<sup>0</sup> to AuO<sub>x</sub> ( $x \leq 1.5$ ). The percentage of AuO<sub>x</sub> reaches maximum when oxidation duration is 45 min, further oxidation may cause decomposition of gold oxide because of its instability at high temperature. The SEM images for gold nanoparticles after oxidized for different duration suggest that there was surface migration on gold nanoparticles, evidenced by the disappearance of sharp edges of as-prepared gold nanoparticles. Both palladium and platinum nanoparticles can be efficiently oxidized by plasma, generate PdO, PdO<sub>2</sub>, PtO, and PtO<sub>2</sub>, respectively. Plasma duration study for Pt shows that the oxidation product PtO<sub>2</sub> is more stable in oxygen plasma than PtO, supported by the fact that percentage of PtO<sub>2</sub> kept increasing during the whole oxidation process (5 ~ 45 min), whereas the percentage of Pt kept decreasing, and the amount of PtO

reached maximum within 5 min oxidation then slightly decrease, indicates partial transfer from PtO to PtO<sub>2</sub>. The thickness of oxide shells were estimated from XPS data.

SEM and TEM images show graphene shell on the surface of gold nanoparticles. The thickness of carbon shell is about 1 ~ 2 nm, with lattice spacing ~0.35nm, indicated the formation of graphene structure. Surface migration of gold nanoparticles during CVD process was evidenced by the increase of particle size (from 60 ~ 70 nm after plasma oxidation 30min, to ~ 120nm). Three processes happened simultaneously during CVD growth graphene: graphene fragments formation and spread, shape change of gold nanoparticles at high temperature, and gold nanoparticles aggregation. Graphene encapsulated palladium and platinum nanoparticles were also synthesized through process similar with CVD growth of graphene encapsulated gold nanoparticles. From Raman spectroscopy, D-band and G-band are distinguished for gold, palladium, and platinum nanoparticles after graphene growth. Raman mapping shows the distribution of graphene encapsulated noble metal nanoparticles. SERS study indicates both AuNPs and PtNPs can enhance Raman signal for methylene-blue by 3.8 and 8.6 times, respectively.

Future work could be on functionalization of multifunctional nanomaterials. To minimize aggregation during plasma oxidation and graphene growth, the gold nanoparticles can be dispersed on MPTMS functionalized silicon wafer, and then grow graphene. These graphene encapsulated noble metal nanoparticles have importance in the area of SERS-based sensing. Thus, future work will be focus on fundamentally understanding the SERS mechanism based on these hybrid nanoparticles, tuning their function based on structure and morphology of nanoparticles, and developing large area chemical detection platform.

## REFERENCES

1. Buzea, C.; Pacheco, II; Robbie, K., Nanomaterials and nanoparticles: Sources and toxicity. *Biointerphases* **2007**, 2 (4), MR17-MR71.
2. Satoh, N.; Nakashima, T.; Kamikura, K.; Yamamoto, K., Quantum size effect in TiO<sub>2</sub> nanoparticles prepared by finely controlled metal assembly on dendrimer templates. *Nature Nanotechnology* **2008**, 3 (2), 106-111.
3. Jiang, H. J.; Moon, K. S.; Dong, H.; Hua, F.; Wong, C. P., Size-dependent melting properties of tin nanoparticles. *Chemical Physics Letters* **2006**, 429 (4-6), 492-496.
4. Chen, X.; Mao, S. S., Titanium dioxide nanomaterials: Synthesis, properties, modifications, and applications. *Chemical Reviews* **2007**, 107 (7), 2891-2959.
5. Vancea, J.; Hoffmann, H.; Kastner, K., Mean free-path and effective density of conduction electrons in polycrystalline metal-films. *Thin Solid Films* **1984**, 121 (3), 201-216.
6. Porta, F.; Prati, L.; Rossi, M.; Coluccia, S.; Martra, G., Metal sols as a useful tool for heterogeneous gold catalyst preparation: reinvestigation of a liquid phase oxidation. *Catalysis Today* **2000**, 61 (1-4), 165-172.
7. Lampert, J. K.; Kazi, M. S.; Farrauto, R. J., Palladium catalyst performance for methane emissions abatement from lean burn natural gas vehicles. *Applied Catalysis B-Environmental* **1997**, 14 (3-4), 211-223.
8. Yoshitake, T.; Shimakawa, Y.; Kuroshima, S.; Kimura, H.; Ichihashi, T.; Kubo, Y.; Kasuya, D.; Takahashi, K.; Kokai, F.; Yudasaka, M.; Iijima, S., Preparation of fine platinum catalyst supported on single-wall carbon nanohorns for fuel cell application. *Physica B-Condensed Matter* **2002**, 323 (1-4), 124-126.
9. Lamprecht, B.; Schider, G.; Lechner, R. T.; Ditlbacher, H.; Krenn, J. R.; Leitner, A.; Ausseneegg, F. R., Metal nanoparticle gratings: Influence of dipolar particle interaction on the plasmon resonance. *Physical Review Letters* **2000**, 84 (20), 4721-4724.
10. Narayanan, R.; El-Sayed, M. A., Catalysis with transition metal nanoparticles in colloidal solution: Nanoparticle shape dependence and stability. *Journal of Physical Chemistry B* **2005**, 109 (26), 12663-12676.
11. Halperin, W. P., Quantum size effects in metal particles. *Reviews of Modern Physics* **1986**, 58 (3), 533-606.

12. Mueller, R. H.; Maeder, K.; Gohla, S., Solid lipid nanoparticles (SLN) for controlled drug delivery: A review of the state of the art. *European Journal of Pharmaceutics and Biopharmaceutics* **2000**, *50* (1), 161-177.
13. Murphy, C. J.; San, T. K.; Gole, A. M.; Orendorff, C. J.; Gao, J. X.; Gou, L.; Hunyadi, S. E.; Li, T., Anisotropic metal nanoparticles: Synthesis, assembly, and optical applications. *Journal of Physical Chemistry B* **2005**, *109* (29), 13857-13870.
14. Sau, T. K.; Rogach, A. L., Nonspherical Noble Metal Nanoparticles: Colloid-Chemical Synthesis and Morphology Control. *Advanced Materials* **2010**, *22* (16), 1781-1804.
15. Brown, K. R.; Walter, D. G.; Natan, M. J., Seeding of colloidal Au nanoparticle solutions. 2. Improved control of particle size and shape. *Chemistry of Materials* **2000**, *12* (2), 306-313.
16. Walker, C. H.; St John, J. V.; Wisian-Neilson, P., Synthesis and size control of cold nanoparticles stabilized by poly(methylphenylphosphazene). *Journal of the American Chemical Society* **2001**, *123* (16), 3846-3847.
17. Guo, Q. J.; Teng, X. W.; Rahman, S.; Yang, H., Patterned Langmuir-Blodgett films of monodisperse nanoparticles of iron oxide using soft lithography. *Journal of the American Chemical Society* **2003**, *125* (3), 630-631.
18. Sun, Y. G.; Xia, Y. N., Shape-controlled synthesis of gold and silver nanoparticles. *Science* **2002**, *298* (5601), 2176-2179.
19. Vayssières, L., Growth of arrayed nanorods and nanowires of ZnO from aqueous solutions. *Advanced Materials* **2003**, *15* (5), 464-466.
20. Sau, T. K.; Murphy, C. J., Room temperature, high-yield synthesis of multiple shapes of gold nanoparticles in aqueous solution. *Journal of the American Chemical Society* **2004**, *126* (28), 8648-8649.
21. Gao, J. X.; Bender, C. M.; Murphy, C. J., Dependence of the gold nanorod aspect ratio on the nature of the directing surfactant in aqueous solution. *Langmuir* **2003**, *19* (21), 9065-9070.
22. Xia, Y. N.; Yang, P. D.; Sun, Y. G.; Wu, Y. Y.; Mayers, B.; Gates, B.; Yin, Y. D.; Kim, F.; Yan, Y. Q., One-dimensional nanostructures: Synthesis, characterization, and applications. *Advanced Materials* **2003**, *15* (5), 353-389.
23. Chopra, N., Multifunctional and multicomponent heterostructured one-dimensional nanostructures: advances in growth, characterisation, and applications. *Materials Technology* **2010**, *25* (3-4), 212-230.
24. Chen, S. H.; Carroll, D. L., Synthesis and characterization of truncated triangular silver nanoplates. *Nano Letters* **2002**, *2* (9), 1003-1007.

25. Zou, G. F.; Xiong, K.; Jiang, C. L.; Li, H.; Wang, Y.; Zhang, S. Y.; Qian, Y. T., Magnetic Fe<sub>3</sub>O<sub>4</sub> nanodisc synthesis on a large scale via a surfactant-assisted process. *Nanotechnology* **2005**, *16* (9), 1584-1588.
26. Swami, A.; Kumar, A.; Selvakannan, P. R.; Mandal, S.; Pasricha, R.; Sastry, M., Highly oriented gold nanoribbons by the reduction of aqueous chloroaurate ions by hexadecylaniline Langmuir monolayers. *Chemistry of Materials* **2003**, *15* (1), 17-19.
27. Zhao, N.; Wei, Y.; Sun, N. J.; Chen, Q. J.; Bai, J. W.; Zhou, L. P.; Qin, Y.; Li, M. X.; Qi, L. M., Controlled synthesis of gold nanobelts and nanocombs in aqueous mixed surfactant solutions. *Langmuir* **2008**, *24* (3), 991-998.
28. Tao, A. R.; Habas, S.; Yang, P. D., Shape control of colloidal metal nanocrystals. *Small* **2008**, *4* (3), 310-325.
29. Lim, B.; Jiang, M. J.; Tao, J.; Camargo, P. H. C.; Zhu, Y. M.; Xia, Y. N., Shape-Controlled Synthesis of Pd Nanocrystals in Aqueous Solutions. *Advanced Functional Materials* **2009**, *19* (2), 189-200.
30. Chen, J.; Saeki, F.; Wiley, B. J.; Cang, H.; Cobb, M. J.; Li, Z. Y.; Au, L.; Zhang, H.; Kimmey, M. B.; Li, X. D.; Xia, Y., Gold nanocages: Bioconjugation and their potential use as optical imaging contrast agents. *Nano Letters* **2005**, *5* (3), 473-477.
31. Tang, Y.; Ouyang, M., Tailoring properties and functionalities of metal nanoparticles through crystallinity engineering. *Nature Materials* **2007**, *6* (10), 754-759.
32. Murphy, C. J.; Thompson, L. B.; Alkilany, A. M.; Sisco, P. N.; Boulos, S. P.; Sivapalan, S. T.; Yang, J. A.; Chernak, D. J.; Huang, J. Y., The Many Faces of Gold Nanorods. *Journal of Physical Chemistry Letters* **2010**, *1* (19), 2867-2875.
33. Gugliotti, L. A.; Feldheim, D. L.; Eaton, B. E., RNA-mediated control of metal nanoparticle shape. *Journal of the American Chemical Society* **2005**, *127* (50), 17814-17818.
34. Petroski, J. M.; Wang, Z. L.; Green, T. C.; El-Sayed, M. A., Kinetically controlled growth and shape formation mechanism of platinum nanoparticles. *Journal of Physical Chemistry B* **1998**, *102* (18), 3316-3320.
35. Jin, M. S.; Liu, H. Y.; Zhang, H.; Xie, Z. X.; Liu, J. Y.; Xia, Y. N., Synthesis of Pd Nanocrystals Enclosed by {100} Facets and with Sizes < 10 nm for Application in CO Oxidation. *Nano Research* **2011**, *4* (1), 83-91.
36. Grzelczak, M.; Perez-Juste, J.; Mulvaney, P.; Liz-Marzan, L. M., Shape control in gold nanoparticle synthesis. *Chemical Society Reviews* **2008**, *37* (9), 1783-1791.
37. Yong, K. T.; Sahoo, Y.; Choudhury, K. R.; Swihart, M. T.; Minter, J. R.; Prasad, P. N., Shape control of PbSe nanocrystals using noble metal seed particles. *Nano Letters* **2006**, *6* (4), 709-714.

38. Song, H.; Kim, F.; Connor, S.; Somorjai, G. A.; Yang, P. D., Pt nanocrystals: Shape control and Langmuir-Blodgett monolayer formation. *Journal of Physical Chemistry B* **2005**, *109* (1), 188-193.
39. Huang, S. X.; Ma, H. Y.; Zhang, X. K.; Yong, F. F.; Feng, X. L.; Pan, W.; Wang, X. N.; Wang, Y.; Chen, S. H., Electrochemical synthesis of gold nanocrystals and their 1D and 2D organization. *Journal of Physical Chemistry B* **2005**, *109* (42), 19823-19830.
40. Callegari, A.; Tonti, D.; Chergui, M., Photochemically grown silver nanoparticles with wavelength-controlled size and shape. *Nano Letters* **2003**, *3* (11), 1565-1568.
41. Pastoriza-Santos, I.; Liz-Marzan, L. M., N,N-Dimethylformamide as a Reaction Medium for Metal Nanoparticle Synthesis. *Advanced Functional Materials* **2009**, *19* (5), 679-688.
42. Song, Y.; Garcia, R. M.; Dorin, R. M.; Wang, H. R.; Qiu, Y.; Coker, E. N.; Steen, W. A.; Miller, J. E.; Shelnutt, J. A., Synthesis of platinum nanowire networks using a soft template. *Nano Letters* **2007**, *7* (12), 3650-3655.
43. Correa-Duarte, M. A.; Liz-Marzan, L. M., Carbon nanotubes as templates for one-dimensional nanoparticle assemblies. *Journal of Materials Chemistry* **2006**, *16* (1), 22-25.
44. Guo, Y. G.; Wan, L. J.; Zhu, C. F.; Yang, D. L.; Chen, D. M.; Bai, C. L., Ordered Ni-Cu nanowire array with enhanced coercivity. *Chemistry of Materials* **2003**, *15* (3), 664-667.
45. Zhang, H.; Jin, M. S.; Wang, J. G.; Li, W. Y.; Camargo, P. H. C.; Kim, M. J.; Yang, D. R.; Xie, Z. X.; Xia, Y. A., Synthesis of Pd-Pt Bimetallic Nanocrystals with a Concave Structure through a Bromide-Induced Galvanic Replacement Reaction. *Journal of the American Chemical Society* **2011**, *133* (15), 6078-6089.
46. Murphy, C. J.; Gole, A. M.; Stone, J. W.; Sisco, P. N.; Alkilany, A. M.; Goldsmith, E. C.; Baxter, S. C., Gold Nanoparticles in Biology: Beyond Toxicity to Cellular Imaging. *Accounts of Chemical Research* **2008**, *41* (12), 1721-1730.
47. Alvarez, M. M.; Khoury, J. T.; Schaaff, T. G.; Shafiqullin, M. N.; Vezmar, I.; Whetten, R. L., Optical absorption spectra of nanocrystal gold molecules. *Journal of Physical Chemistry B* **1997**, *101* (19), 3706-3712.
48. Link, S.; Mohamed, M. B.; El-Sayed, M. A., Simulation of the optical absorption spectra of gold nanorods as a function of their aspect ratio and the effect of the medium dielectric constant. *Journal of Physical Chemistry B* **1999**, *103* (16), 3073-3077.
49. Kimling, J.; Maier, M.; Okenve, B.; Kotaidis, V.; Ballot, H.; Plech, A., Turkevich method for gold nanoparticle synthesis revisited. *Journal of Physical Chemistry B* **2006**, *110* (32), 15700-15707.

50. Frens, G., CONTROLLED NUCLEATION FOR REGULATION OF PARTICLE-SIZE IN MONODISPERSE GOLD SUSPENSIONS. *Nature-Physical Science* **1973**, 241 (105), 20-22.
51. Brust, M.; Walker, M.; Bethell, D.; Schiffrin, D. J.; Whyman, R., SYNTHESIS OF THIOL-DERIVATIZED GOLD NANOPARTICLES IN A 2-PHASE LIQUID-LIQUID SYSTEM. *Journal of the Chemical Society-Chemical Communications* **1994**, (7), 801-802.
52. Martin, M. N.; Basham, J. I.; Chando, P.; Eah, S. K., Charged Gold Nanoparticles in Non-Polar Solvents: 10-min Synthesis and 2D Self-Assembly. *Langmuir* **2010**, 26 (10), 7410-7417.
53. Jana, N. R.; Gearheart, L.; Murphy, C. J., Seed-mediated growth approach for shape-controlled synthesis of spheroidal and rod-like gold nanoparticles using a surfactant template. *Advanced Materials* **2001**, 13 (18), 1389-1393.
54. Busbee, B. D.; Obare, S. O.; Murphy, C. J., An improved synthesis of high-aspect-ratio gold nanorods. *Advanced Materials* **2003**, 15 (5), 414- 416.
55. Kwon, M. S.; Kim, N.; Park, C. M.; Lee, J. S.; Kang, K. Y.; Park, J., Palladium nanoparticles entrapped in aluminum hydroxide: Dual catalyst for alkene hydrogenation and aerobic alcohol oxidation. *Organic Letters* **2005**, 7 (6), 1077-1079.
56. Matsumura, Y.; Shen, W. J.; Ichihashi, Y.; Okumura, M., Low-temperature methanol synthesis catalyzed over ultrafine palladium particles supported on cerium oxide. *Journal of Catalysis* **2001**, 197 (2), 267-272.
57. Gray, M. R.; McCaffrey, W. C., Role of chain reactions and olefin formation in cracking, hydroconversion, and coking of petroleum and bitumen fractions. *Energy & Fuels* **2002**, 16 (3), 756-766.
58. Venezia, A. M.; Liotta, L. F.; Pantaleo, G.; La Parola, V.; Deganello, G.; Beck, A.; Koppany, Z.; Frey, K.; Horvath, D.; Guczi, L., Activity of SiO<sub>2</sub> supported gold-palladium catalysts in CO oxidation. *Applied Catalysis a-General* **2003**, 251 (2), 359-368.
59. Kishi, H.; Mizuno, Y.; Chazono, H., Base-metal electrode-multilayer ceramic capacitors: Past, present and future perspectives. *Japanese Journal of Applied Physics Part 1-Regular Papers Short Notes & Review Papers* **2003**, 42 (1), 1-15.
60. Kishore, S.; Nelson, J. A.; Adair, J. H.; Eklund, P. C., Hydrogen storage in spherical and platelet palladium nanoparticles. *Journal of Alloys and Compounds* **2005**, 389 (1-2), 234-242.
61. Wiley, B.; Herricks, T.; Sun, Y. G.; Xia, Y. N., Polyol synthesis of silver nanoparticles: Use of chloride and oxygen to promote the formation of single-crystal, truncated cubes and tetrahedrons. *Nano Letters* **2004**, 4 (9), 1733-1739.
62. Teranishi, T.; Miyake, M., Size control of palladium nanoparticles and their crystal structures. *Chemistry of Materials* **1998**, 10 (2), 594-600.

63. Rosenber.B; Vancamp, L.; Krigas, T., Inhibition of cell division in escherichia coli by electrolysis products from a platinum electrode. *Nature* **1965**, 205 (4972), 698- 699.
64. Ahmadi, T. S.; Wang, Z. L.; Green, T. C.; Henglein, A.; ElSayed, M. A., Shape-controlled synthesis of colloidal platinum nanoparticles. *Science* **1996**, 272 (5270), 1924-1926.
65. Imura, K.; Okamoto, H., Development of novel near-field microspectroscopy and imaging of local excitations and wave functions of nanomaterials. *Bulletin of the Chemical Society of Japan* **2008**, 81 (6), 659-675.
66. Willets, K. A.; Van Duyne, R. P., Localized surface plasmon resonance spectroscopy and sensing. *Annual Review of Physical Chemistry* **2007**, 58, 267-297.
67. Hirakawa, T.; Kamat, P. V., Charge separation and catalytic activity of Ag@TiO<sub>2</sub> core-shell composite clusters under UV-irradiation. *Journal of the American Chemical Society* **2005**, 127 (11), 3928-3934.
68. Cortie, M. B.; McDonagh, A. M., Synthesis and optical properties of hybrid and alloy plasmonic nanoparticles. *Chemical Reviews* **2011**, 111 (6), 3713-3735.
69. Naknam, P.; Luengnaruemitchai, A.; Wongkasemjit, S., Au/ZnO and Au/ZnO-Fe<sub>2</sub>O<sub>3</sub> Prepared by Deposition-Precipitation and Their Activity in the Preferential Oxidation of CO. *Energy & Fuels* **2009**, 23, 5084-5091.
70. Chen, C. T.; Chen, Y. C., Fe<sub>3</sub>O<sub>4</sub>/TiO<sub>2</sub> core/shell nanoparticles as affinity probes for the analysis of phosphopeptides using TiO<sub>2</sub> surface-assisted laser desorption/ionization mass spectrometry. *Analytical Chemistry* **2005**, 77 (18), 5912-5919.
71. Tresback, J. S.; Vasiliev, A. L.; Padture, N. P.; Park, S. Y.; Berger, P. R., Characterization and electrical properties of individual Au-NiO-Au heterojunction nanowires. *Ieee Transactions on Nanotechnology* **2007**, 6 (6), 676-681.
72. Qu, L. T.; Dai, L. M.; Osawa, E., Shape/size-control led syntheses of metal nanoparticles for site-selective modification of carbon nanotubes. *Journal of the American Chemical Society* **2006**, 128 (16), 5523-5532.
73. Lu, G. H.; Mao, S.; Park, S.; Ruoff, R. S.; Chen, J. H., Facile, Noncovalent Decoration of Graphene Oxide Sheets with Nanocrystals. *Nano Research* **2009**, 2 (3), 192-200.
74. Jr., W. S. H.; Offeman, R. E., *Preparation of Graphitic Oxide*. *American Chemical Society* **1958**, 80 (6), 1339.
75. Ono, L. K.; Cuenya, B. R., Formation and thermal stability of Au<sub>2</sub>O<sub>3</sub> on gold nanoparticles: Size and support effects. *Journal of Physical Chemistry C* **2008**, 112 (12), 4676-4686.

76. Haruta, M.; Tsubota, S.; Kobayashi, T.; Kageyama, H.; Genet, M. J.; Delmon, B., LOW-TEMPERATURE OXIDATION OF CO OVER GOLD SUPPORTED ON TiO<sub>2</sub>, ALPHA-FE<sub>2</sub>O<sub>3</sub>, AND CO<sub>3</sub>O<sub>4</sub>. *Journal of Catalysis* **1993**, *144* (1), 175-192.
77. Huang, J. H.; Akita, T.; Faye, J.; Fujitani, T.; Takei, T.; Haruta, M., Propene Epoxidation with Dioxygen Catalyzed by Gold Clusters. *Angewandte Chemie-International Edition* **2009**, *48* (42), 7862-7866.
78. Demoulin, O.; Navez, M.; Gaigneaux, E. M.; Ruiz, P.; Mamede, A. S.; Granger, P.; Payen, E., Operando resonance Raman spectroscopic characterisation of the oxidation state of palladium in Pd/gamma-Al<sub>2</sub>O<sub>3</sub> catalysts during the combustion of methane. *Physical Chemistry Chemical Physics* **2003**, *5* (20), 4394-4401.
79. Bondzie, V. A.; Parker, S. C.; Campbell, C. T., Oxygen adsorption on well-defined gold particles on TiO<sub>2</sub>(110). *Journal of Vacuum Science & Technology a-Vacuum Surfaces and Films* **1999**, *17* (4), 1717-1720.
80. King, D. E., OXIDATION OF GOLD BY ULTRAVIOLET-LIGHT AND OZONE AT 25-DEGREES-C. *Journal of Vacuum Science & Technology a-Vacuum Surfaces and Films* **1995**, *13* (3), 1247-1253.
81. Parker, D. H.; Koel, B. E., CHEMISORPTION OF HIGH COVERAGES OF ATOMIC OXYGEN ON THE PT(111), PD(111), AND AU(111) SURFACES. *Journal of Vacuum Science & Technology a-Vacuum Surfaces and Films* **1990**, *8* (3), 2585-2590.
82. Izumi, T.; Watanabe, I.; Yokoyama, Y., Activation of a gold electrode by electrochemical oxidation reduction pretreatment in hydrochloric-acid. *Journal of Electroanalytical Chemistry* **1991**, *303* (1-2), 151-160.
83. Tsai, H. C.; Hu, E.; Perng, K.; Chen, M. K.; Wu, J. C.; Chang, Y. S., Instability of gold oxide Au<sub>2</sub>O<sub>3</sub>. *Surface Science* **2003**, *537* (1-3), L447-L450.
84. Blackstock, J. J.; Stewart, D. R.; Li, Z., Plasma-produced ultra-thin platinum-oxide films for nanoelectronics: physical characterization. *Applied Physics a-Materials Science & Processing* **2005**, *80* (6), 1343-1353.
85. Koslowski, B.; Boyen, H. G.; Wilderotter, C.; Kastle, G.; Zieman, P.; Wahrenberg, R.; Oelhafen, P., Oxidation of preferentially (111)-oriented Au films in an oxygen plasma investigated by scanning tunneling microscopy and photoelectron spectroscopy. *Surface Science* **2001**, *475* (1-3), 1-10.
86. Allen, M. J.; Tung, V. C.; Kaner, R. B., Honeycomb Carbon: A Review of Graphene. *Chemical Reviews* **2010**, *110* (1), 132-145.
87. Geim, A. K.; Novoselov, K. S., The rise of graphene. *Nature Materials* **2007**, *6* (3), 183-191.

88. Gao, W.; Alemany, L. B.; Ci, L. J.; Ajayan, P. M., New insights into the structure and reduction of graphite oxide. *Nature Chemistry* **2009**, *1* (5), 403-408.
89. Gao, X. F.; Jang, J.; Nagase, S., Hydrazine and Thermal Reduction of Graphene Oxide: Reaction Mechanisms, Product Structures, and Reaction Design. *Journal of Physical Chemistry C* **2010**, *114* (2), 832-842.
90. Kosynkin, D. V.; Higginbotham, A. L.; Sinitskii, A.; Lomeda, J. R.; Dimiev, A.; Price, B. K.; Tour, J. M., Longitudinal unzipping of carbon nanotubes to form graphene nanoribbons. *Nature* **2009**, *458* (7240), 872- 876.
91. Wu, J. S.; Pisula, W.; Mullen, K., Graphenes as potential material for electronics. *Chemical Reviews* **2007**, *107* (3), 718-747.
92. Sutter, P., EPITAXIAL GRAPHENE How silicon leaves the scene. *Nature Materials* **2009**, *8* (3), 171-172.
93. Emtsev, K. V.; Bostwick, A.; Horn, K.; Jobst, J.; Kellogg, G. L.; Ley, L.; McChesney, J. L.; Ohta, T.; Reshanov, S. A.; Rohrl, J.; Rotenberg, E.; Schmid, A. K.; Waldmann, D.; Weber, H. B.; Seyller, T., Towards wafer-size graphene layers by atmospheric pressure graphitization of silicon carbide. *Nature Materials* **2009**, *8* (3), 203-207.
94. Bae, S.; Kim, H.; Lee, Y.; Xu, X. F.; Park, J. S.; Zheng, Y.; Balakrishnan, J.; Lei, T.; Kim, H. R.; Song, Y. I.; Kim, Y. J.; Kim, K. S.; Ozyilmaz, B.; Ahn, J. H.; Hong, B. H.; Iijima, S., Roll-to-roll production of 30-inch graphene films for transparent electrodes. *Nature Nanotechnology* **2010**, *5* (8), 574-578.
95. Dresselhaus, M. S.; Dresselhaus, G., Intercalation compounds of graphite. *Advances in Physics* **2002**, *51* (1), 139- 326.
96. Raty, J. Y.; Gygi, F.; Galli, G., Growth of carbon nanotubes on metal nanoparticles: A microscopic mechanism from ab initio molecular dynamics simulations. *Physical Review Letters* **2005**, *95* (9), 1- 4.
97. Lee, S. Y.; Yamada, M.; Miyake, M., Synthesis of carbon nanotubes over gold nanoparticle supported catalysts. *Carbon* **2005**, *43* (13), 2654-2663.
98. Takagi, D.; Homma, Y.; Hibino, H.; Suzuki, S.; Kobayashi, Y., Single-walled carbon nanotube growth from highly activated metal nanoparticles. *Nano Letters* **2006**, *6* (12), 2642-2645.
99. Sutter, E.; Sutter, P.; Zhu, Y. M., Assembly and interaction of Au/C core-shell nanostructures: In situ observation in the transmission electron microscope. *Nano Letters* **2005**, *5* (10), 2092-2096.
100. Hore, S.; Kaiser, G.; Hu, Y. S.; Schulz, A.; Konuma, M.; Gotz, G.; Sigle, W.; Verhoeven, A.; Maier, J., Carbonization of polyethylene on gold oxide. *Journal of Materials Chemistry* **2008**, *18* (46), 5589-5591.

101. Kim, J. H.; Kim, C. K.; Kim, Y. H.; Yoon, C. S., Synthesis of carbon-encapsulated gold nanoparticles in polyimide matrix. *Colloids and Surfaces a-Physicochemical and Engineering Aspects* **2008**, 321 (1-3), 297-300.
102. Chopra, N.; Bachas, L. G.; Knecht, M. R., Fabrication and Biofunctionalization of Carbon-Encapsulated Au Nanoparticles. *Chemistry of Materials* **2009**, 21 (7), 1176- 1178.
103. Bhaviripudi, S.; Mile, E.; Steiner, S. A.; Zare, A. T.; Dresselhaus, M. S.; Belcher, A. M.; Kong, J., CVD synthesis of single-walled carbon nanotubes from gold nanoparticle catalysts. *Journal of the American Chemical Society* **2007**, 129 (6), 1516- 1517.
104. Yang, S. R.; Kolbessen, B. O., A comparative study of the growth of octadecyltrichlorosilane and 3-mercaptopropyltrimethoxysilane self-assembled monolayers on hydrophilic silicon surfaces. *Applied Surface Science* **2008**, 255 (5), 1726-1735.
105. De Yoreo, J. J.; Vekilov, P. G., Principles of crystal nucleation and growth. In *Biomineralization*, Dove, P. M.; DeYoreo, J. J.; Weiner, S., Eds. Mineralogical Soc America: Washington, 2003; Vol. 54, 57-93.
106. Chopra, N.; Claypoole, L.; Bachas, L. G., Morphological control of Ni/NiO core/shell nanoparticles and production of hollow NiO nanostructures. *Journal of Nanoparticle Research* **2010**, 12 (8), 2883-2893.
107. Khanna, P. K.; Gokhale, R.; Subbarao, V.; Vishwanath, A. K.; Das, B. K.; Satyanarayana, C. V. V., PVA stabilized gold nanoparticles by use of unexplored albeit conventional reducing agent. *Materials Chemistry and Physics* **2005**, 92 (1), 229-233.
108. Tang, X. L.; Jiang, P.; Ge, G. L.; Tsuji, M.; Xie, S. S.; Guo, Y. J., Poly(N-vinyl-2-pyrrolidone) (PVP)-capped dendritic gold nanoparticles by a one-step hydrothermal route and their high SERS effect. *Langmuir* **2008**, 24 (5), 1763-1768.
109. Westcott, S. L.; Oldenburg, S. J.; Lee, T. R.; Halas, N. J., Formation and adsorption of clusters of gold nanoparticles onto functionalized silica nanoparticle surfaces. *Langmuir* **1998**, 14 (19), 5396-5401.
110. Garg, N.; Scholl, C.; Mohanty, A.; Jin, R. C., The Role of Bromide Ions in Seeding Growth of Au Nanorods. *Langmuir* **2010**, 26 (12), 10271-10276.
111. Ekwall, P.; Mandell, L.; Solyom, P., The aqueous cetyl trimethylammonium bromide solutions. *Journal of Colloid and Interface Science* **1971**, 35 (4), 519-528.
112. Cappaere, E.; Cressely, R.; Decruppe, J. P., LINEAR AND NONLINEAR RHEOLOGICAL BEHAVIOR OF SALT-FREE AQUEOUS CTAB SOLUTIONS. *Colloids and Surfaces a-Physicochemical and Engineering Aspects* **1995**, 104 (2-3), 353-374.

113. Brown, K. R.; Natan, M. J., Hydroxylamine seeding of colloidal Au nanoparticles in solution and on surfaces. *Langmuir* **1998**, *14* (4), 726-728.
114. Gachard, E.; Remita, H.; Khatouri, J.; Keita, B.; Nadjo, L.; Belloni, J., Radiation-induced and chemical formation of gold clusters. *New Journal of Chemistry* **1998**, *22* (11), 1257-1265.
115. Jana, N. R.; Gearheart, L.; Murphy, C. J., Evidence for seed-mediated nucleation in the chemical reduction of gold salts to gold nanoparticles. *Chemistry of Materials* **2001**, *13* (7), 2313-2322.
116. Watzky, M. A.; Finke, R. G., Nanocluster size-control and "magic number" investigations, experimental tests of the "living-metal polymer" concept and of mechanism-based size-control predictions leading to the syntheses of iridium(0) nanoclusters centering about four sequential magic numbers. *Chemistry of Materials* **1997**, *9* (12), 3083-3095.
117. Wiesner, J.; Wokaun, A., Anisometric gold colloids- preparation, characterization, and optical-properties. *Chemical Physics Letters* **1989**, *157* (6), 569-575.
118. Kim, S. W.; Kim, M.; Lee, W. Y.; Hyeon, T., Fabrication of hollow palladium spheres and their successful application to the recyclable heterogeneous catalyst for Suzuki coupling reactions. *Journal of the American Chemical Society* **2002**, *124* (26), 7642-7643.
119. Teranishi, T.; Hosoe, M.; Tanaka, T.; Miyake, M., Size control of monodispersed Pt nanoparticles and their 2D organization by electrophoretic deposition. *Journal of Physical Chemistry B* **1999**, *103* (19), 3818-3827.
120. Li, F. B.; Li, X. Z., Photocatalytic properties of gold/gold ion-modified titanium dioxide for wastewater treatment. *Applied Catalysis a-General* **2002**, *228* (1-2), 15-27.
121. Inasawa, S.; Sugiyama, M.; Yamaguchi, Y., Laser-induced shape transformation of gold nanoparticles below the melting point: The effect of surface melting. *Journal of Physical Chemistry B* **2005**, *109* (8), 3104-3111.
122. Ohta, T.; Bostwick, A.; Seyller, T.; Horn, K.; Rotenberg, E., Controlling the electronic structure of bilayer graphene. *Science* **2006**, *313* (5789), 951-954.
123. Ottaviano, L.; DiNardo, S.; Lozzi, L.; Passacantando, M.; Picozzi, P.; Santucci, S., Thin and ultra-thin films of nickel phthalocyanine grown on highly oriented pyrolytic graphite: An XPS, UHV-AFM and air tapping-mode AFM study. *Surface Science* **1997**, *373* (2-3), 318-332.
124. Kwon, S. Y.; Ciobanu, C. V.; Petrova, V.; Shenoy, V. B.; Barenco, J.; Gambin, V.; Petrov, I.; Kodambaka, S., Growth of Semiconducting Graphene on Palladium. *Nano Letters* **2009**, *9* (12), 3985-3990.
125. Hu, M. H.; Noda, S.; Okubo, T.; Yamaguchi, Y.; Komiyama, H., Structure and morphology of self-assembled 3-mercaptopropyltrimethoxysilane layers on silicon oxide. *Applied Surface Science* **2001**, *181* (3-4), 307-316.